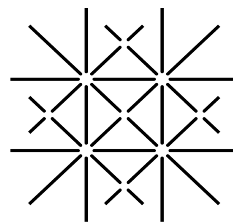


Micro- and Nanostructure of Human Teeth: a Synchrotron Radiation-based X-Ray Study

Inauguraldissertation
zur
Erlangung der Würde eines Doktors der Philosophie
vorgelegt der
Philosophisch-Naturwissenschaftlichen Fakultät
der Universität Basel

von

Hans Deyhle
aus Zürich, Schweiz



U N I
B A S E L

Basel, 2014

Genehmigt von der Philosophisch-Naturwissenschaftlichen Fakultät auf Antrag von:

Prof. Dr. Bert Müller, Fakultätsverantwortlicher
Prof. Dr. Thomas Jung, Korreferent

Basel, den 13. November 2012

Prof. Dr. Jörg Schibler, Dekan

Contents

Summary	v
Zusammenfassung	vii
List of Publications	ix
1 Introduction	1
2 Results	7
2.1 Implications of tooth micro- and nanoimaging for clinical applications	7
2.2 Optimization of the three-dimensional visualization of tooth micro- structure	19
2.3 Collagen content in carious dentin	31
2.4 Morphology of carious enamel	40
3 Conclusions	51
Bibliography	52
Acknowledgments	57
Curriculum Vitae	59

Summary

The anisotropic composite nature of human teeth guarantees their function for decades under high mechanical loads and adverse chemical conditions. Even more so since only marginal remodeling and repair mechanisms take place in adult teeth. While the macroscopical anatomy of the tooth has been well understood, long range ordering of the tooth's micro and nano components is still matter of research. Tooth micro- and nanostructure has been extensively studied, mainly with two-dimensional approaches as, for example, electron microscopy. The ultrastructural organization over a whole tooth is, however, not readily accessible with these approaches, because they only permit a very localized observation and often even remove the investigated structures from their natural three-dimensional organization.

The high degree of anisotropy in both dentin and enamel on the micro- and nanometer scale has a strong impact on the tooth's mechanical properties. For example, the Young's modulus and crack resistance of dentin are different parallel and perpendicular to the dentin tubules. Synchrotron radiation-based micro computed tomography with pixel sizes in the sub-micrometer range allows to three-dimensionally image dentin tubules, however only over restricted specimen sizes below one millimeter in diameter. To map the tubular network over an entire tooth, multiple scans are necessary. Given the generally limited beamtime available at synchrotron sources, a method has to be identified that allows for the visualization of dentin tubules with high accuracy and within reasonable time. Single distance phase retrieval, multiple distance phase retrieval and absorption contrast datasets, acquired at the beamline ID 19 at ESRF, were compared concerning their spatial and density resolution as well as their suitability for tubule rendering, and single distance phase retrieval, with a specimen detector distance of 75% of the critical value d^2/λ , was found to yield optimal results.

The knowledge of tooth ultrastructure is of particular interest when dealing with carious lesions. The treatment of carious lesions is nowadays accompanied by the removal of affected hard tissues and their replacement with isotropic restoration materials. Despite their high performance, these restorations have limited life span. As a result, additional clinical interventions and the replacement of the restoration are often necessary. An alternative would be the fabrication of anisotropic fillings, which mimic the natural organization of the tooth. Such structures are speculated to exhibit properties similar to those of healthy teeth and thus to be superior to the isotropic materials currently in use, thus extending restoration lifetime. For this purpose an extensive mapping of tooth ultrastructure is necessary. Small-angle X-ray scattering (SAXS) in scanning setup allows for the investigation of tooth nanostructural organization over extended areas. Scanning SAXS measurements of micrometer-thin tooth slices were performed at the cSAXS beamline at the Paul Scherrer Institut, revealing a high degree of structural organization of the tooth's nanometer-sized components. Based on this knowledge, a model for bio-mimetic fillings was proposed.

Nonetheless, bio-inspired fillings would still require costly interventions, and their superior performance has not been demonstrated yet. As alternative to restorations, where the affected tissue is removed and replaced with man-made materials, a treatment based on the re-mineralization of the carious lesion could be performed. The aim is not only the re-mineralization of de-mineralized tissues, but also the re-establishment of tooth morphology including its nanostructure, which in return will ensure mechanical properties comparable to those of healthy tissue. The morphology of the carious tissue is crucial for this procedure, as the structures retained in the lesion can act as nucleation sites for the re-mineralizing crystallites. Carious dentin and enamel were examined with scanning SAXS to determine whether the organization on the nanometer level is retained to some extent. In dentin, a significant part of the collagen network is retained concerning orientation and abundance after mild demineralization has taken place. In enamel, the overall orientation of the hydroxyapatite crystallites is unaltered, despite the complex organization of enamel lesions, consisting of alternating layers of de- and re-mineralized tissue.

Zusammenfassung

Menschliche Zähne bestehen aus stark anisotropen Verbundmaterialien, die trotz hoher mechanischer Belastungen und widrigen chemischen Bedingungen über Jahre Bestand haben. Dies obwohl Zähne nur über minimale regenerative Möglichkeiten verfügen. Die makroskopische Anatomie des Zahns ist gut bekannt. Seine Mikro- und Nanoanatomie hingegen sind noch nicht vollständig erforscht und auch heute noch Gegenstand intensiver Untersuchungen. Dazu werden meist zweidimensionale hochauflösende Bildgebungsverfahren, wie z.B. die Elektronenmikroskopie, verwendet. Allerdings sind mit diesen Methoden üblicherweise nur sehr lokalisierte Analysen möglich. Zusätzlich ist die Probenpräparation aufwändig, und kann unter Umständen die einzelnen Komponenten aus ihrer natürlichen Anordnung lösen.

Gerade die Zusammensetzung und Ausrichtung der Mikro- und Nanostruktur im gesamten Zahn sind aber von grossem Interesse, da diese die mechanischen Eigenschaften des Zahns bestimmen. So sind z.B. der E-Modul und die Rissfestigkeit des Dentins parallel und senkrecht zur Ausrichtung der Tubuli verschieden. Durch eine vollständige 3D-Visualisierung der Tubuli können daher Rückschlüsse auf die lokalen mechanischen Eigenschaften des Dentins gezogen werden. Diese Fragestellung kann mit Hilfe der synchrotronstrahlungsbasierten Mikro Computertomographie angegangen werden. Allerdings sind die Probengrößen, die man derzeit mit dieser Methode scannen kann, auf unter einen Millimeter Durchmesser beschränkt. Um die tubuläre Struktur eines ganzen Zahns zu untersuchen sind daher etliche Scans notwendig. Da Strahlzeit an Synchrotronquellen begrenzt ist, sollte die Scanmethode einerseits die nötige Orts- und Dichteauflösung liefern, andererseits aber mit möglichst wenig Strahlzeit auskommen. Deshalb wurden in der vorliegenden Arbeit verschiedene Aufnahmemodalitäten verglichen. Die Messungen wurden an der Beamline ID 19 am ESRF durchgeführt. Es wurden Phasenrekonstruktion aus einem einzigen Proben-Detektor Abstand, Phasenrekonstruktion aus mehreren Proben-Detektor Abständen und Absorptionskontrasttomographie bezüglich Orts- und Dichteauflösung sowie Tubulidarstellbarkeit verglichen. Die Einzel-Abstand Phasenberechnung mit einem Proben-Detektor Abstand, der 75% des kritischen Werts d^2/λ beträgt, wurde als die optimale Methode identifiziert.

Von besonderem Interesse ist die Zahn-Ultrastruktur wenn kariöse Läsionen vorhanden sind. Die Behandlung besteht oftmals in der Entfernung der befallenen Stelle und deren Ersatz durch i.A. isotrope Materialien. Obwohl diese mittlerweile hervorragende mechanische Eigenschaften aufweisen, haben sie eine begrenzte Lebensdauer, was oft eine Nachbehandlung und den Austausch des Zahnersatzes erfordert. Ersatzmaterialien, die die lokale Beschaffenheit des Zahns auf der Mikro- oder Nanoskala imitieren und daher zahnähnliche anisotrope mechanische Eigenschaften aufweisen, sollten hier von Vorteil sein, da erwartet werden kann, dass ihre Eigenschaften diejenigen herkömmlicher Materialien übertreffen. Für die Fertigung solcher Materialien ist es notwendig, die ortsabhängige Nanomorphologie des Zahns zu kennen. Diese kann mit Kleinwinkel-Röntgenstreuung im Scanning-Modus (scanning SAXS) erschlossen

werden. Scanning SAXS Messungen an Mikrometer dünnen Zahnscheiben wurden an der cSAXS Beamline am Paul Scherrer Institut durchgeführt. Der hohe Grad an struktureller langreichweitiger Organisation der Zahn-Nanokomponenten konnte so sichtbar gemacht werden. Anhand dieser Ergebnisse wurde ein Modell einer biomimetischen Zahnfüllung erstellt, welche die Nanomorphologie des Schmelzes und des Dentins imitiert.

Allerdings kann auch eine biomimetische Füllung mit überlegenen Eigenschaften die Notwendigkeit eines klinischen Eingriffs und die damit verbundenen Kosten nicht beseitigen. Hier können Ansätze, die auf die Reparatur des beschädigten Gewebes abzielen, Abhilfe schaffen. Ihr Ziel wäre nicht nur die Remineralisierung von kariösem Schmelz und Dentin, sondern auch die Wiederherstellung der Zahnmorphologie im Nanometerbereich, was auch die Wiederherstellung der mechanischen Eigenschaften des Zahns gewährleisten würde. Für eine solche Behandlung ist wiederum die Nanomorphologie des kariösen Gewebes ausschlaggebend, da die in der Läsion vorhandenen Strukturen als Keimbildungsstellen für die remineralisierenden Kristallite fungieren können. Kariöse Läsionen wurden ebenfalls an der cSAXS Beamline untersucht. Dabei wurde festgestellt, dass trotz kariösem Befall sowohl im Schmelz als auch im Dentin die natürliche Organisation der Nanostruktur zumindest teilweise erhalten ist. Im Dentin ist besonders in den frühen Stadien der Karies oder bei leichter Demineralisierung unter 10% ein signifikanter Anteil des Kollagennetzwerks bezüglich Menge und Orientierung erhalten. Im Schmelz ist die allgemeine Orientierung der Hydroxyapatitkristallite trotz der komplexen geschichteten Struktur der Läsion erhalten.

List of Publications

F. Kern, T. Waltimo, **H. Deyhle**, F. Beckmann, W. Stark, B. Müller, “Synchrotron radiation-based micro computed tomography in the assessment of dentin de- and re-mineralization.” *Proceedings of SPIE* **7078**, 70780M (2008). (doi:10.1117/12.795231)

H. Deyhle, O. Bunk, S. Buser, G. Krastl, N. Zitzmann, B. Ilgenstein, F. Beckmann, F. Pfeiffer, R. Weiger, B. Müller, “Bio-inspired dental fillings.” *Proceedings of SPIE* **7401**, 74010E (2009). (doi:10.1117/12.827437)

B. Müller, **H. Deyhle**, D. Bradley, M. Farquharson, G. Schulz, M. Müller-Gerbl, O. Bunk, “Scanning X-ray scattering: evaluating the nanostructure of human tissues.” *European Journal of Nanomedicine* **3**, 30-33 (2010). (doi:10.3884/0003.1.8)

B. Müller, **H. Deyhle**, G. Schulz, S. Mushkolaj, O. Bunk, “The nanostructure of biological tissues: a scanning X-ray scattering study.” *European Cells and Materials* **20**, 181 (2010). (doi:10.3884/0003.1.8)

H. Deyhle, O. Bunk, B. Müller, “Nanostructure of healthy and caries-affected human teeth.” *Nanomedicine: Nanotechnology, Biology, and Medicine* **7**, 694-701 (2011). (doi:10.1016/j.nano.2011.09.005)

S. Köhl, **H. Deyhle**, M. Zimmerli, G. Spagnoli, F. Beckmann, B. Müller, A. Filippi, “Cracks in dentin and enamel after cryo-preservation.” *Oral Surgery, Oral Medicine, Oral Pathology, Oral Radiology and Endodontology* **113**, e5-e10 (2011). (doi:10.1016/j.tripleo.2011.06.020)

G. Schulz, **H. Deyhle**, B. Müller, “Imaging the human body: Micro- and nanostructure of human tissues.” In: *Nanomedicine and Nanobiotechnology* (Ed. S. Logothetidis), 64-69, Springer 2012. (doi:10.1007/978-3-642-24181-9_4)

H. Deyhle, G. Schulz, B. Müller, “Imaging the human body down to the molecular level.” In *Encyclopedia of Nanotechnology* (Eds. B. Bhushan, H.D. Winbigler), 1049-1056, Springer 2012. (doi:10.1007/978-90-481-9751-4_326)

H. Deyhle, S. Hieber, B. Müller, “Nanodentistry.” In *Encyclopedia of Nanotechnology* (Eds. B. Bhushan, H.D. Winbigler), 1514-1518, Springer 2012. (doi:10.1007/978-90-481-9751-4)

S. Gaiser, **H. Deyhle**, O. Bunk, S. White, B. Müller, “Understanding nano-anatomy of healthy and carious human teeth: a prerequisite for nanodentistry.” *Biointerphases* **7**, 4 (2012). (doi:10.1007/s13758-011-0004-8)

H. Deyhle, T. Weitkamp, S. Lang, G. Schulz, A. Rack, I. Zanette, B. Müller, “Comparison of propagation-based phase-contrast tomography approaches for

the evaluation of dentin microstructure.” *Proceedings of SPIE* **8506**, 85060N (2012). (doi:10.1117/12.929951)

H. Deyhle, S. N. White, O. Bunk, F. Beckmann, B. Müller, “Nanostructure of the carious tooth enamel lesion.” *Acta Biomaterialia* **10**, 355-364 (2014). (doi:10.1016/j.actbio.2013.08.024)

Publications not directly related to the present thesis

H. Deyhle, M. Hirayama, F. Zuber, B. Müller, “Morphology of metal-coated silicone films.” *European Cells and Materials* **16**, 31 (2008). (ISSN:1473-2262)

B. Müller, S. Lang, M. Dominiotto, M. Rudin, G. Schulz, **H. Deyhle**, M. Germann, F. Pfeiffer, C. David, T. Weitkamp, “High-resolution tomographic imaging of microvessels.” *Proceedings of SPIE* **7078**, 70780B (2008). (doi:10.1117/12.794157)

B. Müller, **H. Deyhle**, S. Mushkolaj, M. Wieland, “The challenges in artificial muscle research to treat incontinence.” *Swiss Medical Weekly* **139**, 591-595 (2009).

B. Müller, **H. Deyhle**, F. Fierz, S. Irsen, J. Yoon, S. Mushkolaj, O. Boss, E. Vondran, U. Gbureck, Ö. Degistrici, M. Thie, B. Leukers, F. Beckmann, F. Witte, “Bio-mimetic hollow scaffolds for long bone replacement.” *Proceedings of SPIE* **7401**, 74010D (2009). (doi:10.1117/12.825487)

H. Deyhle, F. Schmidli, G. Krastl, B. Müller, “Evaluating tooth restorations: Micro computed tomography in practical training for students in dentistry.” *Proceedings of SPIE* **7804**, 780417 (2010). (doi:10.1117/12.859842)

T. Weitkamp, I. Zanette, C. David, J. Baruchel, M. Bech, P. Bernard, **H. Deyhle**, T. Donath, J. Kenntner, S. Lang, J. Mohr, B. Müller, F. Pfeiffer, E. Reznikova, S. Rutishauser, G. Schulz, A. Tapfer, J. Valade, “Recent developments in X-ray Talbot interferometry at ESRF-ID19.” *Proceedings of SPIE* **7804**, 780406 (2010). (doi:10.1117/12.860203)

J. Gugger, G. Krastl, M. Huser, **H. Deyhle**, B. Müller, “The morphology of amputated human teeth and its relation to mechanical properties after restoration treatment.” *Proceedings of SPIE* **7804**, 78041H (2010). (doi:10.1117/12.859813)

G. Schulz, A. Morel, M. S. Imholz, **H. Deyhle**, T. Weitkamp, I. Zanette, F. Pfeiffer, C. David, M. Müller-Gerbl, B. Müller, “Evaluating the microstructure of human brain tissues using synchrotron radiation-based micro computed tomography.” *Proceedings of SPIE* **7804**, 78040F (2010). (doi:10.1117/12.859273)

L. Kofmehl, G. Schulz, **H. Deyhle**, A. Filippi, G. Hotz, D. Berndt-Dagassan, S. Kramis, F. Beckmann, B. Müller, “Computed tomography to quantify tooth abrasion.” *Proceedings of SPIE* **7804**, 78041F (2010). (doi:10.1117/12.859278)

-
- S. Gürel, C. Unold, **H. Deyhle**, G. Schulz, S. Köhl, B. Saldamli, J. Tübel, R. Burgkart, F. Beckmann, B. Müller, “The microstructure of mandibular bone grafts and three-dimensional cell clusters.” *Proceedings of SPIE* **7804**, 78041G (2012). (doi:10.1117/12.859437)
- T. Jensen, M. Bech, I. Zanette, T. Weitkamp, C. David, **H. Deyhle**, R. Feidenhans'l, F. Pfeiffer, “Directional x-ray dark-field imaging of strongly ordered systems.” *Physical Review B* **82**, 214103 (2010). (doi:10.1103/PhysRevB.82.214103)
- T. Weitkamp, I. Zanette, G. Schulz, M. Bech, S. Rutishauser, S. Lang, T. Donath, A. Tapfer, **H. Deyhle**, P. Bernard, J. Valade, E. Reznikova, J. Kennner, J. Mohr, B. Müller, F. Pfeiffer, C. David, J. Baruchel, “X-ray grating interferometry at ESRF: Applications and recent technical developments.” *AIP Conference Proceedings* **1365**, 28-31 (2010). (doi:10.1063/1.3625297)
- M. Luckow, **H. Deyhle**, F. Beckmann, D. Dagassan-Berndt, B. Müller, “Tilting the jaw to improve the image quality or to reduce the dose in cone-beam computed tomography.” *European Journal of Radiology* **80**, e389-e393 (2011). (doi:10.1016/j.ejrad.2010.10.001)
- G. Krastl, J. Gugger, **H. Deyhle**, N. Zitzmann, R. Weiger, B. Müller, “Impact of adhesive surface and volume of luting resin on fracture resistance of root-canal treated teeth.” *International Endodontic Journal* **44**, 432-439 (2011). (doi:10.1111/j.1365-2591.2010.01846.x)
- B. Ilgenstein, **H. Deyhle**, B. Müller, “Bone augmentation for inserting oral implants.” *European Cells and Materials* **22**, 11 (2011). (ISSN:1473-2262)
- J. Althaus, **H. Deyhle**, O. Bunk, B. Müller, “Structural anisotropies of PEEK foils revealed by optical dichroism and X-ray scattering methods.” *European Cells and Materials* **22**, 29 (2011). (ISSN:1473-2262)
- B. Müller, **H. Deyhle**, S. Lang, G. Schulz, T. Bormann, F. Fierz, S. Hieber, “Three-dimensional registration of tomography data for quantification in biomaterials science.” *International Journal of Materials Research* **103**, 242-249 (2012). (doi:10.3139/146.110663)
- J. Yoon, **H. Deyhle**, U. Gbureck, E. Vorndran, F. Beckmann, B. Müller, “Three-dimensional morphology and mechanics of bone scaffolds fabricated by rapid prototyping.” *International Journal of Materials Research* **103**, 200-206 (2012). (doi:10.3139/146.110661)
- J. Althaus, **H. Deyhle**, O. Bunk, P.M. Kristiansen, B. Müller, “Anisotropy in polyetheretherketone films.” *Journal of Nanophotonics* **6**, 063510 (2012). (doi:10.1117/1.JNP.6.063510)
- J. Althaus, P. Urwyler, C. Padeste, R. Heuberger, **H. Deyhle**, H. Schiff, J. Gobrecht, U. Pieses, D. Scharnweber, K. Peters, B. Müller, “Micro- and nanostructured polymer substrates for biomedical applications.” *Proceedings of SPIE* **8339**, 83390Q (2012). (doi:10.1117/12.915235)

- F. Weiss, **H. Deyhle**, G. Kovacs, B. Müller, “Designing micro- and nanostructures for artificial urinary sphincters.” *Proceedings of SPIE* **8340**, 83400A1 (2012). (doi:10.1117/12.914649)
- P. Urwyler, **H. Deyhle**, O. Bunk, P.M. Kristiansen, B. Müller, “Nanometer-size anisotropy of injection-molded polymer micro-cantilever arrays.” *Journal of Applied Physics* **111**, 103530 (2012). (doi:10.1063/1.4720942)
- B. Müller, G. Schulz, A. Mehlin, J. Herzen, S. Lang, M. Holme, I. Zanette, S. Hieber, **H. Deyhle**, F. Beckmann, F. Pfeiffer, T. Weitkamp, “Grating-based tomography of human tissues.” *AIP Conference Proceedings* **1466**, 107-112 (2012). (doi:10.1063/1.4742277)
- Y.-C. Brogle-Kim, **H. Deyhle**, B. Müller, G. Schulz, T. Bormann, F. Beckmann, K. Jäger, “Evaluation of oral scanning in comparison to impression using three-dimensional registration.” *Proceedings of SPIE* **8506**, 85061R (2012). (doi:10.1117/12.929727)
- B. Ilgenstein, **H. Deyhle**, C. Jaquiere, C. Kunz, A. Stalder, S. Stübinger, G. Jundt, F. Beckmann, B. Müller, S. E. Hieber “Combined micro computed tomography and histology study of bone augmentation and distraction osteogenesis.” *Proceedings of SPIE* **8506**, 85060M (2012). (doi:10.1117/12.929616)
- M. N. Holme, G. Schulz, **H. Deyhle**, S. E. Hieber, T. Weitkamp, F. Beckmann, J. Herzen, J. A. Lobrinus, F. Montecucco, F. Mach, A. Zumbuehl, T. Saxer, B. Müller, “Morphology of atherosclerotic coronary arteries.” *Proceedings of SPIE* **8506**, 850609 (2012). (doi:10.1117/12.930052)
- C. Vögtlin, G. Schulz, **H. Deyhle**, K. Jäger, T. Liebrich, S. Weikert, B. Müller, “Comparison of denture models by means of micro computed tomography.” *Proceedings of SPIE* **8506** 85061S (2012). (doi:10.1117/12.930068)

1 Introduction

Human teeth belong to the most durable tissues in the human body. Their anisotropic composite nature guarantees function for decades under mechanical loads as high as 380 N [1] and adverse chemical conditions, even more so since only marginal remodeling and repair mechanism in adult teeth take place. Enamel, constituting the crown of the tooth, is composed to 96% of carbonated hydroxyapatite, while less than one percent of organic material is present [2]. The high mineral content makes enamel the hardest substance in the human body, but also renders it quite brittle and prone to crack formation. The microscopic organization of enamel reflects its formation process. The growth tracks of the ameloblasts, the cells responsible for enamel formation, present themselves as keyhole-shaped prisms or rods [3], which run from the dentin-enamel junction (DEJ) towards the tooth surface. The organization of the primary structural units of enamel, the nanometer-sized hydroxyapatite crystallites, has been studied extensively with scanning and transmission electron microscopy (SEM, TEM), [3–5]. Crystallites within the rod head run parallel to the rod direction, while their angle with respect to the rod direction increases to reach angles as high as 60° within the tail [3, 6, 7].

The supporting structure of human teeth is dentin, which abuts on enamel. It is essentially composed of carbonate-rich enamel crystallites embedded in an organic matrix of collagen fibers. The distinguishing microstructural features are the dentin tubules, micrometer-thin channels which mark the growth tracks of the odontoblasts and run from the DEJ towards the pulp. They are surrounded by the highly mineralized peri-tubular dentin (PTD) and embedded in a less mineralized collagen-hydroxyapatite composite termed inter-tubular dentin (ITD). The collagen fibers lie perpendicular to the tubules, and the dentinal hydroxyapatite crystallites align along the collagen fibers [8]. Therefore, dentin tubuli orientation is strongly linked to the organization of the nanometer sized dentin components.

While the macroscopical anatomy of the tooth has been well understood, long range ordering of tooth micro and nano components is still matter of research. Extensive investigations have been performed in this direction, mainly with two-dimensional approaches as SEM and TEM, which only permit a very localized observation and often even remove the investigated structures from their natural three-dimensional (3D) organization, thus losing important information about the orientation. The high degree of anisotropy in both dentin and enamel, however, has a strong impact on their mechanical behavior as well as on diffusion processes involved in carious attacks. It is therefore desirable to identify a technique that allows the investigation of the nanometer-sized tooth components while still retaining fields of view in the order of 1 cm².

Small-angle X-ray scattering

The present work proposes small-angle X-ray scattering (SAXS) in combination with scanning in real space [9, 10] as a possibility to access information about tooth nanostructure over extended areas. As all scattering techniques, SAXS is based on a reciprocal relationship between the size of the scattering features and the scattering angle [11]. Classically, the relation between scattering angle and X-ray wavelength is given by the Bragg equation

$$n\lambda = 2d\sin(\theta) \quad (1.1)$$

where λ is the wavelength of the X-rays, d is the size of the scattering features, 2θ is the scattering angle, and $n = 1, 2, 3, \dots$. For values of d much larger than λ , the scattering angle becomes accordingly small. More generally, the diffraction pattern of a sample can be described in terms of reciprocal, or Fourier, space [12], if only coherent scattering is considered. Since the scattering angles are small, this condition is met [11]. Let $\rho(r)$ denote the electron density of the sample, then the scattered amplitude corresponds to

$$A(\vec{q}) = \int \rho(r) \cdot e^{-i\vec{q}\cdot\vec{r}} dV \quad (1.2)$$

where $q = \frac{4\pi}{\lambda}\sin(\theta)$ is the momentum transfer of the scattered photons. Since not the amplitude, but the intensity I of the scattered photons is detected, the scattered intensity observed at a certain q -value is the square of the amplitude $A(\vec{q})$ [12]. It follows from Eq. 1.2 that for samples with constant electron density no scattering is observed. Only specimens exhibiting electron density variations on the nanometer scale will yield SAXS signal [11].

In the scanning setup, as preformed at the cSAXS beamline (Swiss Light Source, Paul Scherrer Institut, Villigen, Switzerland), the specimen is scanned through the micro-focus X-ray beam in a raster scan fashion in the plane perpendicular to the beam. At each raster point, a scattering pattern is acquired. In such a fashion, a two dimensional (2D) map of the investigated specimen is created, containing information about orientation, degree of anisotropy and abundance of nanometer-sized scatterers within the the plane perpendicular to the beam. Generally, micrometer-thin specimens are required. On one hand, since only a small fraction of the incoming radiation contributes to the scattering signal, X-ray absorption should be kept as low as possible. On the other hand, the whole illuminated volume contributes to the scattering signal. If morphologically different zones are present within the thickness of the specimen, all will contribute to the SAXS signal, making a distinction difficult.

Scanning SAXS has been successfully applied to a variety of fields, like material and life sciences. For example, anisotropic layers in injection-molded polymer micro-cantilevers [13] and embossing-induced crystallinity in commercially available PEEK foils [14] have been investigated. Moreover, investigations of human brain tissue and urethra were performed [15].

Dentin tubular structure

For the mechanical properties of human teeth, the tubular structure in dentin is of particular interest. For example, Nalla *et al.* [16] reported that the fracture

toughness of dentin varies depending on the crack orientation with respect to the dentin tubules. Many studies on dentin tubular structure, mainly based on 2D approaches exist [16–18]. It is generally assumed that the tubules run parallel to each other in a continuous fashion from the DEJ to the pulp. However, local tilting of tubuli with respect to each other and tubuli that end before reaching the pulp might occur. Synchrotron radiation-based micro computed tomography (SR μ CT) using hard X-rays offers the means to image tooth microstructure and has, for example, successfully been applied to the investigation of cryo-induced cracks [19] or for the quantification of tooth abrasion [20]. With the advent of detectors with pixel sizes in the sub-micron range, the 3D investigation of dentin tubuli became possible with tomographic setups both in absorption [21–24] and phase contrast [25,26] modalities. However, due to the reduced pixel sizes, the field of view is restricted to about one millimeter. Therefore, in high resolution tomographic investigations generally tiny, sub-millimeter thin rods were cut from human teeth. Thus it is not yet possible to access the entire tubular structure within the tooth with a single specimen, and scans of multiple specimens obtained from one tooth would be necessary [22]. Therefore, the identification of an imaging approach suited for the visualization of dentin tubuli with the required spatial resolution within reasonable time is necessary.

Possible approaches for the treatment of caries

The knowledge of tooth ultrastructure is of particular interest when dealing with carious lesions. Caries is a bacterial infection that damages enamel and dentin through the release of acidic species which dissolve tooth tissues. Since human teeth possess only minimal regenerative possibilities, treatment of caries is often accompanied by the removal of the affected region. The anisotropic load bearing tooth tissue is replaced with isotropic restoration materials. With the exception of posts, restoration materials that mimic the anisotropic, highly oriented tooth structure do not exist. Hence, even though current restoration materials exhibit outstanding mechanical properties, they do not fully fit the performance of healthy tooth tissues, resulting in a limited life span of the restoration, which renders further interventions necessary [27,28]. A possible approach for the improvement of filling materials is the realization of bio-inspired dental fillings, which mirror tooth micro or nano-morphology [21]. The nanometer-sized components in dentin and enamel change their orientation depending on the location within the tooth. The morphology of the restoration should adapt accordingly. Therefore, a comprehensive understanding of nanostructural organization within human teeth is necessary.

Although caries can be sometimes arrested under optimized conditions, removal of the affected part is generally unavoidable to the present day given the low regenerative capabilities of human teeth. Since restorative dental treatments are generally associated with high costs, the question arises whether it is possible to regenerate the damaged tissues instead of replacing them. The possibilities have mainly been examined *in vitro* [29,30]. However, caries is a complex process, involving many cycles of naturally occurring de-mineralization and re-mineralization, leading to porous substrates with varying pore sizes and pore size distributions, which in return affect the diffusion processes involved in the dissolution of the dental tissues [5,31,32]. Thus, the caries affected regions exhibit different morphologies depending on location.

Early carious lesions are restricted to enamel. They are described as consisting of four zones. The surface layer is located at the outer surface of enamel. It appears as a thin, relatively unaffected region with about 10% mineral loss. Adjacent to it the so called body of the lesion is found, an extended area exhibiting an increased de-mineralisation of about 25%. Even deeper within the lesion one finds the dark zone, presenting only about 6% mineral loss. The most advanced region, called translucent zone, exhibits only minimal de-mineralization, generally below 5%. This classification is based on polarized light microscopy, which does not offer sufficient spatial resolution to access information about the individual crystallites. SAXS on the other hand fits for the investigation on the length scale of the crystallites, and allows to access tooth nanostructure orientation, which appears to remain unaltered by the attack [33]. It also allows estimates of pore abundance and pore size distribution, independent on pore accessibility, as opposed for example to vapour deposition. A deep characterization of the enamel carious zones will allow for a better understanding of the carious process and therefore facilitate the development of non-invasive restoration treatments.

When dealing with deeper lesions, dentin becomes affected. Here, multiple attempts of classification were made. Ohgushi *et al.* [34] proposed a classification based on the stainability with fuchsin. More recently, Pugach *et al.* [35] used a similar approach, and defined four different zones within carious dentin. Since dentin is a composite, consisting of organic and inorganic components, the question arises whether these components react differently to the carious attack. Since the inorganic hydroxyapatite is highly susceptible to acidic attacks, it can be expected that its dissolution proceeds faster than that of the organic components, and thus in carious lesions the collagen is preserved to a certain extent. This has important implications for a possible re-mineralization treatment. As the anisotropic morphology on the micro- and nanoscale are fundamental for the tooth's mechanical performance, such treatments should not only aim at restoring the original mineral content within the affected dentin, but also to restore its original morphology. The presence of an unaffected collagen network might act as nucleation site for the formation of crystallites, thus allowing to revert the damage caused by the carious infection.

The inspection of teeth with non-destructive X-ray methods allows to access their morphology on the micro- and nanometer scale, making a quantitative classification of carious tooth structure possible.

Salient points

Chapter 2.1 deals, on the one hand, with the possibilities for the visualization of tooth microstructure. Visualization of dentin tubules by SR μ CT was demonstrated and their orientation at the DEJ revealed. Since only a restricted part of a tooth was imaged, however, generalizations regarding tubule orientation at the DEJ are somehow speculative. On the other hand, tooth nano-anatomy, focusing on unaffected healthy tooth tissues, was inspected with scanning SAXS, revealing strong anisotropy within the tooth and its long range organization. Note that in Figures 6 and 7 the color-wheel indicates the main axes of the scatterers, not the orientation of the scattering signal as stated in the figure captions. Therefore, Figure 8 is presented in a modified fashion in Deyhle *et al.* [36]. Based on these findings dental experts proposed a model for bio-inspired dental fillings, which mimic the

natural organization of the human tooth, illustrated in Figure 8. The contribution of Figure 8 to the manuscript by Dr. Bernd Ilgenstein is gratefully acknowledged.

In chapter 2.2 the possibilities for an optimized visualization of the dentin tubular system by diverse SR μ CT approaches is investigated further. Single-distance phase retrieval, performed with the freely available software *ANKAphase* [37], which is based upon an algorithm presented by Paganin *et al.* [38], is proposed as the option of choice. An optimal specimen-detector distance for tubule visualization is postulated based on the contrast-to-noise ratio, slightly modified from the one proposed by Herzen *et al.* [39] to better fit the experimental data, and spatial resolution of the acquired datasets. The reconstruction of the multiple-distance phase retrieval data by Dr. Sabrina Lang is gratefully acknowledged.

Caries-induced changes to the tooth's nanostructural components are investigated in chapters 2.3 and 2.4. Chapter 2.3 focuses on dentin, with particular attention given to its organic components. Twelve specimens, exhibiting carious lesions extending to the dentin, were investigated. The intensity of scattering originating from collagen I, related to collagen abundance, was extracted from the scattering patterns based on an algorithm proposed by Bunk *et al.* [10] and compared to the X-ray absorption within the lesions, revealing that a significant part of the collagen network remains intact concerning abundance and orientation when de-mineralization does not exceed 90% in dentin.

Chapter 2.4 deals with early enamel caries, where the dentin is not or only minimally affected. SAXS measurements reveal distinct zones within the enamel lesion, which can be distinguished by their scattering potential, linked to caries induced voids in the inorganic phases of the enamel. Two zones, presenting similar pore size distribution, but different pore abundance, are identified in the outer parts of the lesion. A third zone, presenting larger pores, is located adjacent to the enamel. Despite the degradation of the inorganic phases within the lesion, the data demonstrate the preservation of orientation of the overall enamel structure. The invaluable help in data interpretation by S.N. White is gratefully acknowledged.

2 Results

2.1 Implications of tooth micro- and nanoimaging for clinical applications

The manuscript proposes synchrotron radiation-based micro computed tomography and small-angle X-ray scattering as methods for the investigation of tooth micro- and nanostructure. Based on the acquired data speculations are made about the possibility of bio-inspired dental fillings, which mimic the natural organization of tooth tissue.

Published in Proceedings of SPIE

Bio-inspired dental fillings

Hans Deyhle^{a,b}, Oliver Bunk^c, Stefan Buser^{a,b}, Gabriel Krastl^a, Nicola U. Zitzmann^a,
Bernd Ilgenstein^a, Felix Beckmann^d, Franz Pfeiffer^{c,e}, Roland Weiger^a, and Bert Müller^{*a,b}

^aSchool of Dental Medicine, University of Basel, Hebelstrasse 3, 4056 Basel, Switzerland;

^bBiomaterials Science Center, University of Basel, c/o University Hospital, 4031 Basel, Switzerland;

^cPaul Scherrer Institute, 5232 Villigen-PSI, Switzerland;

^dGKSS Research Center, Max-Planck-Str. 1, 21502 Geesthacht, Germany;

^eDepartment of Physics (E17), Technical University Munich, 85748 Garching, Germany

ABSTRACT

Human teeth are anisotropic composites. Dentin as the core material of the tooth consists of nanometer-sized calcium phosphate crystallites embedded in collagen fiber networks. It shows its anisotropy on the micrometer scale by its well-oriented microtubules. The detailed three-dimensional nanostructure of the hard tissues namely dentin and enamel, however, is not understood, although numerous studies on the anisotropic mechanical properties have been performed and evaluated to explain the tooth function including the enamel-dentin junction acting as effective crack barrier. Small angle X-ray scattering (SAXS) with a spatial resolution in the 10 μm range allows determining the size and orientation of the constituents on the nanometer scale with reasonable precision. So far, only some dental materials, i.e. the fiber reinforced posts exhibit anisotropic properties related to the micrometer-size glass fibers. Dental fillings, composed of nanostructures oriented similar to the natural hard tissues of teeth, however, do not exist at all. The current X-ray-based investigations of extracted human teeth provide evidence for oriented micro- and nanostructures in dentin and enamel. These fundamental quantitative findings result in profound knowledge to develop biologically inspired dental fillings with superior resistance to thermal and mechanical shocks.

Keywords: human tooth, dentin, enamel, small angle X-ray scattering, micro computed tomography, microtubules, anisotropy, microstructure, nanometer scale, synchrotron radiation

1. INTRODUCTION

Enamel and dentin of human teeth belong to the anisotropic biological materials. Enamel is known as highly mineralized hard and brittle substance [1]. On the micrometer scale, oriented enamel rods or prisms can be observed, which are the result of polarized columnar cells termed *ameloblasts*. These enamel rods mainly consist of densely packed calcium phosphates. It is also found within the spaces between the crystallites. The only difference between the calcium phosphate in and between the rods is their orientation on the nanometer scale.

Dentin can be regarded as a natural composite consisting of carbonate-rich calcium phosphate nanometer-sized crystallites embedded in collagen fiber networks. As the result of the different composition and density X-ray-based imaging easily permits the discrimination between the two hard tissues dentin and enamel.

While the principal anatomy of the tooth has been understood since decades, the detailed three-dimensional micro- and nanostructure especially at the dentin-enamel junction is still matter of research (see, e.g. [1-3]). Electron microscopy micrographs provide impressive qualitative insights into the crystallite morphology, but the quantitative evaluation is time-consuming and complex as well as distorted by the sectioning artifacts. Nevertheless, there are several successful attempts to uncover the size, orientation, and density of the apatite crystallites as well as the organization of the collagen fibrils in the three-dimensional space.

*bert.mueller@unibas.ch; phone 41 61 265-9660; fax 41 61 265-9699; www.bmc.unibas.ch

The studies include synchrotron radiation-based small angle X-ray scattering (SAXS) with a spatial resolution down to 200 μm [3]. Although these SAXS studies already indicate local variations in the ordered phases within the dentin, the restricted spatial resolution has not allowed any conclusion about the enamel-dentin junction that is of paramount importance for the mechanical properties of the entire teeth [1]. The present investigation evaluates how far scanning SAXS with a spatial resolution in the range of 10 μm [4] can contribute to an improved understanding of the nano-architecture of dentin and enamel in particular near the dentin-enamel junction, where the ordered dentinal tubules are supposed to end. This morphological transition adapts the mechanical properties between the enamel of high strength and brittleness and the supportive compliant dentin [1]. So far, dental fillings used to repair (caries-induced) defects do not exhibit any similar micro- or nano-architecture neither anisotropic mechanical properties as observed for the two biological materials. In this context, the current study on the three-dimensional micro- and nano-architecture of the underlying structural elements should enable the realization of bio-mimetic dental fillings with superior resistance to thermal and, more important, to mechanical shocks.

2. MATERIALS AND METHODS

2.1 Tooth selection and preparation for X-ray imaging

An extracted non-restored molar tooth of the fourth quadrant without any visible damage was selected for the experiments. The human tooth was caries-free as it did not show any clinical sign of enamel caries. For the measurements the extracted tooth was placed into an Eppendorf tube to avoid dehydration.

2.2 Conventional micro computed tomography of teeth

Micro computed tomography (μCT) measurements of the complete tooth in the liquid-filled Eppendorf tube were performed with the system 1174TM (SkyScan, Kontich, Belgium) [5, 6]. The fixed specimen rotation stage allows for positioning in one direction perpendicular to the X-ray beam. The X-ray absorption of the tooth required the highest possible accelerating voltage of 50 kV and the application of a 0.5 mm-thick aluminum filter. The focus between the X-ray scintillator and the one megapixel CCD detector was adjusted to obtain an isotropic pixel size of 28.8 μm . 900 projections from 0 to 360° in steps of 0.4° were recorded using a beam current of 800 μA . The reconstruction was performed with a modified Feldkamp algorithm using SkyScan NreconTM software.

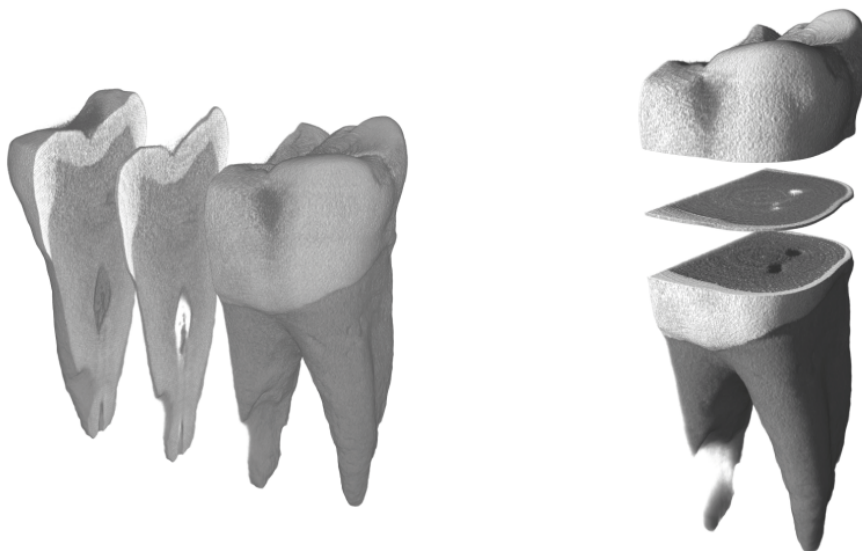


Fig. 1. Preparation of teeth slices for the high-resolution measurements parallel and perpendicular to the tooth axis. The images were generated from the μCT -data using the software VG Studio Max 1.2.1 (Volume Graphics, Heidelberg, Germany).

2.3 Specimen preparation

Based on the μ CT results of the complete tooth, Figure 1 schematically shows the harvesting of slices with thicknesses of about 200 μm and 300 μm , respectively. The slices were obtained parallel and perpendicular to the tooth axis. A saw (Exact Apparatebau GmbH, Norderstedt, Germany) equipped with a 0.2 mm cutting diamond band served for the slice preparation.

2.4 Synchrotron radiation-based micro computed tomography

The SR μ CT-measurements were performed at two different beamlines: W 2 (HASYLAB at DESY, Hamburg, Germany) and TOMCAT (SLS at PSI, Villigen, Switzerland).

The beamline W 2 with its standard setup for absorption contrast tomography [7], operated by the GKSS Research Center, served for the simultaneous visualization of a series of teeth slices combined in one container filled with phosphate buffer saline (PBS). The photon energy was set to 45 keV. The present study included two datasets at different heights, which were combined after reconstruction with pixel resolution. The rotation axis was chosen asymmetrical to the incoming X-ray beam to increase the spatial resolution [8]. Therefore, the complementary projections were combined before reconstruction. The number of projections corresponded to 1441 acquired by rotating the sample in steps of 0.25° from 0 to 360° . The filtered back-projection algorithm served for the slice-wise reconstruction [9]. In order to improve the density resolution at the restricted number of projections, the data, recorded with a pixel size of 4.6 μm , were binned by a factor of two before reconstruction [10]. The spatial resolution determined from the 10% value of the modulated transfer function of a highly X-ray absorbing edge corresponded to 8.8 μm [11].

The SR μ CT-measurements at TOMCAT [12] were carried out in absorption contrast mode using a photon energy of 15 keV with a band width of 2% to 3% and an exposure time of 170 ms per projection. The absorption contrast contains edge enhancement as well. For these experiments a rod was cut out of the tooth slice so that the specimen presented with a maximum diameter of 0.7 mm. This setting permitted high-resolution measurements with a pixel size of 0.37 μm . The specimen held in air was rotated in steps of 0.12° between 0° and 180° to record the projections. Reconstructed data were obtained by means of the filtered back-projection available at the beamline, where 9 height steps were acquired to follow a reasonable volume within dentin and enamel as well as of the dentin-enamel junction.

2.5 Small angle X-ray scattering

Small angle X-ray scattering (SAXS) is a powerful method that profits from the elastic scattering of X-rays at features within the nanometer range [13]. SAXS is usually restricted to scattering angles well below 10° . SAXS data contain quantitative information averaged on the illuminated area.

As schematically shown in Figure 2, the X-ray beam with the selected photon energy is scattered by the nanometer-sized features of the tooth slice. The interaction of the keV-photons with matter, however, is rather weak, so that most of the beam simply penetrates the tooth slice. In order to detect the weak scattered intensities, a beam stop is usually incorporated (see Figure 2).

The SAXS measurements were performed at the cSAXS beamline of the Swiss Light Source (Paul Scherrer Institut, Villigen, Switzerland). A monochromatic X-ray beam with a photon energy of 18.58 keV was focused to a spot of about $20 \mu\text{m} \times 5 \mu\text{m}$ for the raster scan measurements. Two modules of a PILATUS detector [14] with about 190'000 pixels in total have been used for the detection. To speed up the data acquisition, the tooth slice was moving at constant speed along a line of the 2D raster pattern, while the detector was continuously recording data. The detector was operated with 20 ms exposure time and 8 ms readout time. This selection corresponds to a frame rate of 36 Hz.

In order to determine information on the abundance of nanostructures of interest within the illuminated point of the raster scan, the recorded intensity was averaged within the related ring around the through beam. The orientation and the anisotropy of these nanostructures follow the angular intensity distribution along the ring [4]. One finally obtains an intensity map with the color-coded orientation for the selected nanometer range.

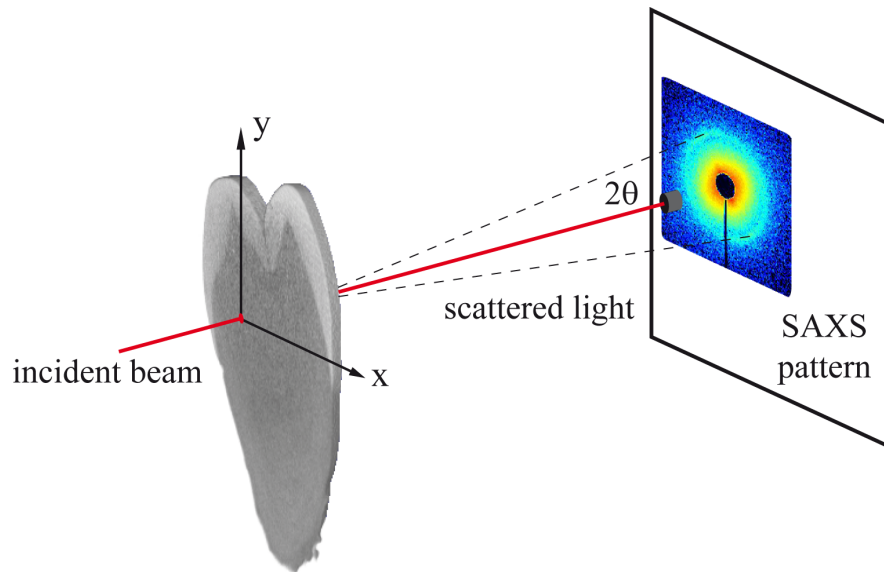


Fig. 2. The X-ray beam, about $5\ \mu\text{m} \times 20\ \mu\text{m}$ wide, perpendicularly hits the tooth slice that can be moved along x and y directions. For each (x,y)-position a SAXS pattern is recorded. Finally a ring of each SAXS pattern around the direct beam is analyzed to determine the size and orientation of the nanometer-sized features of dentin and enamel.

3. RESULTS

3.1 Micro computed tomography to characterize the tooth slices

Synchrotron radiation-based micro computed tomography (SR μ CT) served for both the determination of the outer shape of the entire slice, which includes the measurement of the slice thickness, and the internal microstructure of the tooth slice.

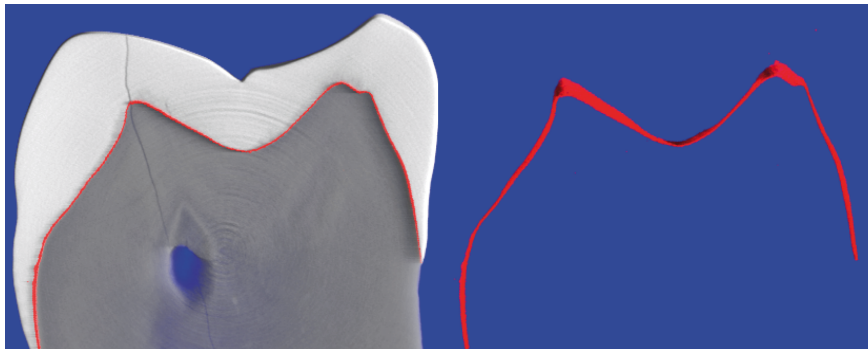


Fig. 3. The high-resolution tomography experiments of the tooth slice enable the segmentation of two homogeneous components (enamel and dentin) and the interface (as the result of the partial volume effect). In addition, the image also shows a crack and an abrasion on the enamel.

One can perfectly discriminate between enamel and dentin because of the different X-ray absorption (see Figure 3). Dentin and enamel, however, appear as homogeneous materials. Hence, the value of the SR μ CT remains in the measurement of the slice thickness and parallelism and, more important, in the local orientation of the dental-enamel junction. If the dental-enamel junction is parallel to the beam direction for the SAXS measurements, one can draw

conclusions about this interface. If the interface, however, shows an angle of 45° for instance, the SAXS-measurements yields a mean value of both enamel and dentin.

3.2 Microstructure of dentin: Visualization of tubules

For the high-resolution tomography, a rod was cut from one $500\ \mu\text{m}$ thick tooth slice. This rod fits well into a cylinder less than $0.7\ \text{mm}$ in diameter and, therefore, allows for sub-micrometer resolution tomography. Figure 3 represents a series of nine slices perpendicular to the rod axis, which are $74\ \mu\text{m}$ apart from each other. The enamel given in light gray in the first two slices exhibits a stronger X-ray absorption than the dentin. Thus, enamel and dentin can be easily segmented. In these high-resolution edge-enhanced images the enamel does not exhibit a homogeneous X-ray absorption as in the X-ray imaging presented above and well known from conventional X-ray imaging techniques but certain variations in composition that includes very few tubular microstructures.

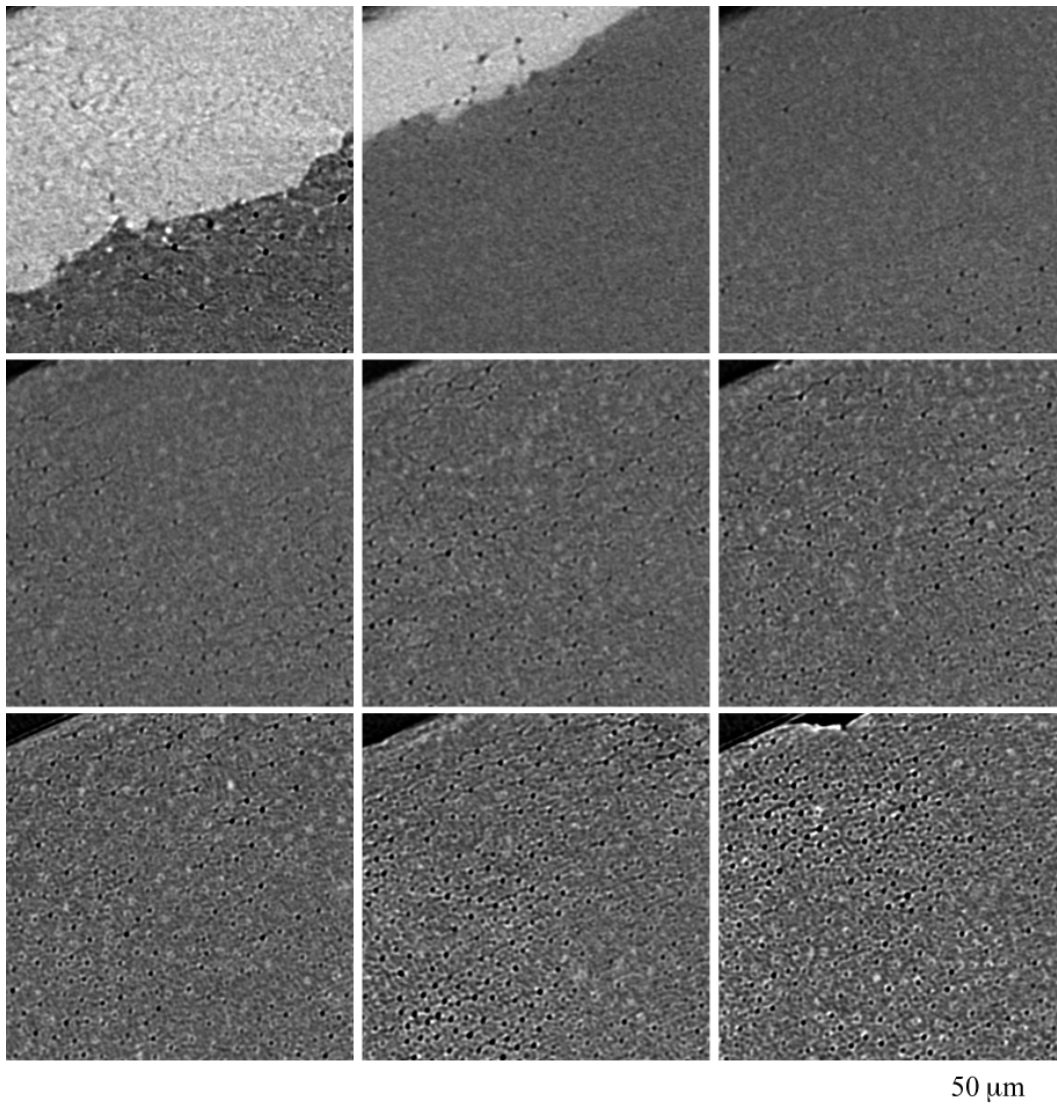


Fig. 4. The series of slices shows the density distribution of the tubules, which becomes smaller and smaller towards the dentin-enamel junction. The distance between the slices corresponds to $74\ \mu\text{m}$ each.

Within the dentin structure thousands of tubules are visible. The density of these tubules, however, varies and depends on the distance to the dentin-enamel junction. In general, the tubule density decreases towards the interface to the enamel, as indicated in Figures 4 and 5.

Figure 5 shows the density distribution of the tubules, which are oriented in a parallel manner. Here, the distance between the slices also corresponds to $74\ \mu\text{m}$. It is also recognized in Figure 5 that although the tubules are usually parallel, their orientation can change to become perpendicular to the dentin-enamel junction.

The tubules do not appear as simple cavities, which would become visible as very thin black cylinders. Almost each tubule contains a bright halo with a thickness of one or two micrometers.

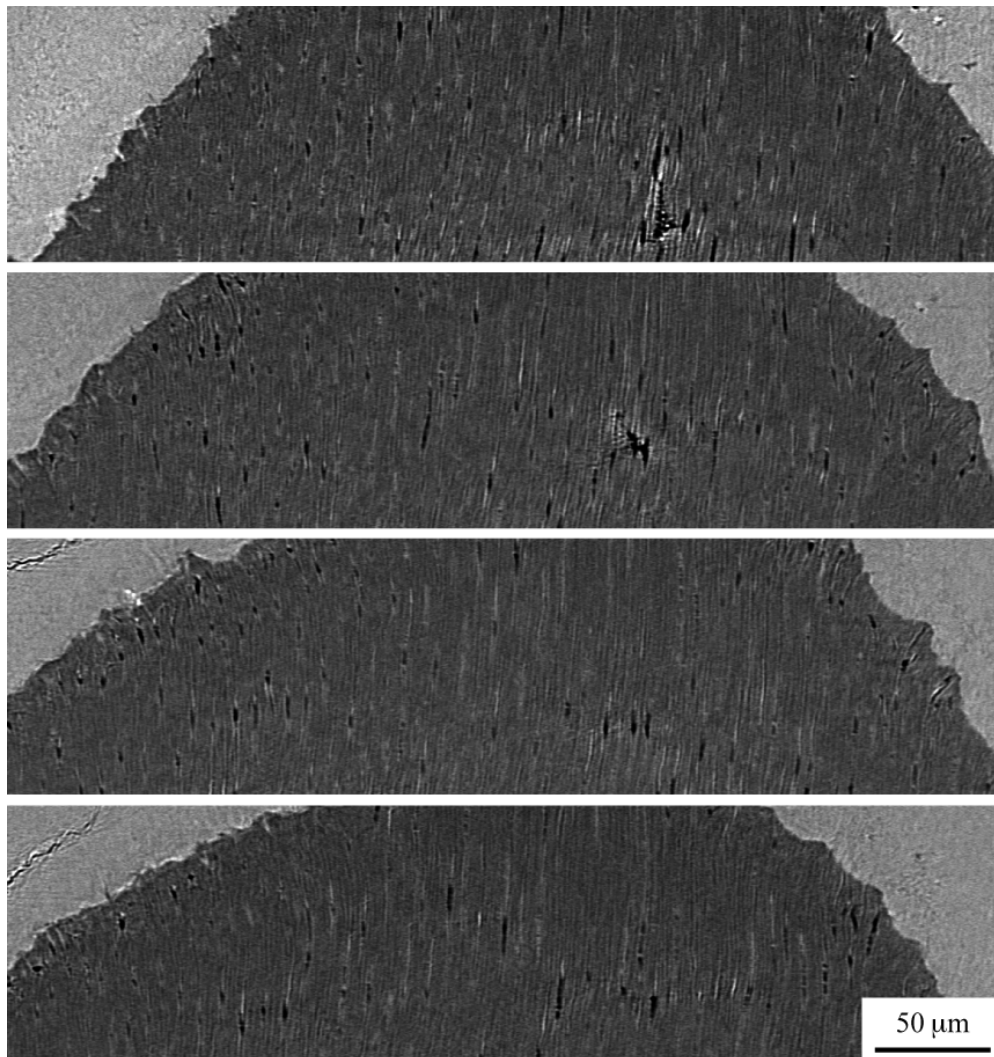


Fig. 5. The series of selected slices parallel to the tooth axis demonstrates the parallel orientation of the tubules within the dentin. Their density is reduced towards the dentin-enamel junction. The crack in the enamel is attributed to a preparation artifact.

3.3 Nanostructure of enamel and dentin

The SAXS measurements prove the preferential orientation of the nanostructures present in dentin and enamel. Figure 6 shows the cut perpendicular to the tooth axis. The nanostructures in the dentin are hardly ordered as indicated by the gray color. Only in the 20 nm range the nanostructures are oriented towards the growth direction. The light color, however, indicates that the number of scatters is rather weak. For the 20 nm range, however, one can differentiate between two different kinds of dentin. The inner part of the tooth contains more scatter centers, which are less ordered, whereas the part towards the enamel exhibit better ordered nanostructures of rather small density.

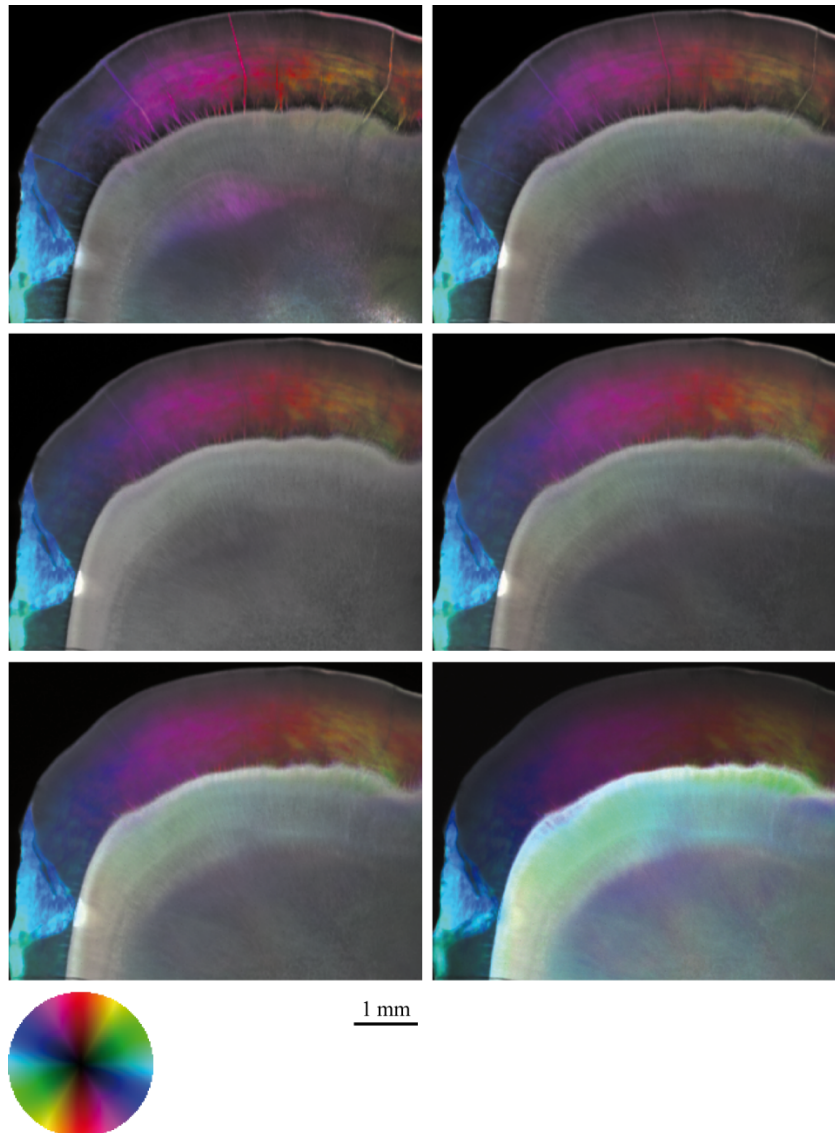


Fig. 6. The representation of the SAXS measurement demonstrates that nanostructures within dentin and enamel are often oriented from the center of the tooth towards the periphery. The images are obtained for the different length scales: 14 to 24 nm (top, left), 24 to 39 nm, 40 to 52 nm, 53 to 71 nm, 73 to 173 nm and 185 to 231 nm (bottom, right). The colored circular area denotes the orientation of the scattered intensity.

The enamel contains much more nanometer-sized features than the dentin in the range between 10 and 200 nm. They are clearly oriented in the central part, best seen within the 200 nm range. Although, there exist close similarities between the different nanometer scales, only the larger nanostructures show prominent features that are even crack-like traveling through the whole enamel structure of the tooth. The turquoise colored part on the left side of the images belongs to the characteristics of this particular slice. This part is significantly thinner, because a part of the enamel was broken off during the preparation of the slice.

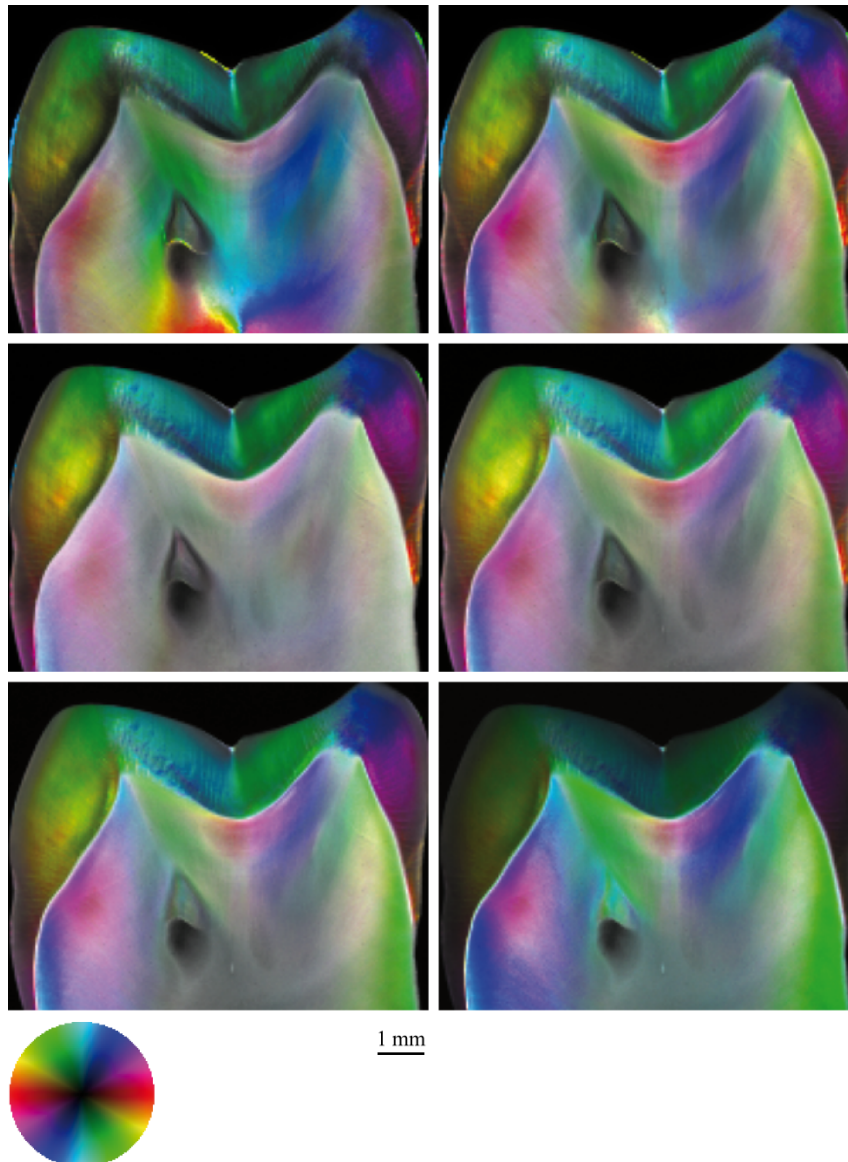


Fig. 7. The representation of the SAXS data parallel to the tooth axis reveals a preferential orientation of features in the range between 10 and 200 nm for both enamel and dentin. The orientation, however, is significantly different for both hard tissue components. The images are obtained for the different length scales: 14 to 24 nm (top, left), 24 to 39 nm, 40 to 52 nm, 53 to 71 nm, 73 to 173 nm and 185 to 231 nm (bottom, right).

The SAXS data of Figure 7 are obtained from a slice parallel to the tooth axis with a thickness of (270 ± 10) μm . In comparison to Figure 6 it demonstrates that the nanostructures of the hard tissues of the tooth are mainly oriented from top to bottom.

The SAXS experiments allow discriminating between enamel and dentin, since the nanostructures of the same frequencies are oriented in different directions. Nanostructures of the enamel that are below 24 nm do not exhibit the preferential orientation as observed among the larger ones. The color-coded images further uncover that the nanostructures within certain limits abruptly change their orientation at the dentin-enamel junction. Analyzing the SR μ CT data of the tooth slices, it is concluded that the transparent line on the left side of the tooth resulted from the interface between of dentin and enamel with rather irregular nanostructures. The abrasion on the left part of the tooth does not affect the orientation of the adjacent nanostructures.

4. DISCUSSION AND CONCLUSIONS

Conventional X-ray imaging techniques allow extracting the tooth geometry and the intensity-based segmentation [15] of dentin and enamel. The spatial and density resolution, however, are insufficient to uncover the micro- and the nanostructure of teeth tissues. The quantitative determination of the composition is especially demanding [16], since the dentin belongs to biological tissues with related diversification and property variations. Tomography with true micrometer resolution permits the visualization of the dentin tubules [17, 18]. Contrary to electron microscopy the tomographic imaging allows visualizing the tubules in the three-dimensional space and not only at the surface. Hence, the density and orientation of the tubules are quantitatively accessible. The bright halo of the tubules can be attributed to the enhanced density around each tubule and/or to the edge enhancement as the result of the coherent X-ray beam. In the slices of Figure 5 some cracks within the enamel are recognized. Such cracks are probably the result of the imperfect preparation procedure.

The current investigations reveal strong anisotropic morphologies of dentin and enamel on the micro- and nanometer scale. The orientation of the tubules follows the growth direction that corresponds to the main direction of mechanical loading. The SAXS data, which uncover the nano-architecture of the hard tissues, also show preferential orientation towards the growth directions. Interestingly, the orientations of the nanostructures within the dentin and the enamel are altered. Within certain regions, the nanostructures are almost perpendicular to each other at the dentin-enamel junction.

This fundamental knowledge should be applied for the development of biologically inspired dental fillings, i.e. to realize man-made materials with a micro- and nano-architecture similar to enamel and dentin. If caries has significantly damaged the enamel and dentin of the tooth, the dentist removes the damaged part and re-builds it by means of conventional isotropic dental composite materials that do not resemble the anisotropic structure of human teeth. The use of such a material that tends to shrink is also the reason, why the dentist usually removes more enamel than really necessary. Overhangs, as represented in Figure 8, are generally avoided to prevent the potential cracking. Therefore, improved fillings are highly desirable to achieve better results by less invasive treatment modalities.

The challenge for the realization of the biologically inspired fillings lies in the arrangement of the nanometer-sized building blocks. At least two different layers, namely for the dentin and for the enamel have to be foreseen in order to achieve the different preferential orientation of the nanostructures.

One could imagine various approaches to imitate the hard tissues of the human teeth. For example, crystalline growth processes, which take place at non-equilibrium conditions with gradients in temperature or concentration, give rise to nanostructures with strong anisotropies [19]. Unfortunately such processes are difficult to be controlled and, hence, impractical for patient treatment. Furthermore, one could apply fiber composites as already successfully incorporated into dental posts. The appropriate orientation of the fibers, however, is demanding. Building blocks of charged or dipolar units such as dedicated carbon nano-tubes would result in parallel arrangements of the nanostructures. The dashed curves in Figure 8 represent the potential arrangements of charged nano-tubes. Because of the charge, the nano-tubes exhibit a repulsive interaction that leads to almost parallel equidistant alignments [20]. Such dental fillings should have superior resistance to thermal and mechanical shocks as known from the hardest substance in the human body – the enamel.

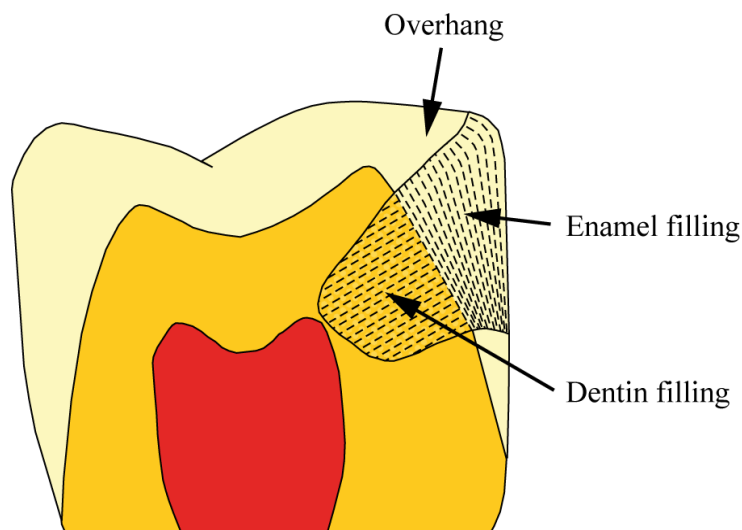


Fig. 8. The biomimetic and biologically inspired dental fillings should contain nanostructures such as charged carbon nanotubes that become aligned because of the repulsive interactions. Their size and orientation should be analogue to the undamaged dentin and enamel.

ACKNOWLEDGEMENTS

The beamtime at the synchrotron radiation facilities was kindly provided within the approved proposals I-20080224 EC (HASYLAB at DESY) and 20080959 (SLS at PSI). The technical support of F. Schmidli (Basel) for the tooth preparation and characterization is gratefully acknowledged.

REFERENCES

- [1] V. Imbeni, J. J. Kruzic, G. W. Marshall *et al.*, "The dentin–enamel junction and the fracture of human teeth," *Nature Materials*, 4, 229-232 (2005).
- [2] M. Al-Jawad, A. Streuwer, S. H. Kilcoyne *et al.*, "2D mapping of texture and lattice parameters of dental enamel," *Biomaterials*, 28, 2908-2914 (2007).
- [3] J. H. Kinney, J. A. Pople, G. W. Marshall *et al.*, "Collagen orientation and crystallite size in human dentin: a small angle X-ray scattering study," *Calcif. Tissue Int.*, 69, 31-37 (2001).
- [4] O. Bunk, M. Bech, T. H. Jensen *et al.*, "Multimodal X-ray scatter imaging," submitted, (2009).
- [5] S. Drews, F. Beckmann, J. Herzen *et al.*, [Comparative micro computed tomography study of a vertebral body] SPIE, San Diego (2008).
- [6] A. Papadimitropoulos, S. Friess, F. Beckmann *et al.*, [Comparative study of desktop- and synchrotron radiation-based micro computed tomography analyzing cell-seeded scaffolds in tissue engineering of bone] SPIE, San Diego (2008).
- [7] F. Beckmann, [Microtomography using synchrotron radiation as a user experiment at beamlines BW2 and BW5 of HASYLAB at DESY] SPIE, San Diego, USA (2002).
- [8] B. Müller, R. Bernhardt, T. Weitkamp *et al.*, "Morphology of bony tissues and implants uncovered by high-resolution tomographic imaging," *Int J Mat Res*, 98(7), 613-621 (2007).
- [9] A. C. Kak, and M. Slaney, [Principles of Computerized Tomographic Imaging] IEEE Press, New York (1988).
- [10] P. Thurner, F. Beckmann, and B. Müller, "An optimization procedure for spatial and density resolution in hard X-ray micro-computed tomography," *Nucl. Instrum. Meth.*, 225(4), 599-603 (2004).
- [11] B. Müller, P. Thurner, F. Beckmann *et al.*, [Non-destructive three-dimensional evaluation of biocompatible materials by microtomography using synchrotron radiation] SPIE, San Diego, USA (2001).

- [12] M. Stampanoni, A. Groso, A. Isenegger *et al.*, [Trends in synchrotron-based tomographic imaging: the SLS experience] SPIE, San Diego, USA (2006).
- [13] O. Paris, "From diffraction to imaging: New avenues in studying hierarchical biological tissues with x-ray microbeams," *Biointerphases*, 3(2), FB16-FB26 (2008).
- [14] P. Kraft, A. Bergamaschi, C. Broenimann *et al.*, "Performance of single-photon-counting PILATUS detector modules," *J. Synchrotron Rad.*, 16, 368-375 (2009).
- [15] B. Müller, F. Beckmann, M. Huser *et al.*, "Non-destructive three-dimensional evaluation of a polymer sponge by micro-tomography using synchrotron radiation" *Biomolecular Engineering*, 19, 73-78 (2002).
- [16] F. Kernen, T. Waltimo, H. Deyhle *et al.*, [Synchrotron radiation-based micro computed tomography in the assessment of dentin de- and re-mineralization] SPIE, San Diego (2008).
- [17] S. Zabler, P. Cloetens, and P. Zaslansky, "Fresnel-propagated submicrometer x-ray imaging of water-immersed tooth dentin," *Optics Lett.*, 32(20), 2987-2989 (2007).
- [18] S. R. Stock, A. E. M. Vieira, A. C. B. Delbem *et al.*, "Synchrotron microComputed Tomography of the mature bovine dentinoenamel junction," *J. Structural Biol.*, 161(2), 162-171 (2008).
- [19] B. Müller, "Natural formation of nanostructures: from fundamentals in metal heteroepitaxy to applications in optics and biomaterials science," *Surf. Rev. Lett.*, 8(1/2), 169-228 (2001).
- [20] J. V. Barth, J. Weckesser, C. Cai *et al.*, "Building supramolecular nanostructures at surfaces by hydrogen bonding," *Angewandte Chemie – Int. Ed.*, 39, 1230-1234 (2000).

2.2 Optimization of the three-dimensional visualization of tooth micro-structure

Phase and absorption contrast approaches are compared concerning spatial and density resolution as well as rendering of the dentin micro-structure. Single distance phase retrieval is proposed as best alternative.

Published in Proceedings of SPIE

Comparison of propagation-based phase-contrast tomography approaches for the evaluation of dentin microstructure

Hans Deyhle^a, Timm Weitkamp^{b,c}, Sabrina Lang^a, Georg Schulz^a, Alexander Rack^c, Irene Zanette^{b,d}, and Bert Müller^a

^aBiomaterials Science Center, University of Basel, Basel, Switzerland;

^bSynchrotron Soleil, Gif-sur-Yvette, France;

^cEuropean Synchrotron Radiation Facility, Grenoble, France;

^dDepartment of Physics, Technische Universität München, Garching, Germany

ABSTRACT

The complex hierarchical structure of human tooth hard tissues, enamel and dentin, guarantees function for decades. On the micrometer level the dentin morphology is dominated by the tubules, micrometer-narrow channels extending from the dentin-enamel junction to the pulp chamber. Their structure has been extensively studied, mainly with two-dimensional approaches. Dentin tubules are formed during tooth growth and their orientation is linked to the morphology of the nanometer-sized components, which is of interest for example for the development of bio-inspired dental fillings. Therefore, a method has to be identified that can access the three-dimensional organization of the tubules, e.g. density and orientation. Tomographic setups with pixel sizes in the sub-micrometer range allow for the three-dimensional visualization of tooth dentin tubules both in phase and absorption contrast modes. We compare high-resolution tomographic scans reconstructed with propagation-based phase retrieval algorithms as well as reconstructions without phase retrieval concerning spatial and density resolution as well as rendering of the dentin microstructure to determine the approach best suited for dentin tubule imaging. Reasonable results were obtained with a single-distance phase retrieval algorithm and a propagation distance of about 75% of the critical distance of d^2/λ , where d is the size of the smallest objects identifiable in the specimen and λ is the X-ray wavelength.

Keywords: Synchrotron radiation-based micro computed tomography, phase contrast, signal-to-noise ratio, spatial resolution, dentin tubules, tooth microstructure, Paganin phase retrieval, segmentation

1. INTRODUCTION

The complex hierarchical structure of human tooth hard tissues, i.e. enamel and dentin, guarantees tooth function for decades. At the macroscopic level, the interplay of hard, brittle enamel and softer and tougher dentin allows for masticatory forces of up to 380 N [1]. On the micrometer level, the most prominent features are the dentin tubules, micrometer-narrow channels running from the pulp chamber to the dentin-enamel junction (DEJ) in an *S*-shaped fashion. Locally, they can appear wavy and tilted with respect to each other. They are surrounded by the highly mineralized peri-tubular dentin (PTD) and embedded in the intra-tubular dentin. Dentin tubuli are formed during tooth growth and mark the path of the odontoblasts, which ultimately determine the shape of the tooth. Since remodeling in dentin is minimal, their orientation is linked to the organization of the nanometer-sized components such as collagen fibers and calcium phosphate crystallites deposited during tooth formation [2, 3]. These structures are of interest for example for the development of bio-inspired, anisotropic dental fillings with orientation dependent mechanical properties [4].

Dentin tubular structure [5–7] and its impact on the mechanical properties of dentin [8–10] have been studied with a wide variety of two-dimensional methods. These techniques often do not take into account local inhomogeneities related to tubule orientation. Therefore, a method has to be identified that gives access to the three-dimensional organization of the tubules. Tomographic setups with pixel sizes in the sub-micrometer range

Further author information: (Send correspondence to H.D.)

H.D.: E-mail: hans.deyhle@unibas.ch, Telephone: +41 61 265 9127

Developments in X-Ray Tomography VIII, edited by Stuart R. Stock,
Proc. of SPIE Vol. 8506, 85060N · © 2012 SPIE · CCC code: 0277-7864/12/\$18
doi: 10.1117/12.929951

allow for the three-dimensional (3D) visualization of tooth dentin tubules both in phase [11, 12] and absorption contrast modes [4, 13, 14]. Because of the small voxel size in these datasets, only small parts of a tooth, below approximately 1 mm in diameter, can be imaged simultaneously. Thus, for a complete understanding of the 3D organization of the tubular structure of dentin, scans of multiple thin specimens obtained from one tooth would be necessary from the present point of view. It is therefore desirable to identify the approach which allows one to image dentin tubules with the necessary spatial resolution as well as within reasonable scan time.

Absorption contrast is well suited for hard tissues such as bone or teeth, especially in a dry environment, due to the relatively high contrast of calcified tissues with respect to air, and thus suited for porous systems of these materials. Phase contrast techniques are particularly sensitive to interfaces, and therefore suitable for the detection of voids in an otherwise more or less homogeneous matrix, as is the case of dentin tubules, especially since exact information of dentin density is not needed.

Among X-ray phase contrast methods, grating interferometry (*GI*) excels due to its high density resolution [15], but it has only moderate spatial resolution [16]. It is therefore less suitable for imaging dentin tubuli. On the other hand, propagation-based (*PB*) phase contrast gives access to micrometer resolution [17]. In the present study we therefore investigated *PB* imaging approaches, which are based on phase contrast generated by the propagation of X rays in free space between specimen and detector. Phase retrieval was applied to the *PB* data with a multi-distance approach, frequently termed holotomography (*HT*) [18], and a single distance phase retrieval (*SDPR*) approach where the phase profile of the X-ray wavefront exiting plane of the specimen can be recovered from only a single radiograph, using an algorithm presented by Paganin *et al.* [19]. The algorithm assumes that monochromatic radiation illuminates a homogeneous object, a condition that is sufficiently fulfilled in the case of synchrotron radiation from a multilayer monochromator and dentin. In addition, the data acquired at different specimen-detector distances was reconstructed without phase retrieval.

The experimental data were compared concerning their spatial and density resolution, and rendering of the dentin microstructure, to determine the approach best suited for dentin tubule imaging and analysis. This knowledge is a prerequisite for the development of bio-inspired dental fillings or bio-inspired crown reconstructions.

2. MATERIALS AND METHODS

2.1 Specimen preparation

A $600 \times 400 \mu\text{m}^2$ thin rod was cut in the apical-cervical direction from the center of a human third molar, extracted for clinical reasons, with a diamond band saw (Exakt Apparatebau GmbH, Norderstedt, Germany). Enamel and a thin section of dentin below the DEJ were removed. The rod was dried in air prior to measurement.

2.2 Synchrotron radiation-based micro computed tomography

SR μ CT measurements were performed at the beamline ID19 [20] at the European Synchrotron Radiation Facility (ESRF, Grenoble, France). The photon energy was set to 17.6 keV with a multilayer monochromator [20]. 1500 projections of 2048×2048 pixels each and a pixel size of $0.33 \mu\text{m}$ were acquired at equidistant angular positions over 180° while the specimen was continuously rotated. The exposure time for each projection was 1 s. Four scans were performed at distances z between specimen and detector of 3, 6, 9 and 20 mm.

2.3 Data treatment

2.3.1 Holotomography

Phase retrieval exploits the intensity modulations of the wavefront due to phase shifts caused by the specimen and subsequent propagation of the beam from specimen to detector. In the *HT* approach the phase shifts are determined from multiple projections acquired at different specimen-detector distances z [18]. For the phase retrieval from the four sets of data a mixed approach was chosen, which combines the contrast transfer function and the transport-of-intensity equation [21–23]. This algorithm is valid for non-zero specimen absorption and extended propagation distances. To reduce low-frequency artifacts, which can arise from the fact that the transfer function for phase contrast is small in the low spatial frequency range, the low-frequency components of the phase profile are assumed to be proportional to the logarithm of the projected intensity transmission via a

fixed estimate of the ratio δ/β of refractive index decrement over absorption coefficient [23]. A value of $\delta/\beta = 300$ was chosen, which yielded reasonable results even though it differs from the theoretical value of 130 at 17.6 keV [24].

2.3.2 Single distance phase retrieval

The phase profile of the X-ray wavefront exiting the plane of the specimen can be recovered from only a single radiograph under the assumption of a single material specimen and monochromatic illumination [19, 25]. Phase retrieval from single distance data was performed using the software *ANKAphase* [25] which is based upon an algorithm presented by Paganin *et al.* [19]. *ANKAphase* requires δ and β , the decrement of the real part of the refractive index and its imaginary part respectively, of the material to be known. The quality of the results is, however, only dependent on the ratio δ/β , while the absolute values of the two coefficients only result in a proportional scaling factor of the results. For processing, $\delta = 1.004 \cdot 10^{-6}$ and $\beta = 7.74 \cdot 10^{-9}$ were chosen, which are the δ and β values of hydroxy-apatite of $1.5 \text{ g}\cdot\text{cm}^{-3}$ density at 17.6 keV photon energy [24], resulting in a δ/β ratio of 130. Single distance phase retrieval was performed for the four acquired scans from the holotomography.

2.3.3 Tomographic reconstruction

All tomographic datasets were reconstructed using a filtered backprojection algorithm implemented in Matlab[®] (2010b, The MathWorks, Natick, USA).

3. RESULTS AND DISCUSSION

3.1 Density and spatial resolution

Figure 1 on the left shows a selected cross-section from the *HT* dataset of a tooth rod with a diameter of $500 \mu\text{m}$. Despite the presence of prominent ring artifacts, the dentin can be described as rather homogeneous material, with the characteristic texture dominated by the dentin tubules. The white square indicates the region of interest (ROI) shown in the central panel of Figure 1. Here, the dentin tubules can be clearly identified as dark spots with a diameter between 1 and $2 \mu\text{m}$, partially surrounded by structures with higher $\Delta\delta$. It is unclear whether these arise from electron density variations inside the dentin or are artifacts caused by specimen movement during the tomographic acquisition. The plot on the right shows the histogram of the 3D dataset. The peaks corresponding to air and dentin were individually fitted with Gaussians and are clearly separated. The shoulder on the left side of the dentin-related peak contains the dentin tubules, which exhibit intensities close to that of dentin due to the partial volume effect caused by the similar size of the tubules compared to the pixel size.

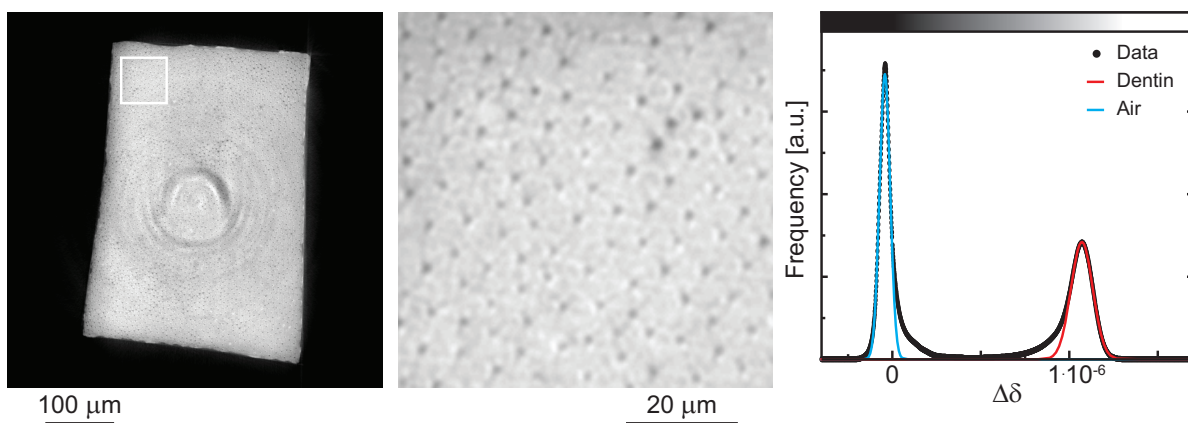


Figure 1. On the left, reconstructed slice of a $500 \mu\text{m}$ -thin tooth rod. The dentin appears speckled due to the presence of dentin tubules. In the center, magnified region according to the white square on the left. The dentin tubules can be clearly identified as dark spots. On the right, the histogram of the volumetric dataset. Air and dentin are clearly separated. The shoulder on the left of the dentin peak contains the dentin tubules, which exhibit intensities close to that of dentin due to the partial volume effect caused by the small size of the tubules, close to the pixel size of $0.33 \mu\text{m}$.

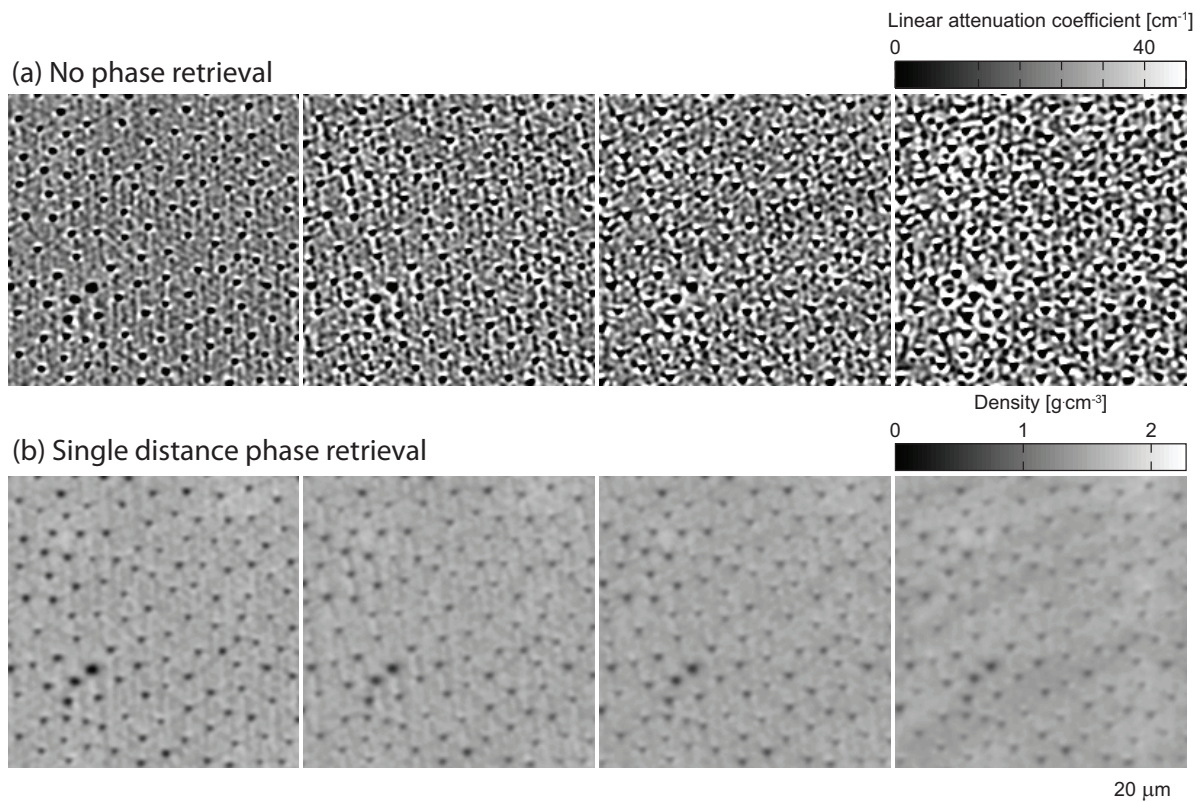


Figure 2. Detail of the specimen according to Figure 1. On the top line from left to right, a part of a selected slice from the data reconstructed without phase retrieval from the four measured distances (3, 6, 9 and 20 mm specimen-detector distance) are shown. Pronounced edge enhancement can be seen, it increases with specimen-detector distance. On the bottom line from left to right, the same region of the slice from the single distance phase retrieval data from the four measured distances. Note the increasing blurriness of the dentin tubules with longer specimen-detector distance.

Figure 2 shows, on the top row, a ROI of the data reconstructed without phase retrieval, acquired at the four specimen-detector distances 3, 6, 9 and 20 mm, from left to right respectively. The location of the ROI is defined in Figure 1. The dentin tubules can be identified as dark spots in the surrounding dentin matrix. While the dentin looks rather homogeneous in the data acquired at $z = 3$ mm, increasingly prominent bright structures surrounding the tubules, caused by edge enhancement, appear with increasing z , and inhomogeneities in the dentin increase. Zabler *et al.* showed that void tubules surrounded by a highly mineralized *PTD* give rise to dark spots surrounded by bright structures after free-space propagation of the X-rays if the radius of the *PTD* is at least 1.67 times as large as the radius of the void tubule [26]. The intensity of the bright rings is reported to increase with increasing propagation distance, in good agreement with our results. In the case of void tubules not surrounded by *PDT* they reported the presence of a bright spot at the position of the tubule after propagation. However, this case did not occur in the data presented here.

The bottom row shows the same ROI reconstructed from single distance phase retrieval projections. The tubules can be clearly identified in the leftmost image (3 mm specimen-detector distance) and become more and more blurry with increasing propagation distance.

Structures corresponding to the dentin tubules can be identified in the data of all imaging approaches even though their size and appearance vary depending on acquisition mode and z . It is therefore difficult to determine which approach offers the most accurate representation. A more thorough inspection of the spatial and density resolution of the datasets will allow for the choice of the most suited method.

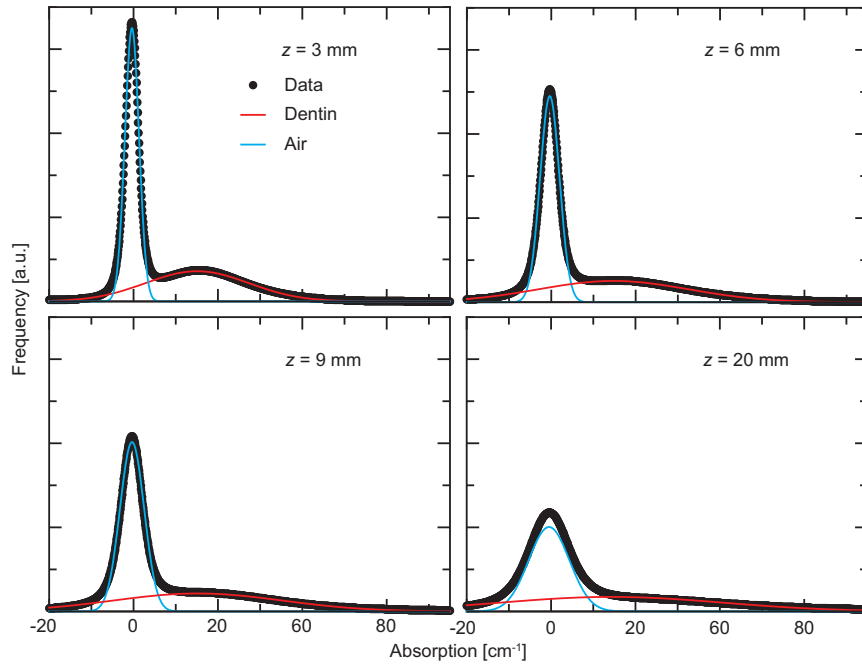


Figure 3. Histograms from the datasets reconstructed without phase retrieval, measured at the four specimen-detector distances 3, 6, 9 and 20 mm. The peak corresponding to dentin largely overlaps with the air-related peak and becomes broader with increasing specimen-detector distance while peak position remains largely unaffected.

Figures 3 and 4 show the attenuation coefficient and reconstructed density histograms (*SDPR* data) of the 3D data, respectively, for the four specimen-detector distances. The peaks corresponding to air and dentin were fitted individually with Gaussians (pro Fit 6.2.0, Quantum Soft, Uetikon am See, Switzerland). The dentin-related peak from the data reconstructed without phase retrieval is almost an order of magnitude wider compared to the one related to the surrounding air. The width of both peaks increases with increasing z , indicating a degradation of density resolution. For the *SDPR* data, however, the width of the dentin-related peak slightly decreases with increasing distance, from 0.22 full width at half maximum (FWHM) to 1.67 FWHM, as determined from the Gaussian fits (cp. Fig. 4), except for the last distance, where it increases to 0.23 FWHM. Therefore one expects an improvement in density resolution with increasing distance for this approach. The comparison of the histograms of the three approaches suggests that the large width of the dentin peak in the data reconstructed without phase retrieval does not originate solely from material inhomogeneities, but is rather a combination of X-ray absorption variations in the dentin and phase effects, e.g. edge enhancement.

To quantify the density resolution of the datasets, Herzen *et al.* [27] proposed the contrast-to-noise ratio (CNR) defined as

$$\text{CNR} = \frac{|S_a - S_d|}{\sqrt{\sigma_a^2 + \sigma_d^2}} \quad (1)$$

where S_a and S_d are the peak positions (cp. Figs. 3 and 4) of the measured quantities corresponding to two different homogeneous materials, and σ_a and σ_d are the standard deviations in regions of equal volume inside these materials. Unfortunately, this approach is not directly applicable to the datasets discussed here since it requires two homogeneous media for the calculation of the standard deviations. Dentin can not be considered homogeneous for this purpose. Peri-tubular dentin and intra-tubular dentin are known to possess different degrees of calcification, and thus different densities. In addition, the high number of tubules present makes the selection of a volume containing only dentin difficult. Therefore the approach chosen by Schulz *et al.*

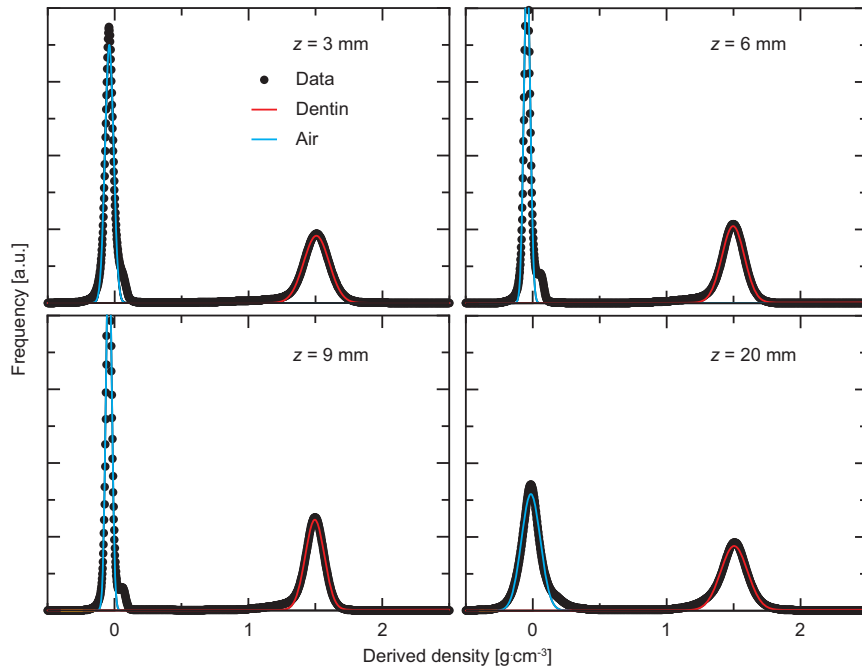


Figure 4. Single distance phase retrieval histograms from the datasets measured at the four specimen-detector distances 3, 6, 9 and 20 mm. The width of the dentin-related peak decreases from distance 1 through distance 3 while increasing again at distance 4.

[28] was applied, where only the standard deviation σ_a of the medium surrounding the specimen is considered. The single material contrast-to-noise ratio, CNR_{sm} is therefore defined as

$$\text{CNR}_{sm} = \frac{|S_a - S_d|}{\sigma_a} \quad (2)$$

where S_d is the peak position of dentin, S_a the peak position of air and σ_a the standard deviation in a ROI in air. The CNR_{sm} are resumed in table 1. CNR_{sm} steadily decreases for the data reconstructed without phase retrieval with increasing specimen-detector distance. This is caused by the increased width of the air related peak, and therefore σ_a . We assume this is related to the appearance of streak-like noise which arises from the back projection of the enhanced edges in the specimen caused by longer propagation distances of the X rays between specimen and detector [29,30]. On the contrary, CNR_{sm} increases up to 9 mm specimen-detector distance in the *SDPR* data, while only the data at the maximal distance of 20 mm shows degraded density resolution. The algorithm proposed by Paganin *et al.* [19] is derived on the assumption that

$$z \ll \frac{d^2}{\lambda} \quad (3)$$

where z is the specimen-detector distance, d is the size of the smallest objects identifiable in the specimen and λ is the X-ray wavelength. For the present experiment $d \approx 1 \mu\text{m}$ and $\lambda = 0.705 \text{ \AA}$. Therefore, the z should not exceed 10 mm. However, the phase retrieval algorithm proves to be robust against deviations from the optimal conditions [31]. Even though the CNR_{sm} decreases drastically at 20 mm, individual tubules can still be identified (cp. Fig. 2).

It is evident that the phase retrieval-based data outmatch the data without phase retrieval concerning density resolution. The highest CNR_{sm} is obtained for single distance phase retrieval data at $z = 9 \text{ mm}$. It is almost a factor of 10 higher than one obtained from data reconstructed without phase retrieval acquired at $z = 3 \text{ mm}$. Density resolution of the *HT* lies between the two methods discussed.

Table 1. Single material contrast-to-noise ratio CNR_{sm} for the investigated imaging approaches. z : specimen-detector distance, *SDPR*: single-distance phase retrieval.

Imaging approach	$z = 3$ mm	$z = 6$ mm	$z = 9$ mm	$z = 20$ mm
Without phase retrieval	9.2	6.6	5.4	3.1
<i>SDPR</i>	48.8	66.3	72.4	21.5
Holotomography	37.4			

To investigate the spatial resolution of the datasets, taking into consideration the properties of the specimen and experimental setup, the radial spectral power distribution (RSP) of a small region of the specimen of $201 \times 201 \times 201$ voxels was calculated and normalized by the RSP of a region of the same size containing air. The spatial resolution was defined as the highest spatial frequency where the normalized RSP had twice the baseline value [32, 33]. Table 2 lists the spatial resolution of the datasets.

The data reconstructed without phase retrieval yields the best spatial resolution among the investigated approaches in this study, ranging from $1.13 \mu\text{m}$, which correspond to 3.4 pixels, at the shortest z to $1.36 \mu\text{m}$, corresponding to 4.1 pixels, at $z = 20$ mm. Spatial resolution of the *SDPR* data is found to be slightly degraded compared to the data reconstructed without phase retrieval. The difference between the two methods is however not as drastic as in the case of the CNR_{sm} . The origin of the improved spatial resolution in the *SDPR* data for $z = 20$ mm is unclear. As should be expected, the spatial resolution in both approaches does not reach the theoretically optimal resolution limit imposed by the width of the first Fresnel zone of a point-like object in the specimen, given by $\sqrt{\lambda \cdot z}$, indicating that there are no spurious multiple fringes around object features, which would generate higher frequency contributions to the *RSP*. The resolution limit for the four specimen-detector distances z is also resumed in Table 2.

Table 2. Spatial resolution determined from the radial spectral power distribution for the investigated imaging approaches. Resolution is given in μm . z : specimen-detector distance, *SDPR*: single-distance phase retrieval. *Resolution limit* indicates the expected spatial resolution limit given by the width of the first Fresnel zone.

Imaging approach	$z = 3$ mm	$z = 6$ mm	$z = 9$ mm	$z = 20$ mm
Without phase retrieval	1.13	1.15	1.17	1.36
<i>SDPR</i>	1.67	1.88	2.13	1.86
Resolution limit	0.46	0.65	0.80	1.19
Holotomography	1.39			

The values for spatial resolution obtained by the RSP analysis (Table 2) are slightly better for the images obtained without phase retrieval than for the *SDPR* images. This is consistent with what should be expected because the *SDPR* phase reconstruction effectively acts as a low-pass filter on the spatial frequency spectrum of the data [19]. For the *SDPR* data and the data obtained without phase reconstruction, the difference between the resolution values obtained by *RSP* analysis and the width of the first Fresnel zone decreases as the distance z increases. This is consistent with the expectations because at shorter distances z , the resolution should primarily be limited by experimental limitations as signal-to-noise ratio or detector resolution, whereas, at longer z , the Fresnel zone width should become the predominant resolution limit.

3.2 Tubule segmentation

Dentin tubules were segmented from the tomograms with a simple threshold approach and alternatively by filtering the individual slices with a second derivative kernel h :

$$h = \begin{pmatrix} 1 & 1 & 1 \\ 1 & -8 & 1 \\ 1 & 1 & 1 \end{pmatrix} \quad (4)$$

This filter was chosen since the the pixel size lies close to the characteristic size of the tubules which run perpendicular to the tomographic slices. After filtering, the slices were binarized to identify the pixels corresponding to tubules.

Since thresholding is related to image contrast, the first method was applied to the datasets of each imaging approach exhibiting the highest CNR_{sm} , while the second method, related to the presence of sharp edges, was applied to the datasets possessing highest spatial resolution. Figure 5 shows, on the top row, ROIs from the data reconstructed without phase retrieval, the *SDPR* data and the *HT* data, from left to right. The pixels corresponding to the segmented tubules are shown in red. For the data reconstructed without phase retrieval, the segmentation threshold was chosen as the absorption value where the Gaussians related to air and dentin intersect. For the propagation-based methods, the threshold was defined as the value where the Gaussian fitted to the dentin-related peak reaches 10% of its maximum value. The bottom row of Figure 5 shows, analogously, the tomographic datasets and, superimposed in red, the tubules segmented with the filter approach.

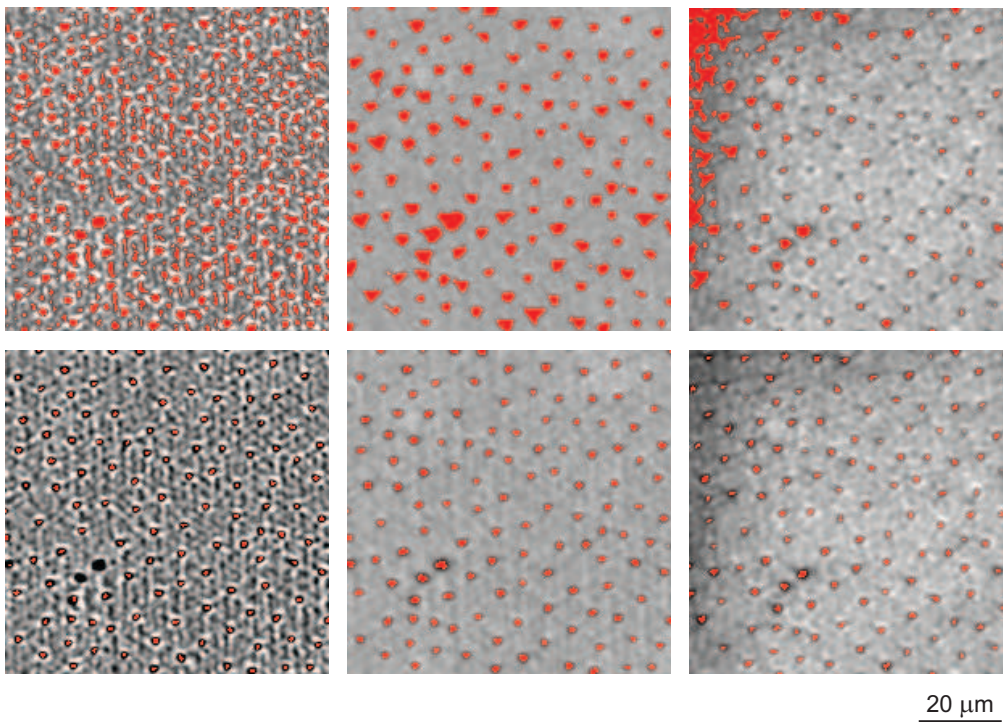


Figure 5. In the top row, from left to right, ROIs from the data reconstructed with no phase retrieval ($z = 3$ mm), with *SDPR* ($z = 9$ mm) and *HT*. Segmented dentin tubules (in red) were superimposed to the tomograms. In the top row, a thresholding approach was chosen for segmentation. In the bottom row, ROIs from the data reconstructed with no phase retrieval ($z = 3$ mm), with *SDPR* ($z = 3$ mm) and *HT* are shown, analogously. Segmentation was performed with a second derivative filtering and subsequent thresholding.

Segmentability through thresholding is in reasonable agreement with the CNR_{sm} values, i.e. better contrast leads to better segmentability. Thresholding of the data reconstructed without phase retrieval leads to the inclusion of structures within the dentin due to the high inhomogeneity in the material, in agreement with the fact that the air- and dentin-related curves in Fig. 3 overlap. *SDPR* data after thresholding show satisfying

results concerning tubule position, however the mean tubule diameter is above those determined with the other approaches. We assume that through this segmentation procedure their size is overestimated. The spatial resolution of the shown dataset amounts to $1.7 \mu\text{m}$, which is near the mean diameter of the tubules. The tubule edges do therefore not appear sharp and are smeared over the complete area of the tubules and surrounding dentin. Thus, the tubules exhibit a contrast value closer to dentin rather than air. The threshold was chosen to be high enough that the majority of tubules were segmented. The consequence is that an increased number of voxels is considered part of the tubules. A more conservative threshold would lead to a more precise estimation of tubule sizes, but on the other hand also be less sensitive to the smaller voids. Such an approach can be seen in the threshold-segmented *HT*-data (top-right in Fig. 5), where size and position of the larger tubules is segmented correctly, while smaller tubules remain undetected.

Segmentation based on the second derivative of the data yields overall better results than the threshold-based approach (bottom row of Fig. 5). The sharp edges in the tomogram of the data reconstructed without phase retrieval, related to the high spatial resolution, lead to an underestimation of the tubule size with the applied filter, and large tubules are not detected at all. A larger filter kernel could lead to an improvement of the segmentation. The blurriness of the *SDPR* data is, in this case, of advantage, since the tubule edges do not appear sharp. Therefore, larger structures are also segmented. This is also the case for the *HT* data, where position and size of all tubules can be extracted.

4. CONCLUSIONS

High-resolution SR μ CT is a suitable tool for the 3D imaging of human teeth, allowing for the rendering of the dentin tubules, which dominate the tooth microstructure. The propagation-based phase retrieval approaches offer increased density resolution compared to the data where no phase retrieval was performed, while still retaining sufficient spatial resolution for tubule identification. This has the advantage of a better representation of modulations in dentin density. Therefore, these approaches will often be preferred over reconstructions with no phase retrieval, since the complexity of the setup and data processing only slightly exceed those of measurements without phase retrieval. Since single distance phase retrieval and holotomography achieve comparable results, the manifold acquisition time in holotomography, caused by the necessity for multiple scans at different detector distances, makes *SDPR* the better alternative. The best results in this study are achieved with a propagation distance of about 75% of the critical distance of d^2/λ .

REFERENCES

- [1] Helkimo, E., Carlson, G. E., and Helkimo, M., "Bite force and state of dentition," *Acta Odontol. Scand.* **35**, 207–303 (1977).
- [2] Deyhle, H., Bunk, O., and Müller, B., "Nanostructure of healthy and caries-affected human teeth," *Nanomed-Nanotechnol.* **7**, 694–701 (2011).
- [3] Gaiser, S., Deyhle, H., Bunk, O., White, S. N., and Müller, B., "Understanding nano-anatomy of healthy and carious human teeth: A prerequisite for nanodentistry," *Biointerphases* **7**, 4 (2012).
- [4] Deyhle, H., Bunk, O., Buser, S., Krastl, G., Zitzmann, N. U., Ilgenstein, B., Beckmann, F., Pfeiffer, F., Weiger, R., and Müller, B., "Bio-inspired dental fillings," *Proc. SPIE* **7401**, 74010E (2009).
- [5] Schilke, R., Lisson, J. A., Bauss, O., and Geurtsen, W., "Comparison of the number and diameter of dentinal tubules in human and bovine dentine by scanning electron microscopic investigation," *Arch. Oral Biol.* **45**, 355–361 (2000).
- [6] Schellenberg, U., Krey, G., Bosshardt, D., and Nair, P. N. R., "Numerical density of dentinal tubules at the pulpal wall of human permanent premolars and third molars," *J. Endod.* **18**, 104–109 (1992).
- [7] Mjör, I. A. and Nordahl, I., "The density and branching of dentinal tubules in human teeth," *Arch. Oral Biol.* **5**, 401–412 (1996).
- [8] Nalla, R. K., Kinney, J. H., and Ritchie, R. O., "Effect of orientation on the in vitro fracture toughness of dentin: The role of toughening mechanisms," *Biomater.* **24**, 3955–3968 (2003).
- [9] Inoue, S., Pereira, P. N. R., Kawamoto, C., Nakajima, M., Koshiro, K., Tagami, J., Carvalho, R. M., Pashley, D. H., and Sano, H., "Effect of depth and tubule direction on ultimate tensile strength of human coronal dentin," *Dent. Mater. J.* **22**, 39–47 (2003).

- [10] Kinney, J. H., Marshall, S. J., and Marshall, G. W., "The mechanical properties of human dentin: A critical review and re-evaluation of the dental literature," *Crit. Rev. Oral Biol. Med.* **14**, 13–29 (2003).
- [11] Zabler, S., Cloetens, P., and Zaslansky, P., "Fresnel-propagated submicrometer X-ray imaging of water-immersed tooth dentin," *Opt. Lett.* **32**, 2987–2989 (2007).
- [12] Zaslansky, P., Zabler, S., and Fratzl, P., "3D variations in human crown dentin tubule orientation: A phase-contrast microtomography study," *Dent. Mater.* **26**, e1–e10 (2010).
- [13] Stock, S. R., Vieira, A. E. M., Delbem, A. C. B., Cannon, M. L., Xiao, X., and De Carlo, F., "Synchrotron microcomputed tomography of the mature bovine dentinoenamel junction," *J. Struct. Biol.* **161**, 162–171 (2008).
- [14] Parkinson, C. R. and Sasov, A., "High-resolution non-destructive 3D interrogation of dentin using X-ray nanotomography," *Dent. Mater.* **24**, 773–777 (2008).
- [15] Zanette, I., Weitkamp, T., Lang, S., Langer, M., Mohr, J., David, C., and Baruchel, J., "Quantitative phase and absorption tomography with an X-ray grating interferometer and synchrotron radiation," *Phys. Status Solidi A* **208**, 2526–2532 (2011).
- [16] Lang, S., Zanette, I., Dominiotto, M., Langer, M., Rack, A., Le Duc, G., David, C., Mohr, J., Pfeiffer, F., Müller, B., and Weitkamp, T., "Comparison of grating-based and propagation-based X-ray phase tomography of soft tissue," **in preparation** (2012).
- [17] Spanne, P., Raven, C., Snigireva, I., and Snigirev, A., "In-line holography and phase-contrast microtomography with high energy X-rays," *Phys. Med. Biol.* **44**, 741–749 (1999).
- [18] Cloetens, P., Ludwig, W., Baruchel, J., Van Dyck, D., Van Landuyt, J., Guigay, J. P., and Schlenker, M., "Holotomography: Quantitative phase tomography with micrometer resolution using hard synchrotron radiation X rays," *Appl. Phys. Lett.* **75**, 2912–2914 (1999).
- [19] Paganin, D., Mayo, S. C., Gureyev, T. E., Miller, P. R., and Wilkins, S. W., "Simultaneous phase and amplitude extraction from a single defocused image of a homogeneous object," *J. Microsc.* **206**, 33–40 (2002).
- [20] Weitkamp, T., Tafforeau, P., Boller, E., Cloetens, P., Valade, J.-P., Bernard, P., Peyrin, F., Ludwig, W., Helfenand, L., and Baruchel, J., "Status and evolution of the ESRF beamline ID19," *AIP Conf. Proc.* **1221**, 33–38 (2010).
- [21] Guigay, J., Langer, M., Boistel, R., and Cloetens, P., "Mixed transfer function and transport of intensity approach for phase retrieval in the Fresnel region," *Opt. Lett.* **32**, 1617–1619 (2007).
- [22] Langer, M., Cloetens, P., Guigay, J. P., and Peyrin, F., "Quantitative comparison of direct phase retrieval algorithms in in-line phase tomography," *Med. Phys.* **35**, 4556–4566 (2008).
- [23] Langer, M., Cloetens, P., and Peyrin, F., "Regularization of phase retrieval with phase-attenuation duality prior for 3D holotomography," *IEEE Trans. Image Proces.* **19**, 24282436 (2010).
- [24] "CXRO center for x-ray optics," http://henke.lbl.gov/optical_constants/getdb2.html .
- [25] Weitkamp, T., Haas, D., Wegrzynek, D., and Rack, A., "ANKAphase: software for single-distance phase retrieval from inline X-ray phase-contrast radiographs," *J. Synchrotron Rad.* **18**, 617–629 (2011).
- [26] Zabler, S., Riesemeier, H., Fratzl, P., and Zaslansky, P., "Fresnel-propagated imaging for the study of human tooth dentin by partially coherent x-ray tomography," *Opt. Express* **14**, 8584–8597 (2006).
- [27] Herzen, J., Donath, T., Pfeiffer, F., Bunk, O., Padeste, C., Beckmann, F., Schreyer, A., and David, C., "Quantitative phase-contrast tomography of a liquid phantom using a conventional X-ray tube source," *Opt. Express* **17**, 1001010018 (2009).
- [28] Schulz, G., Waschkies, C., Pfeiffer, F., Zanette, I., Weitkamp, T., David, C., and Müller, B., "Multimodal imaging of human cerebellum - merging X-ray phase microtomography, magnetic resonance microscopy and histology," **submitted** (2012).
- [29] Cloetens, P., Barrett, R., Baruchel, J., Guigay, J. P., and Schlenkerz, M., "Phase objects in synchrotron radiation hard X-ray imaging," *J. Phys. D* **29**, 133–146 (1996).
- [30] Snigirev, A., Snigireva, I., Kohn, V., Kuznetsov, S., and Schelokov, I., "On the possibilities of xray phase contrast microimaging by coherent high energy synchrotron radiation," *Rev. Sci. Instrum.* **66**, 5486–5492 (1995).

- [31] Myers, G. R., Mayo, S. C., Gureyev, T. E., Paganin, D. M., and Wilkins, S. W., “Polychromatic cone-beam phase-contrast tomography,” *Phys. Rev. A* **76**, 045804 (2007).
- [32] Modregger, P., D., Lübbert, Schäfer, P., and Köhler, R., “Spatial resolution in Bragg-magnified X-ray images as determined by Fourier analysis,” *Phys. Status Solidi A* **204**, 2746–2752 (2007).
- [33] Schulz, G., Weitkamp, T., Zanette, I., Pfeiffer, F., Beckmann, F., David, C., Rutishauser, S., Reznikova, E., and Müller, B., “High-resolution tomographic imaging of a human cerebellum: Comparison of absorption and grating based phase contrast,” *J. R. Soc. Interface* **7**, 1665–1676 (2010).

2.3 Collagen content in carious dentin

The bacterial processes dissolve the ceramic components in enamel and dentin, but a significant part of the dentinal collagen network remains unaffected with respect to its abundance and orientation in early stages of caries and in parts of extended carious lesions.

Published in Nanomedicine: Nanotechnology, Biology, and Medicine



CLINICALLY RELEVANT

Nanomedicine: Nanotechnology, Biology, and Medicine
7 (2011) 694–701



Short Communication

nanomedjournal.com

Nanostructure of healthy and caries-affected human teeth

Hans Deyhle, MSc^{a,b}, Oliver Bunk, PhD^b, Bert Müller, PhD^{a,*}

^aBiomaterials Science Center, University of Basel, Basel, Switzerland

^bPaul Scherrer Institut, Villigen, Switzerland

Received 11 April 2011; accepted 8 September 2011

Abstract

Spatially resolved small-angle x-ray scattering based on synchrotron radiation combines the quantitative assessment of nanometer-sized components using scattering with the real-space imaging by means of scanning. The method enables us to study the effect of caries-induced damages on the inorganic and organic nanoscopic components in human teeth. We demonstrate for several 200- to 500- μm -thin tooth slices that the bacterial processes dissolve the ceramic components in enamel and dentin, but the dentinal collagen network remains practically unaffected with respect to its abundance and orientation in early stages of caries and in parts of extended carious lesions. Consequently, we speculate that future caries treatments can be developed reversing the effect of bacterial attacks by means of suitable remineralization of the dentin.

From the Clinical Editor: In this groundbreaking study of caries pathology using synchrotron-based X-ray scattering, the authors demonstrated that while bacterial processes do dissolve the ceramic components in enamel and dentin; however, the dentinal collagen network remains unaffected, enabling the development of future caries treatments that re-mineralize the dentin.

© 2011 Elsevier Inc. All rights reserved.

Key words: Tooth nanostructure; Dentin; Dentinal collagen; Small-angle X-ray scattering; Synchrotron radiation

The hierarchical structure of the hard tissues of human teeth guarantees function for decades. Caries, the most frequent disease, is known to damage the enamel, the dentin, and the cementum through the production of acidic species that dissolve the ceramic tooth components as also observed in the dental erosion that habitually accompanies excessive citrus fruit consumption.¹ Unfortunately, the destroyed tooth structures do not fully regenerate, although remineralization of small carious lesions occurs under optimized dental hygiene.²

The treatment of carious lesions is nowadays accompanied by the removal of affected hard tissues. The progression of caries is enhanced in the dentin in comparison with the progression in the enamel. The faster spread through the dentin is generally visible in sections or projections as triangles with their basis along the enamel-dentin junction.³ Therefore, dentists are regularly forced to amputate not only the massively damaged enamel, but also a significant amount of healthy enamel to guarantee the complete substitution of carious dentin by the restoration material. As the current restoration materials do not fully fit the performance of the natural healthy hard tissues, the resulting limited lifespan renders further interventions necessary.^{4,5} The dentin not only consists of ceramic compo-

nents, but also of about 20 wt% organic material.⁶ It has been hypothesized that the organic components, in particular the collagen, may remain unaffected. This hypothesis is based on electron microscopy inside carious lesions, which proves the strong similarity between collagen in selected healthy and caries-affected regions.⁷ Furthermore, it has been speculated that the remaining collagen network can provide nucleation sites for remineralization.^{8,9} To prove the hypothesis an imaging method has to be identified that allows comparing the collagen abundance in healthy and caries-affected parts of a tooth. Spatially resolved small-angle x-ray scattering (SAXS) is a technique that enables the identification of collagen using its 67-nm periodicity¹⁰ over extended areas with resolution in the micrometer range, i.e., about 40,000 scattering patterns per square centimeter.¹¹ Because the patterns are average values of the illuminated volume along the x-ray beam, the contributions from the surfaces are negligible and the potential influence of artifacts from cutting several 100- μm -thick slices is small. Consequently, scanning SAXS is well suited for the structural characterization of tooth slices over the entire nanometer range.

Methods

Eight teeth, five carious and three healthy, were extracted for clinical reasons and cut into 200- to 500- μm -thin slices

No conflict of interest is reported by the authors.

*Corresponding author: Biomaterials Science Center, c/o University Hospital Basel, 4031 Basel, Switzerland.

E-mail address: bert.mueller@unibas.ch (B. Müller).

1549-9634/\$ – see front matter © 2011 Elsevier Inc. All rights reserved.
doi:10.1016/j.nano.2011.09.005

Please cite this article as: H. Deyhle, O. Bunk, B. Müller, Nanostructure of healthy and caries-affected human teeth. *Nanomedicine: NBM* 2011;7:694-701, doi:10.1016/j.nano.2011.09.005

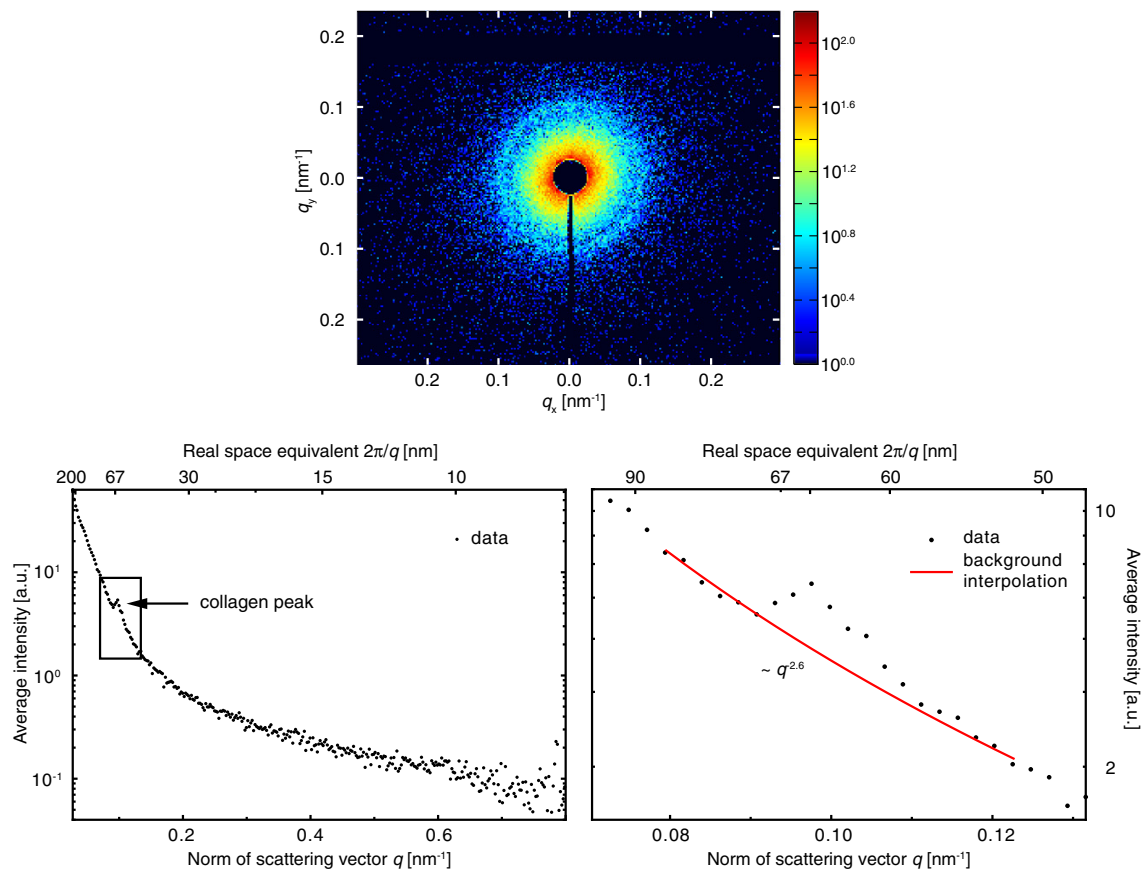


Figure 1. A typical SAXS pattern of healthy dentin with collagen ring is given on the top row. On the bottom panels, the radial-integrated intensity is shown. The collagen-associated peak can be extracted subtracting the background indicated by a solid line in the bottom right panel.

parallel to the tooth's long axis with a diamond band saw (Exakt Apparatebau GmbH, Norderstedt, Germany). The slices of the teeth were stored in phosphate-buffered saline (PBS). Only one slice from the healthy teeth was stored in air.

Synchrotron radiation-based micro computed tomography (SR μ CT) measurements were performed at the beamline W 2 (HASYLAB at DESY, Hamburg, Germany) operated by the HZG-Research Center, Geesthacht, Germany, in standard absorption contrast mode¹² in two sessions. One carious specimen was measured using a photon energy of 45 keV. The 1440 projections acquired with asymmetric rotation axis equally distributed along 360 degrees with a pixel size of 4.6 μ m were combined¹³ and binned by a factor of 2 to improve the density resolution.¹⁴ The spatial resolution of 8.8 μ m was determined from the 10% value of the modulation transfer function of a strongly x-ray absorbing edge.¹⁵ The remaining three carious specimens were also measured using a photon energy of 45 keV, but with 1800 projections over 360 degrees and a pixel size of 3.14 μ m, and a spatial resolution of

8.4 μ m. Prior to reconstruction, the data were binned by a factor of 4.

Scanning SAXS measurements were performed at the cSAXS beamline of the Swiss Light Source (PSI, Villigen, Switzerland).¹¹ The 18.58 keV photon beam was focused to $8 \times 25 \mu$ m² at the position of the specimen for the raster scans. The specimens were scanned through the beam in 50 μ m steps in x - and y -directions, perpendicular to the beam. Two modules of the PILATUS 2M detector¹⁶ positioned at 7.1 m from the specimen were used to record the scattering patterns. One carious and two healthy specimens were scanned with 20 msec exposure time per frame. The remaining specimens were measured with an exposure time of 180 msec with 24 modules of the PILATUS detector in use. Specimen-to-detector distance was determined with the first scattering order of a silver behenate calibration specimen. Prior to scattering pattern acquisition, the attenuated through-beam was recorded with the same step-size, 8 msec exposure time per point without beam stop and with attenuated beam. To reduce air scattering, an evacuated flight tube was placed between specimen and detection unit.

696

H. Deyhle et al / Nanomedicine: Nanotechnology, Biology, and Medicine 7 (2011) 694–701

Results

The organic ingredients of dentin contain mainly collagen-I fibrils. The building blocks of collagen arrange themselves along the collagen fibril with a main periodicity of 67 nm, as determined, for example, by means of atomic force microscopy and SAXS.^{17,18}

Figure 1 shows, in the top row, a typical scattering pattern from healthy dentin and the corresponding radial-integrated intensity (q -plot). A distinct peak, associated with collagen-I, is found at the q -values between 0.091 and 0.111 nm⁻¹, corresponding to a real space periodicity of 69.2 to 56.5 nm. The base intensity below the peak can be approximated with a power-law with an exponent of -2.6 (see Figure 1 diagram bottom right). The intensity above the fitted curve is solely associated with the scattering signal from the collagen.

Perfectly disc-shaped structures yield a scattering intensity, which decays according to a power-law with an exponent of -2.¹⁹ It is known that dentin contains mainly plate-like crystallites, especially near the dentin–enamel junction (DEJ).^{10,20,21} Considering the deviation of dentin crystallite shapes from perfect discs and the presence of the organic phase, the exponent of -2.6 chosen for the collagen extraction is a reasonable estimate.

Cariou infections are known to reduce the degree of calcification in tooth hard tissue. To visualize this phenomenon in quantitative fashion, two x-ray absorption measurements have been performed. Figure 2 (top) shows the logarithm of the x-ray transmission, corrected for specimen thickness, measured in line with the SAXS scan, which illustrates the expected differences between dentin and enamel. The carious lesion can be clearly identified as dark region in the center of the dentin. It is clearer in tomography data as the result of improved contrast. Therefore, a slice of the tomography data is represented in the center of Figure 2. The carious lesion appears as darker region in the center of the dentin and in the enamel due to the reduced degree of calcification. The effect is prominent and clearly detectable in the related x-ray absorption histogram given in Figure 2 below the images. Here, the carious dentin appears as shoulder and tail on the left side of the healthy dentin peak.

The images in Figure 3 (left and middle columns, top images) show the elastic scattering towards angles, which correspond to nanostructures between 56.5 and 69.2 nm for the total and the collagen-related signal, respectively. Dentin and enamel exhibit different scattering potentials and are therefore distinguishable. We found it surprising that the caries-affected regions appear brighter in enamel and dentin; i.e., they yield a stronger signal in comparison with that of the healthy tissues. This behavior can be attributed to a change in mean crystallite size of caries-affected hard tissues,²¹ or to an increased porosity in the affected dentin. The collagen-related scattering signal (bottom images), extracted from the SAXS patterns of the same tooth slice, does not allow any discrimination between healthy and caries-affected parts in the tooth, where the degree of demineralization amounts to 10%. The intensity for the enamel is close to zero because of the negligible amount of organic species in

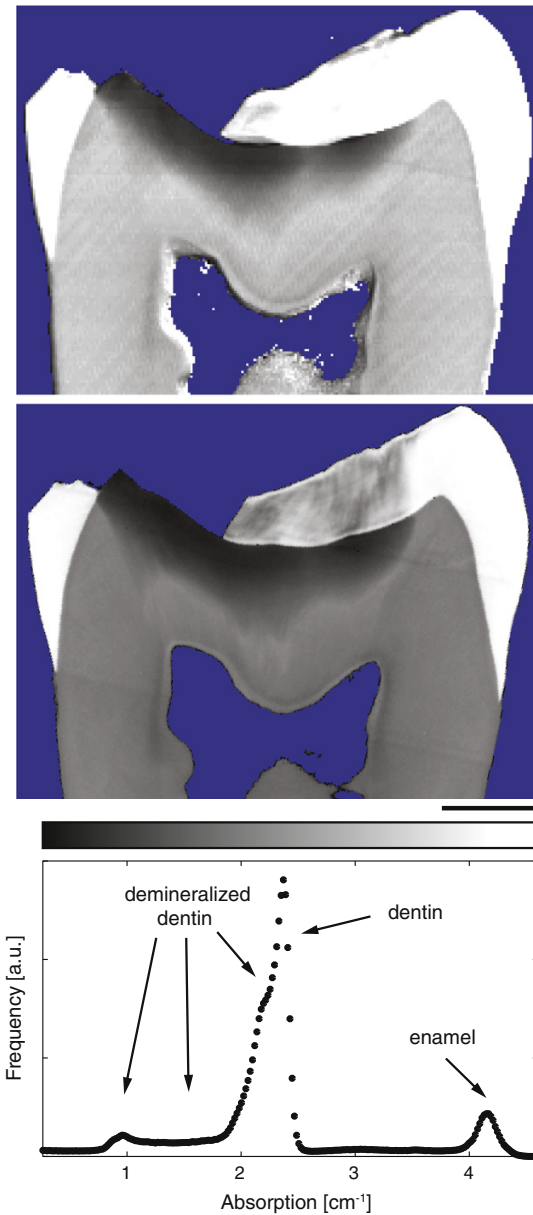


Figure 2. On top, the transmission data from the SAXS measurements of one carious specimen are presented (sam05). In the middle, a slice through the tomography data of the same specimen is shown. The carious regions are identifiable as darker regions in both enamel and dentin. The length of the bar corresponds to 2 mm. The x-ray absorption histogram of the entire tomography data is given below. The missing enamel is the result of a preparation artifact.

enamel.⁶ The dentin, however, contains anisotropic, heterogeneously distributed nanostructures as visible in both images. The scattering intensity near the dentin–enamel junction is more than a factor of two higher in comparison with the

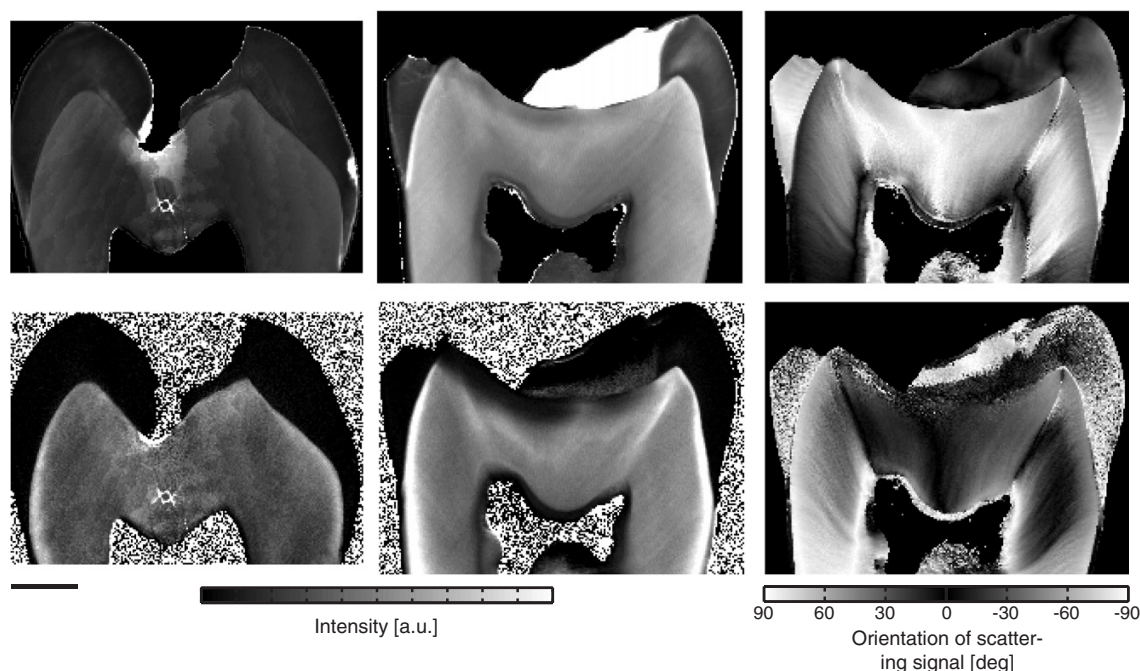


Figure 3. The first two columns of images display the elastic scattering towards angles, which correspond to nanostructures between 56.5 and 69.2 nm, for all features (top) and the collagen-related signal (bottom), respectively (sam13 and sam05). The scattered intensity is represented in average counts per pixel, corrected for specimen absorption and thickness. The caries-affected region in the dentin can be clearly identified from the integral signal, while only parts of it can be seen in the collagen-related part. The images in the right column show the preferential orientation of the nanostructures between 56.5 and 69.2 nm in sam05. The gray value labels the angle between the horizontal direction (black) and the preferential orientation of the scattering intensity. The length bar corresponds to 2 mm.

regions near pulp. This phenomenon is better illustrated in Figure 4, which includes line plots through the collagen-related signal (solid line) and the absorption (dashed line) through healthy and caries-affected regions. The collagen signal of the carious region does not differ from the one of the healthy region, if the x-ray absorption is within 70% of that of healthy tissue; i.e., the onset of collagen deterioration seems to be significantly delayed with respect to the decomposition of the mineral phase.

The analysis of the SAXS patterns does not only allow analyzing the scattering potential but also assessing the preferential orientations of nanostructures. The average direction of a scattering signal in a selected range of nanostructures (q -range) was determined approximating the azimuthal intensity distribution by a cosine.¹¹ The preferential orientation of the scattering signal caused by the tooth's nanostructures between 56.5 and 69.2 nm determined from such a fitting procedure is given in Figure 3, right column – total signal on top and collagen-related signal on bottom. The collagen-related scattering signal is oriented along collagen fibrils, whereas the scattering signal related to ceramic components is typically oriented perpendicular to structures like rods and platelets. This allows deducing the orientation of nanostructures in the tooth from the orientation of the scattering signal as shown in Figure 3. The orientation of

nanostructures changes at the dentin-enamel junction, being more or less perpendicular in the enamel and dentin at this position. In dentin one can clearly distinguish between an inner region around the pulp with vertically oriented hydroxyapatite crystallites and collagen fibers and an outer region with mainly horizontally oriented nanostructures. The carious lesion is only distinguishable in the topmost layer of the caries in the collagen orientation signal, but it is not seen in the total signal; i.e., the caries did not affect the average orientation of nanostructures. Figure 5, first and second columns, combines the information on abundance and orientation of the selected nanostructures for the total (first column) and the collagen-related (second column) scattering signals in four selected slices of three healthy teeth. The scattered intensity is coded as brightness. The color represents the preferred orientation according to the color wheel. For example, cyan marks mainly vertical scattering, red marks horizontal scattering, etc. The color saturation displays the degree of orientation, which is defined as the ratio between oriented and total mean scattered intensities.^{11,22} Enamel and dentin are clearly distinguished because of their different scattering potential and nanostructure texture. Similarities between different teeth and different positions inside one tooth concerning the organization of collagen and inorganic components can be seen (top and bottom row of Figure 5 respectively). Overall perpendicular

698

H. Deyhle et al / Nanomedicine: Nanotechnology, Biology, and Medicine 7 (2011) 694–701

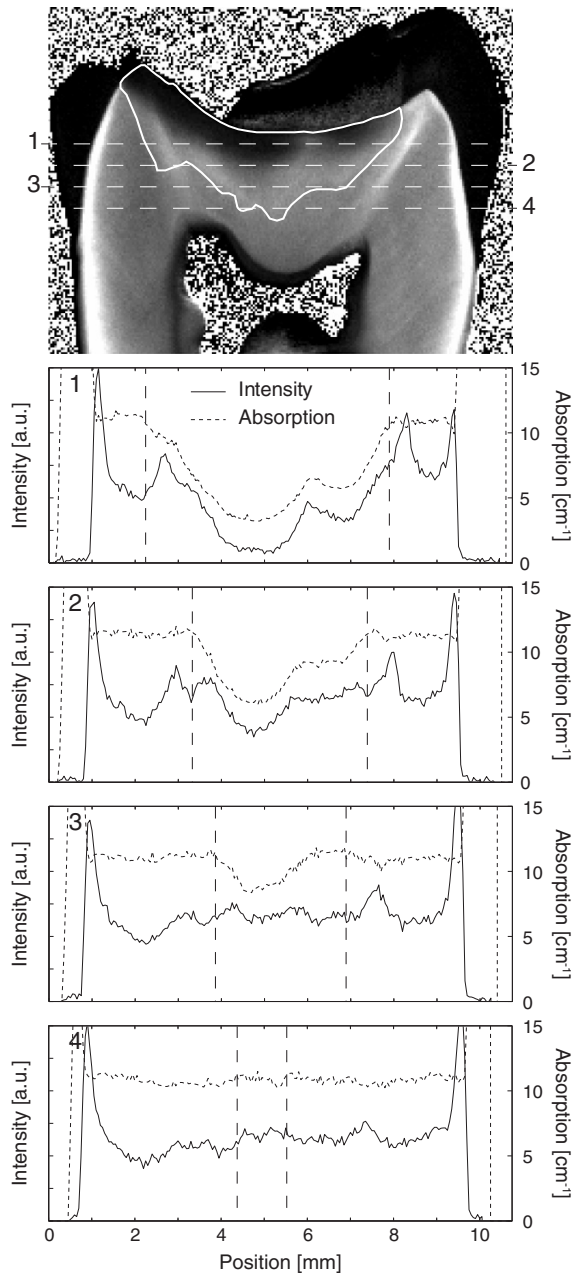


Figure 4. Intensity of the collagen-related signal across one carious tooth slice (sam05): The line plots according to the dashed lines in the image quantitatively show the changes in collagen scattering signal intensity (solid line) and specimen absorption (dotted line). The higher concentration of collagen fibrils near the dentin-enamel junction produces the prominent feature.

resp. parallel orientation of the scattering signal with respect to the dentin-enamel junction (DEJ) in dentin resp. enamel is found in all specimens. Sharp changes in nanostructure

orientation, especially in the enamel and the collagen, are present on imaginary lines connecting the tooth cusps to the pulp. Figure 5, third and fourth columns, shows these data from four slices through the carious molars. The carious regions in both dentin and enamel can be identified easily as they present stronger overall intensity in comparison with the healthy part. The overall orientation of the scattered collagen intensity is mainly perpendicular to that of the total scattering in the dentin, revealing the parallel alignment of the collagen fibrils with the inorganic crystallites, whereas no significant collagen intensity is found in the enamel. In the collagen-related signal, the carious region can be identified in the first, second, and third slice shown. However, it appears less extended than in the total scattering signal. The overall pattern in the deeper caries resembles that of healthy dentin. This implies that the caries bacteria attacks do not change the abundance and orientation of the collagen network until a certain degree of demineralization is reached.

To relate the degree of decalcification with the strength of the collagen signal, the dentin of each specimen was divided in three regions, namely sound dentin (SD), mildly carious dentin (MCD), corresponding to the tissue presenting between 90% and 70% of the x-ray absorption of healthy dentin in each specimen, and carious dentin (CD), corresponding to tissue presenting less than 70% of the x-ray absorption of the healthy part. The classification was performed through histogram analysis of the transmission data. To account for the different slice thicknesses and absorption potentials, the data were corrected by dividing the scattering signal by the slice thickness, obtained from the SR μ CT measurements, and the x-ray transmission obtained in line with the SAXS measurements.

Even though the x-ray absorption is heterogeneous in healthy dentin, this classification is an appropriate choice for intensity-based segmentation, as illustrated in Figure 6. The mean collagen signal and x-ray absorption for each region and specimen are shown in Table 1; the errors correspond to the standard deviation.

Discussion

The scanning SAXS images of human teeth show similarities to polarization microscopy pictures obtained from tooth slices many decades ago.²³ The preparation of the tooth slices for polarization microscopy, however, is much more laborious. The slices have to be thin enough for the optical transmission and their surfaces have to be well prepared to avoid artifacts. Because the photon energy can be adapted to the slice thickness in scanning SAXS, much thicker tooth slices can be investigated, reducing the potential influence of inadequate surface preparation. Another advantage of SAXS with respect to polarization microscopy is the precise quantification of abundance and orientation of nanostructures including collagen fibrils. The lateral resolution of scanning SAXS, however, is much worse than in polarization microscopy. Consequently the two methods can be regarded as complementary rather than competing.

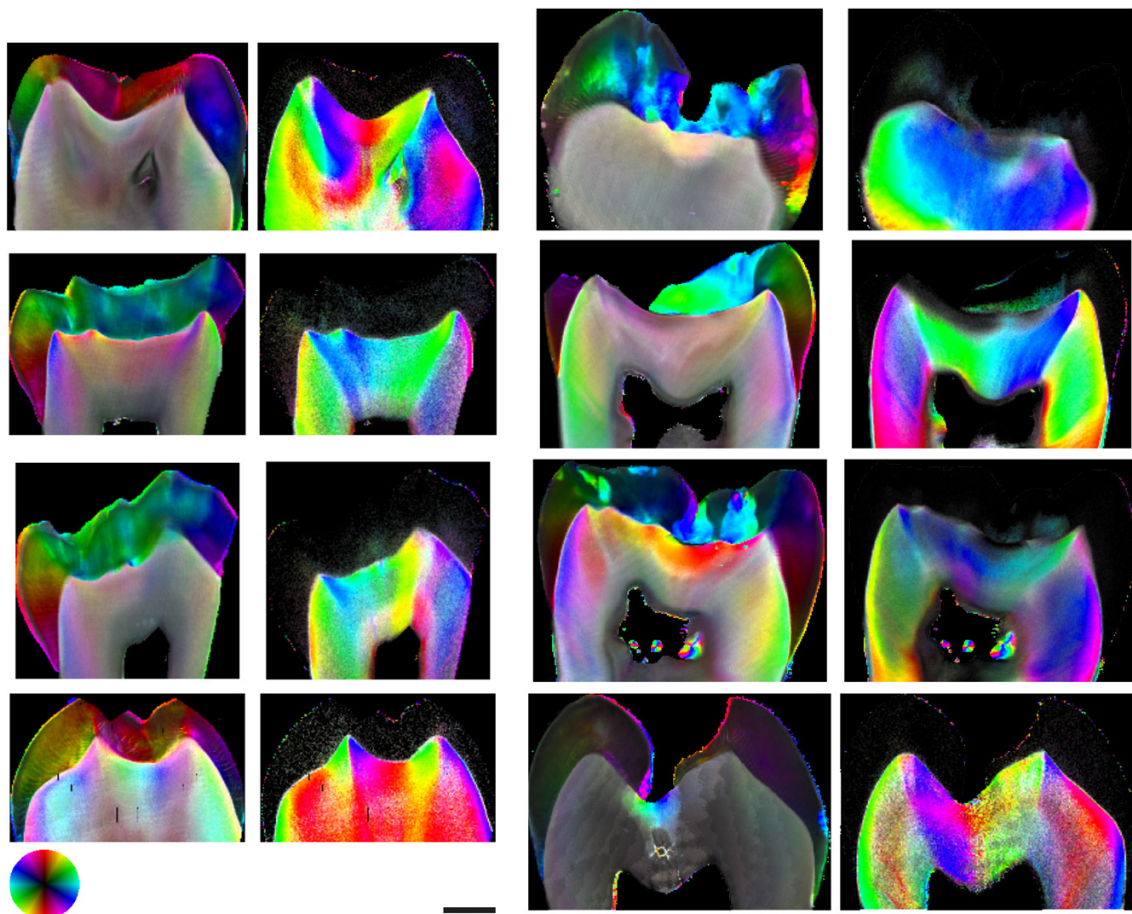


Figure 5. The color-coded images display four slices from three healthy (two left columns) and four carious (sam02, sam05, sam11, and sam13, two right columns) teeth. In the first and third columns, the total scattering signal corresponding to the range between 56.5 and 69.2 nm is given, whereas the second and fourth columns show just the collagen-related signal. The preferential orientations of the nanostructures of interest are color-coded according to the color wheel. The color intensity codes the scattered intensity, whereas the color saturation represents the degree of orientation. The length bar corresponds to 2 mm.

Caries bacteria destroy the tooth and degenerate the dentin. During the very early stages of caries, however, the nanometer-sized components are only slightly altered in size and orientation.²⁴ As opposed to local probe techniques, scattering measurements in scanning setup allow obtaining information on macroscopic specimen areas. In the range between 56.5 and 69.2 nm, the enamel exhibits a strong and anisotropic scattering signal caused by the ceramic components aligned roughly perpendicular to the dentin-enamel junction and almost perpendicular to the ceramic components within the dentin. Collagen does not exist in the enamel but exhibits within dentin a scattering signal perpendicular to the dominating calcium phosphate scatterers. The collagen is much better oriented than the inorganic stronger scatterers in the dentin. The nanostructures of the mineral phases of the enamel, however, are as well oriented as the collagen in the dentin. These observations are well in line with the well-established electron and polarization microscopy studies.^{21,23}

In carious lesions, the mineral content is significantly reduced, as shown in countless radiographs. Because of the relative high cross-section of the minerals, one would expect a correspondingly lower scattering signal within the lesion in comparison with the surrounding healthy dentin. For the range between 56.5 and 69.2 nm, however, we detected a significantly higher scattering probability. The increase of the mean crystallite size in caries-affected dentin²¹ can explain this phenomenon. Another explanation could be an increased porosity in dentinal tissue, similar to that found in enamel.²⁵ Independent of these explanations, however, we can state that this phenomenon allows identifying the carious lesion in the SAXS data, especially because the spatially resolved signals mark a clear border between carious and healthy dentin as verified by the SR μ CT data.

The collagen-related signals allow only partially differentiating between carious and healthy dentin in the affected

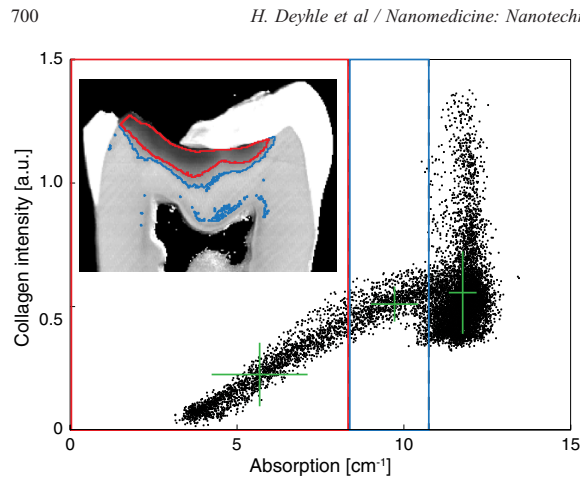


Figure 6. The plot shows the relation between collagen-related scattering signal and x-ray absorption in sam05. The blue- and red-colored regions correspond to MCD and CD. The green crosses correspond to mean values and standard deviation of each point cloud.

specimen. The presence of zones presenting different properties in carious dentin is well known and has, for example, been demonstrated by staining methods.^{7,26} More recently, Pugach et al²⁷ reported a characterization of staining-based zones with the assumption that staining relates to distinct microstructure characteristics. They distinguished between apparently normal dentin, nonstainable affected dentin, partially de-mineralized dentin (light pink staining), having a mineral content of $60\% \pm 14\%$ in comparison with healthy dentin, and a more demineralized zone (pink staining) exhibiting a mineral content of $29\% \pm 8\%$ in comparison with healthy dentin. However, characterization through staining alone may not allow differentiating remineralizable, demineralized dentin from that which can be removed only in a conventional dental treatment. The upper and lower threshold for the region termed MCD in this study were chosen based on the absorption histogram of the x-ray transmission

measured in line with SAXS, with the upper threshold corresponding to 90% of the peak position of healthy dentin lying outside this peak.

Considering the projective nature of the technique, where the demineralization front may not lie parallel to the beam direction, and thus dentin with different degrees of demineralization may overlap, the lower bound is a conservative estimate of what can still be considered mildly demineralized tissue.

The fact that half of the inspected specimens present a collagen signal in the MCD zone within 90% of the signal of sound dentin indicates that a significant amount of collagen is retained under mild demineralization, in these specimens. Five of the six remaining specimens present values between 65% and 80%, suggesting that mild to considerable damage to the collagen network has happened.

It is noteworthy that differences in the degree of preservation of the collagen occur between specimens obtained from the same tooth. Thus, not only the total degree of decalcification, but also the location within the carious lesion, seems to play a role concerning the damage to the collagen network. In addition, the projective nature of two-dimensional scanning SAXS may lead to overlapping MCD and CD zones, so that a mixed signal is obtained.

Caries bacteria destroy the tooth and degenerate the dentin, but at least during the initial stages or only mild demineralization, a significant part of the collagen network is conserved in abundance and orientation. We hypothesize that dentin with mainly healthy collagen may be suitable for remineralization.

Acknowledgments

The technical support of F. Schmidli (Basel) for the tooth preparation and of Xavier Donath during SAXS measurements is gratefully acknowledged. Extracted teeth were kindly provided by Dr. Marlen Luckow, Dr. Gabriel Krastl and Prof. Dr. Nicola Zitzmann. The SAXS experiments were performed on the cSAXS beamline at the Swiss Light Source, Paul Scherrer Institut, Villigen, Switzerland.

Table 1
Mean collagen signal intensities and x-ray absorption values of healthy and carious human teeth including their standard deviations

Specimen		Sound dentin (SD)		Mildly carious dentin (MCD)		MCD/ SD [%]	Carious dentin (CD)		CD/ SD [%]
		Collagen signal [a.u.]	Absorption [cm ⁻¹]	Collagen signal [a.u.]	Absorption [cm ⁻¹]		Collagen signal [a.u.]	Absorption [cm ⁻¹]	
28_72	sam02	0.83 ± 0.22	10.2 ± 0.4	0.41 ± 0.10	8.2 ± 0.6	49	0.28 ± 0.07	6.1 ± 0.8	34
28_72	sam03	0.60 ± 0.16	6.1 ± 0.2	0.39 ± 0.15	5.0 ± 0.4	65	0.25 ± 0.12	2.5 ± 1.4	42
48_63	sam04	0.55 ± 0.14	11.0 ± 0.4	0.54 ± 0.07	9.1 ± 0.7	98	0.27 ± 0.13	5.1 ± 1.5	49
48_63	sam05	0.56 ± 0.17	10.9 ± 0.4	0.51 ± 0.07	9.0 ± 0.7	91	0.23 ± 0.13	5.3 ± 1.3	41
48_63	sam06	0.55 ± 0.17	10.9 ± 0.4	0.53 ± 0.11	9.1 ± 0.7	96	0.18 ± 0.12	5.3 ± 1.4	33
18_66	sam07	0.65 ± 0.22	9.7 ± 0.7	0.62 ± 0.23	8.0 ± 0.5	95	0.11 ± 0.12	4.0 ± 1.6	17
18_66	sam08	0.66 ± 0.15	11.2 ± 0.4	0.44 ± 0.16	9.2 ± 0.7	67	0.10 ± 0.11	6.0 ± 1.5	15
48_66	sam09	0.60 ± 0.16	11.0 ± 0.5	0.44 ± 0.16	9.0 ± 0.7	73	0.16 ± 0.11	5.9 ± 1.8	27
48_66	sam10	0.62 ± 0.16	10.9 ± 0.4	0.46 ± 0.17	9.7 ± 0.7	74	0.14 ± 0.10	6.0 ± 1.3	23
48_66	sam11	0.63 ± 0.16	11.4 ± 0.4	0.57 ± 0.14	9.5 ± 0.6	90	0.25 ± 0.13	6.1 ± 1.8	40
48_66	sam12	0.57 ± 0.19	9.7 ± 0.6	0.52 ± 0.18	8.1 ± 0.5	91	0.47 ± 0.14	6.2 ± 0.4	82
SB3	sam13	0.21 ± 0.04	9.0 ± 0.9	0.17 ± 0.04	7.4 ± 0.5	80	0.07 ± 0.01	5.7 ± 0.1	33

The ratios relate to the collagen signal intensities. a.u., arbitrary units.

References

1. Ganss C, Schleichriemen M, Klimek J. Dental erosions in subjects living on a raw food diet. *Caries Res* 1999;33:74-80.
2. Mäkinen KK. Sugar alcohols, caries incidence, and remineralization of caries lesions: a literature review. *Int J Dent* 2010;2010:981072.
3. Ekstrand KR, Ricketts DNJ, Kidd EAM. Do occlusal carious lesions spread laterally at the enamel – dentin junction? *Clin Oral Invest* 1998(2):15-20.
4. Sunnegardh-Grönberg K, VanDijken JWV, Funegard U. Selection of dental materials and longevity of replaced restorations in Public Dental Health clinics in northern Sweden. *J Dent* 2009;37:673-8.
5. VanNieuwenhuysen JP, D'Hoore W, Carvalho J, Qvist V. Long-term evaluation of extensive restorations in permanent teeth. *J Dent* 2003;31:395-405.
6. Stack MV. The chemical nature of the organic matrix of bone, dentin, and enamel. *Ann NY Acad Sci* 1955;60:585-95.
7. Ohgushi K, Fusayama T. Electron microscopic structure of the two layers of carious dentin. *J Dent Res* 1975;54:1019-26.
8. Kurosaki N, Fusayama T. Penetration of elements from amalgam into dentin. *J Dent Res* 1973;53:309-17.
9. Bertassoni LE, Habelitz S, Pugach M, Soares PC, Marshall SJ, Marshall GW. Evaluation of surface structural and mechanical changes following remineralization of dentin. *Scanning* 2010;32:312-9.
10. Kinney JH, Pople JA, Marshall GW, Marshall SJ. Collagen orientation and crystallite size in human dentin: a small angle x-ray scattering study. *Calcif Tissue Int* 2001;69:31-7.
11. Bunk O, Bech M, Jensen TH, Feidenhans'l R, Binderup T, Menzel A, et al. Multimodal x-ray scatter imaging. *New J Phys* 2009;11:123016.
12. Beckmann F, Herzen J, Haibel A, Müller B, Schreyer A. High density resolution in synchrotron-radiation-based attenuation-contrast microtomography. *Proc SPIE* 2008;7078:70781D.
13. Müller B, Bernhardt R, Weitkamp T, Beckmann F, Bräuer R, Schurig U, et al. Morphology of bony tissues and implants uncovered by high-resolution tomographic imaging. *Int J Mater Res* 2007;98:613-21.
14. Thurner P, Beckmann F, Müller B. An optimization procedure for spatial and density resolution in hard x-ray micro-computed tomography. *Nucl Instrum Meth B* 2004;225:599-603.
15. Müller B, Thurner P, Beckmann F, Weitkamp T, Rau C, Bernhardt R, et al. Three-dimensional evaluation of biocompatible materials by microtomography using synchrotron radiation. *Proc SPIE* 2002;4503:17888.
16. Kraft P, Bergamaschi A, Broennimann C, Dinapoli R, Eikenberry EF, Henrich B, et al. Performance of single-photon-counting PILATUS detector modules. *J Synchrotron Radiat* 2009;16:368-75.
17. Balooch M, Habelitz S, Kinney JH, Marshall SJ, Marshall GW. Mechanical properties of mineralized collagen fibrils as influenced by demineralization. *J Struct Biol* 2008;162:404-10.
18. Habelitz S, Balooch M, Marshall SJ, Balooch G, Marshall GW. In situ atomic force microscopy of partially demineralized human dentin collagen fibrils. *J Struct Biol* 2002;138:227-36.
19. Guinier A, Fournet G. Small angle scattering of x-rays. New York: John Wiley & Sons, Inc.; 1955.
20. Johansen E, Parks HF. Electron microscopic observations on the three-dimensional morphology of apatite crystallites of human dentine and bone. *J Biophys Biochem Cytology* 1960;7(4):743-6.
21. Takuma S, Tohda H, Watanabe K. Size increase of dentin crystals in the intertubular matrix due to caries. *J Electron Microsc* 1986;35:60-5.
22. Müller B, Deyhle H, Bradley D, Farquharson M, Schulz G, Müller-Gerbl M, et al. Scanning x-ray scattering: Evaluating the nanostructure of human tissues. *Eur J Nanomed* 2010;3:30-3.
23. Schmidt WJ, Keil A. Die gesunden und die erkrankten Zahngewebe des Menschen und der Wirbeltiere im Polarisationsmikroskop. Theorie, Methodik, Ergebnisse der optischen Strukturanalyse der Zahnhartsubstanzen samt ihrer Umgebung. Carl Hanser Verlag: Munich; 1958.
24. Märten A, Fratzl P, Paris O, Zaslansky P. On the mineral in collagen of human crown dentine. *Biomater* 2010;31:5479-90.
25. Robinson C, Shore RC, Brookes SJ, Strafford S, Wood SR, Kirkham J. The chemistry of dental enamel. *Crit Rev Oral Biol Med* 2000;11:481-95.
26. Fusayama T, Terachima S. Differentiation of two layers of carious dentin by staining. *J Dent Res* 1972;51:866.
27. Pugach MK, Strother J, Darling CL, Fried D, Gansky SA, Marshall SJ, et al. Dentin caries zones: mineral, structure, and properties. *J Dent Res* 2009;88:71-6.

2.4 Morphology of carious enamel

The moderate enamel caries exhibits a complex structure of alternating layers exhibiting varying scattering potential and degree of mineralization. Nonetheless, the orientation of the crystallite is preserved throughout the lesions.

Published in Acta Biomaterialia



Contents lists available at ScienceDirect

Acta Biomaterialia

journal homepage: www.elsevier.com/locate/actabiomat

Nanostructure of carious tooth enamel lesion



Hans Deyhle^{a,b}, Shane N. White^c, Oliver Bunk^b, Felix Beckmann^d, Bert Müller^{a,*}

^a Biomaterials Science Center, University of Basel, c/o University Hospital, 4031 Basel, Switzerland

^b Swiss Light Source, Paul Scherrer Institut, 5232 Villigen, Switzerland

^c UCLA School of Dentistry, University of California, Los Angeles, CA 90095-1668, USA

^d Institute of Materials Research, Helmholtz-Zentrum Geesthacht, 21502 Geesthacht, Germany

ARTICLE INFO

Article history:

Received 22 April 2013

Received in revised form 6 July 2013

Accepted 13 August 2013

Available online 28 August 2013

Keywords:

Enamel nanostructure

Smooth surface caries

Small-angle X-ray scattering

Human tooth

Synchrotron radiation

ABSTRACT

Carious lesions exhibit a complex structural organization composed of zones of higher and lower mineralization, formed by successive periods of cyclic de- and re-mineralization. A thorough understanding of the lesion morphology is necessary for the development of suitable treatments aiming to repair rather than replace the damaged tissue. This detailed understanding includes the entire lesion down to individual crystallites and nanopores within the natural organization of the crown. A moderate lesion, with surface loss and reaching dentin, and a very early lesion were studied. Scanning small-angle X-ray scattering (SAXS) with a pixel size of $20 \times 20 \mu\text{m}^2$ was used to characterize these lesions, allowing for the identification of distinct zones with varied absorption and scattering behavior, indicative of varied porosity and pore morphology. Despite these differences, the overall orientation and anisotropy of the SAXS signal was unaltered throughout both lesions, indicating that an anisotropic scaffold is still present in the lesion. The finding that crystallite orientation is preserved throughout the lesions facilitates the identification of preventive re-mineralizing strategies with the potential to recreate the original nanostructure.

© 2013 Acta Materialia Inc. Published by Elsevier Ltd. All rights reserved.

1. Introduction

Caries is the most prevalent of all chronic childhood diseases and the leading cause of tooth loss among young adults in many societies [1–3]. Caries causes considerable suffering, loss of function and the need for costly restorative, endodontic and prosthetic interventions. However, behavioral, dietary, preventive and interventional actions can re-mineralize early lesions [4–6]. Improved knowledge of the carious process, de- and re-mineralization, at the component or nano-structural level could facilitate improved preventive and therapeutic approaches for early lesions and allow moderate lesions to be addressed.

Caries is a chronic hard tissue infection [7]. Smooth surface caries has been studied extensively, not just because of its epidemiological importance, but also because a relatively simple geometry facilitates studies and experimental modeling. Lesions have been studied in many ways, including macroscopic examination, hard tissue histology, light microscopy, scanning and transmitted electron microscopy, microradiography, micro and nano indentation, histochemical, microbiological and chemical analyses, and X-ray imaging techniques [8–19]. These methods have provided a wealth of information and allowed various zones to be identified. Electron microscopy has been used to observe microstructural changes such as clefs or channels in incipient lesions and to identify de- and

re-mineralization-induced changes to individual crystallites, but generally only after they have been removed from their original spatial organizational positions and associations with their neighbors. Detailed understanding, or mapping, of the entire lesion at the level of individual crystallites and porosities remains elusive.

Differences in optical birefringence caused by the submicroscopic pores produced during de-mineralization have been used to divide the smooth surface lesion into four zones [15,20,21]: first, an outer surface layer of intact relatively unaffected enamel, displaying negative birefringence to polarized light, radio-opacity, with some focal holes and ~10% mineral loss; second, the body of the lesion, with positive birefringence to polarized light, radiolucency and substantial mineral loss of ~24%; third, the dark zone, with positive birefringence to polarized light, radio-opacity and ~6% of mineral loss; finally, the translucent zone with negative birefringence to polarized light, radio-opacity and only ~1% mineral loss. However, this classification does not describe changes in crystallite structure or organization. Furthermore, smaller and deeper pores are not discerned by birefringence [22].

Small-angle X-ray scattering (SAXS) is capable of delivering structural information about macromolecules or crystallites and of repeat distances in partially ordered systems as small as a few nanometers in size and up to several hundred nanometers [23–33]. This range is well suited to studying hydroxyapatite crystallite and collagen periodicities, the primary components of tooth structure. The combination of SAXS with real-space scanning [34] allows for the investigation of a tooth's nano-structural

* Corresponding author. Tel.: +41 (0) 61 265 9660; fax: +41 (0) 61 265 9699.
E-mail address: bert.mueller@unibas.ch (B. Müller).

components over extended areas through the acquisition of thousands scattering patterns [23,29–31,35,36]. Two-dimensional (2-D) maps with raster-scan step sizes as small as $0.1 \times 0.1 \text{ mm}^2$ have been made [31]. Because an early carious lesion may be only 0.1–0.2 mm in total thickness, and because features within a moderate lesion may be <0.1 mm thick, increased point density is needed to study the four zones generally used to describe smooth surface caries. Scanning SAXS with raster-scan step sizes of $20 \times 20 \text{ }\mu\text{m}^2$ is applied. This high point density allows the identification and comparison of morphological differences within and among carious zones with respect to structural organization: orientation and degree of anisotropy of the nanometer-size components.

2. Materials and methods

2.1. Carious specimens

Two representative naturally occurring smooth surface carious lesions, moderate and early, obtained from two third molars extracted for clinical reasons, were studied. All procedures were conducted in accordance with the Declaration of Helsinki and according to the ethical guidelines of the Canton of Basel, Switzerland. Teeth were extracted for clinical reasons unrelated to the study. Written consent by the patients concerning use of the extracted teeth is given in the patient entry form of the dental school. The consent is not study specific. Teeth are anonymized. Backtracking of patient identity is impossible and not desired. The moderate lesion (specimen H) had slight surface loss and appeared to barely reach beyond the dentino-enamel junction (DEJ). The early lesion (specimen V) was smaller and incipient, without surface breakdown, and limited to the outer third of the enamel. The tooth slices were cut using a diamond band saw (Exakt Apparatebau GmbH, Norderstedt, Germany). A $200 \text{ }\mu\text{m}$ thin slice was cut in a transverse direction through the moderate lesion, while a $200 \text{ }\mu\text{m}$ thin slice was obtained through the early lesion in the buccal-lingual direction (see Fig. 1). The slices were stored in phosphate buffered saline before and during measurements.

2.2. Conventional micro computed tomography

Micro computed tomography (μCT) data sets of the entire teeth were acquired with a Skyscan 1174™ tabletop scanner (Bruker, Belgium), and 900 projections with a pixel size of $35.6 \text{ }\mu\text{m}$ were acquired over 360° . The acceleration voltage was set to 50 kV and the beam current to $800 \text{ }\mu\text{A}$. The data were reconstructed using a modified Feldkamp algorithm (NRecon, Bruker, Belgium).

2.3. Synchrotron radiation-based μCT

Synchrotron radiation-based μCT (SR μCT) measurements were performed at the W2 beamline at HASYLAB (DESY, Hamburg, Germany) operated by the HZG research center [37]. For specimen V, the photon energy was set to 45 keV, and 1440 equiangular projections with a pixel size of $4.6 \text{ }\mu\text{m}$ were acquired over 360° . The rotation axis was chosen asymmetrical to the incoming X-ray beam to allow for a larger field of view [38]. The data were reconstructed using a filtered backprojection algorithm. Specimen H was measured at a photon energy of 30 keV. The pixel size of the projections corresponded to $3.2 \text{ }\mu\text{m}$, and 900 projections were acquired over 180° .

2.4. SAXS data acquisition

Scanning SAXS measurements were performed at the cSAXS beamline [39] of the Swiss Light Source (Paul Scherrer Institute, Villigen, Switzerland). The specimens were stored in polyimide sa-

chets and placed on an aluminum holder. Scattering patterns were acquired in a raster scan fashion in the x - and y -directions perpendicular to the beam. For specimen V, the points at which SAXS data was acquired were $50 \text{ }\mu\text{m}$ apart in both x - and y -directions, while for specimen H, a raster scan step size of $20 \text{ }\mu\text{m}$ was chosen. The photon energy was set to 18.6 keV. The scanning in the horizontal, i.e., x -, direction was performed with the detector recording a series of SAXS data, while the specimens moved at a velocity of 1.786 and 0.714 mm s^{-1} , respectively. The X-ray beam was focused to $25 \text{ }\mu\text{m} \times 8 \text{ }\mu\text{m}$ full width at half-maximum (FWHM) spot size at the specimen position. In the first scan, the X-ray transmission of the specimens at each scanning position was recorded with no beam stop and an attenuated beam with 8 ms exposure time. In the second scan, the scattering patterns were recorded with two modules of the PILATUS 2 M detector [40] with 20 ms exposure time and 8 ms readout time. For specimen V, 32,000 frames were acquired, and for specimen H, 82,000 frames. The direct beam was covered with a beam stop 3 mm in diameter. The transmission data were used to correct the SAXS signal for specimen absorption. The specimen-detector distance of 7140 mm was determined with the first-order diffraction ring of a silver-behenate powder. To minimize air scattering, an evacuated flight tube was placed between specimen and detector.

2.5. SAXS data treatment

Each scattering pattern is divided into 16 azimuthal sectors, and the intensity is azimuthally integrated at each radial position, yielding, for each scattering pattern, intensities for the 16 segments as a function of q . The intensity in each segment for a chosen radial range, plotted against the segment angular position ϕ , is approximated with a cosine by means of fast Fourier transform:

$$I(\phi) = I_0 + I_2 \cos(\phi + \Phi) \quad (1)$$

where I_0 and I_2 are the norm of the zero and second Fourier components, respectively, and Φ is the phase of the second Fourier component. The data treatment is explained in detail elsewhere [39]. The data were treated using self-written MATLAB® (2011, The MathWorks, Natick, USA) routines.

The SAXS signal along radial lines through the carious lesions was plotted from 0° to 45° in the direction of maximum extension of the lesion in 15° increments. Control plots of sound tooth structure were made along radial lines of the same specimen, but because natural caries was studied, the control plots could not be made at the same site as the caries. Therefore, the control samples inevitably differed slightly from the carious samples with respect to enamel and dentin thickness and radius of curvature. Additionally, because the moderate caries specimen had lost some surface enamel, its outer endpoint, did not coincide with that of the intact controls. The following data fields were examined and plotted for sound control samples and for samples through the moderate and incipient carious lesions. The mean orientation of the scattering signal can be extracted from the phase term Φ given in Eq. (3). The orientation of the scattering signal is generally perpendicular to the main orientation of the scattering structures, e.g., crystallites in dentin and enamel.

3. Results

The SAXS study includes results from two representative examples of the carious process: a moderate lesion with surface loss reaching dentin with a horizontal orientation (specimen H); and an early surface lesion with a vertical orientation (V). Both examples are smooth surface lesions. Control samples were taken from healthy unaffected enamel in the same tooth specimens.

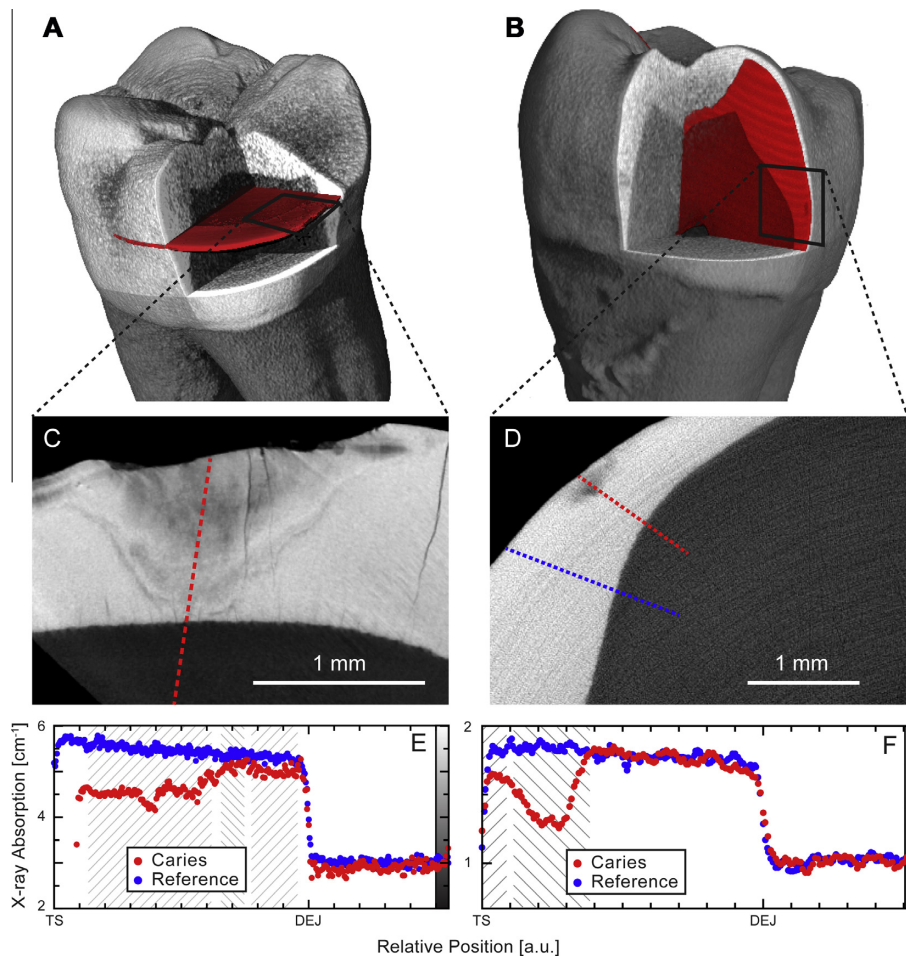


Fig. 1. (A, B) Position of specimens H and V in a 3-D μ CT rendering of the teeth. (C, D) Selected virtual cuts through the SR μ CT data of the tooth slices. The carious lesion in specimen H (C) can be identified as darker region in the enamel, extending from the TS to the dentin. The funnel-shaped subsurface lesion in specimen V (D) appears as darker spot near the outer limit of the enamel. (E, F) Line plots of X-ray absorption through the specimens according to the dashed lines in (B) and (C), respectively. The line through unaffected enamel in specimen H (C) lies outside the field of view. The abscissa was rescaled so that both the DEJ and TS were superimposed.

3.1. Moderate lesion reaching dentin, specimen H

Fig. 1 shows the position of specimens H and V within the corresponding teeth, in a three-dimensional (3-D) μ CT rendering. Specimen H presented a moderate lesion extending to the dentin, as visible in the SR μ CT slice (Fig. 1C). The outermost surface enamel (zone 1) was intact at the peripheral borders of the lesion, but was absent from the central part of the lesion, probably as a result of the carious process. Within the remaining carious lesion, three additional zones were discerned; these were described by a profile of X-ray absorption through the center of the lesion (Fig. 1E). Zone 2 extended through half the thickness of the enamel and exhibited the lowest X-ray density, with a mean absorption corresponding to 86% of that of comparable unaffected enamel, and minima of 76%. Zone 3, a narrower band, deeper than and surrounding the first zone, showed X-ray absorption comparable with that of unaffected enamel, especially towards the sides of the lesion. Finally, zone 4, adjacent to the second and reaching the dentin, again displayed slightly decreased absorption with respect to unaffected enamel, with a mean of 93% and minima of 88%. Bands of alternating

X-ray absorption could be seen in the deeper parts of the lesions on both sides of its deepest extension.

The total scattered intensity is described in Fig. 2. Fig. 2A–C shows the intensity of the scattering signal on a line through the lesion (red dots) and one through unaffected enamel (blue dots), in the q ranges corresponding to 10–20 nm, 100–110 nm and 190–200 nm, respectively. The momentum transfer q is defined as $q = \frac{4\pi}{\lambda} \sin(\theta)$, where λ is the wavelength of the scattering X-rays, and θ is the half scattering angle. q is related to the real space periodicity d by $q = \frac{2\pi}{d}$. Fig. 2D shows three profiles through unaffected enamel at different positions in the specimen (cf., image bottom right) in the range 100–110 nm. The abscissae of the plots were rescaled so that both the DEJ and tooth surface (TS) were superimposed. Little difference in scattered intensity plots could be discerned among the unaffected control samples.

Within the moderate carious lesion, distinct scattering intensity zones were discerned; they were largely coincident with the absorption zones, and are indicated by the shaded regions in Fig. 2A–C. Zone 2 exhibited high scattering in the body of the lesion, extending through half the enamel thickness; zone 3 was

358

H. Deyhle et al./Acta Biomaterialia 10 (2014) 355–364

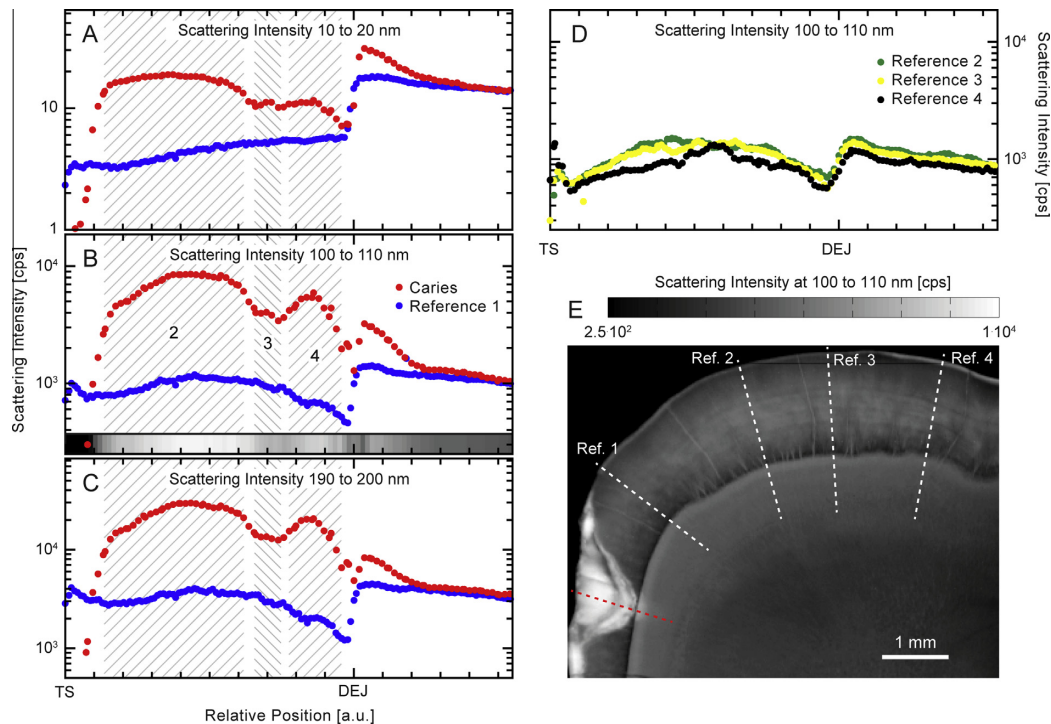


Fig. 2. (A–C) Intensity of the scattering signal on a line through the lesion (red dots) and one through unaffected enamel (blue dots), in the ranges 10–20 nm, 100–110 nm and 190–200 nm, of specimen H, in counts per second according to the dashed lines in (E). Distinct scattering intensity zones can be discerned within the lesion, indicated by the shaded regions. (D) Three line plots through unaffected enamel at different positions in the specimen in the range 100–110 nm to demonstrate their similarity. (E) 2-D map of the total scattering intensity at scattering angles corresponding to the range 100–110 nm.

an intermediate band with reduced scattering; and zone 4 a region with increased scattering, approached the DEJ. Scattering intensities from zones 3 and 4 became more and more alike for smaller features in the 10–20 nm range. No such zones were found in unaffected healthy enamel over the ranges examined (Fig. 2A–D). The total scattered intensity of sound unaffected bulk enamel was almost an order of magnitude lower than the peak signal at the center of the body of the carious lesion. Table 1 summarizes the optical and X-ray scattering behavior of each zone.

As for all the plots in the present paper, additional data sets were created along lines rotated $\pm 15^\circ$ from the central lines through the maximum extensions of the lesions depicted in Figs. 2 and 4–6 (data not shown). Little difference was found between these additional lines and the central lines; angled lines simply produced more oblique images of the same features.

In the narrow region of the DEJ interface, the plots of carious and unaffected control samples intersected (Fig. 2A–C). However, increased scattering intensity was found in the affected region of dentin immediately beneath the DEJ (Fig. 2A–C).

Scattered intensities for points belonging to the three carious zones (I_{car}) and points from anatomically similar regions in healthy enamel (I_{sound}) are compared in Fig. 3A. The ratio I_{car}/I_{sound} is plotted as a function of momentum transfer q . Zones 1 and 2 presented similar behavior, the ratio I_{car}/I_{sound} being constant over all but the smallest examined q ranges corresponding to periodicities <50 nm. For zone 2, I_{car}/I_{sound} amounted to about two-thirds of I_{car}/I_{sound} of zone 1. Zones 2 and 4 behaved in a like manner at periodicity ranges >100 nm. For smaller periodicities, the intensity in zone 4 decreased more rapidly than in zones 2 and 3.

The mean orientation of scattering patterns [39] is displayed in Fig. 4. The color in the image (Fig. 4E) shows the orientation of the

Table 1
Classification of carious zones comparing optical and X-ray scattering behavior.

Zone	Pore size/distribution	Birefringence ([15,20,21])	X-ray absorption (with respect to unaffected enamel)	Scattering potential (with respect to unaffected enamel)
Zone 1	intact enamel ^a	Negative	Approximating unaffected enamel [†]	Approximating unaffected enamel [†]
Zone 2	Homogeneous pore size distribution between 50 and 200 nm	Positive	Reduced (~75% of unaffected enamel)	Over one order of magnitude higher
Zone 3	Homogeneous pore size distribution between 50 and 200 nm	Positive	Approximating unaffected enamel	About five times higher
Zone 4	Prevalence of larger pores (here above 100 nm)	Negative	Slightly reduced (~93% of unaffected enamel), with bands approximating unaffected enamel	Over one order of magnitude higher

^a The statements concern specimen V.

main scattering signal for each point according to the color wheel. The line plots show the orientation of the scattering signal with respect to the dashed lines indicated in Fig. 4E, with 0° indicating a

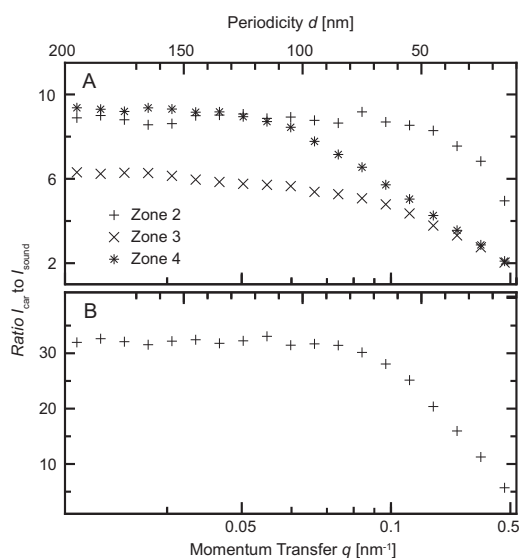


Fig. 3. (A) Ratio $I_{\text{car}}/I_{\text{sound}}$ of the scattering signal of a representative point in each carious zone I_{car} to a comparable point in healthy unaffected enamel I_{sound} as a function of the feature size d for specimen H. (B) Ratio $I_{\text{car}}/I_{\text{sound}}$ for one point inside the lesion and a corresponding point in healthy unaffected enamel of specimen V as a function of momentum transfer q .

parallel alignment. Fig. 4A–C shows the orientation of the scattering signal in the ranges 10–20 nm, 100–110 nm and 190–200 nm, respectively, along a line through the lesion. A plot through unaffected healthy enamel, showing the orientation of the scattering signal related to features between 100 and 110 nm, is shown in Fig. 4D. The abscissae of the plots were rescaled so that both the DEJ and TS were superimposed. Carious enamel samples and their sound unaffected controls exhibited remarkably little difference in their values over the range of periodicities studied.

Fig. 5D shows the azimuthal plot around the direct beam of the total scattered intensity in a radial range corresponding to 100–110 nm, for a point in the caries (red dots) and in unaffected enamel (blue dots). The SAXS intensity is localized mainly along the equatorial direction of the crystallites (i.e., parallel to the TS) in both carious and unaffected enamel, giving rise to two distinct peaks. The increased intensity of the scattering signal from carious enamel is almost solely associated with the direction perpendicular to the crystallites, whereas the increase in intensity observed in all other directions was an order of magnitude smaller. The width of the peaks is related to the anisotropy of the scattering features within the specimen. For each raster scan point, the peaks were fitted with Gaussians and a constant background, and the FWHM was extracted. Fig. 5E shows the FWHM for each point in the range corresponding to 100–110 nm. In zone 2, slight changes to the FWHM of the equatorial scattering can be identified. The red and blue dots indicate the points from which the azimuthal intensity distribution in Fig. 5A was plotted. Fig. 5A–C shows the FWHM of the equatorial peaks in the ranges 10–20 nm, 100–110 nm and 190–200 nm, respectively, along a line through the lesion (red dots) and a line through unaffected enamel (blue dots). A slight decrease in the FWHM, i.e., an increase in SAXS anisotropy, can be found in the carious region, especially towards larger nanometer periodicities.

3.2. Early surface enamel lesion, specimen V

The orientation of the section of interest within the tooth is displayed in Fig. 1B. Selected slices through the SR μ CT data set of

specimen V are shown in Fig. 1D. The carious lesion was visible as a small darker region in the sub-surface enamel owing to reduced X-ray absorption. No surface loss was evident. Line plots showed that the absorption of the outermost surface of the lesion, zone 1, approximated that of unaffected controls; the body of the lesion, zone 2, exhibited a definite subsurface dip in X-ray absorption (Fig. 1F). In all other ways, X-ray absorption did not differ among control and lesion plots.

Total scattered intensity is described in Fig. 6A for the range 100–110 nm, along a line through the lesion (red dots) and through unaffected enamel (blue dots). Plots for the other examined ranges exhibited equivalent behavior (data not shown). The small early carious lesion differed from the moderate carious lesion. The very outermost surface enamel, zone 1, indicated by the shaded region labeled 1, approximated the control samples, and a single narrow sharp spike in scattered intensity, the body of the lesion, was localized to the outer half of the enamel thickness, indicated by the shaded region labeled 2.

Fig. 3B, shows the ratio $I_{\text{car}}/I_{\text{sound}}$ for a point inside the small lesion and a comparable point in healthy enamel, analogously to the three regions of the moderate lesion. The ratio keeps a constant value for periodicities down to 100 nm, and decreases towards larger scattering angles, analogous behavior to zone 2 in the moderate lesion.

The angle of scattering signals in the range 100–110 nm with respect to a radial line is displayed in Fig. 6C (through the carious lesion) and D (through healthy unaffected tissue). Little difference could be discerned between values from the carious region and their controls. These data are shown in separate plots for the sake of clarity. Plots for the other examined ranges exhibited equivalent behavior (data not shown). Anisotropy, as extracted from the FWHM of the equatorial scattering (cf., Fig. 5), is shown in Fig. 6B, along a line through the lesion (red dots), and one through unaffected enamel (blue dots). The FWHM for each raster scan point in the range 100–110 nm is shown in Fig. 6F. The carious lesion is visible as slightly darker zone near the TS.

4. Discussion

4.1. Zone classification

Absorption data were consistent with prior radiographic analyses. The small early lesion had a narrow dip in absorption that was sharply localized to a zone just beneath the relatively normal outermost enamel. These results suggest that, in these real-life carious lesions, the outermost enamel can readily re-mineralize, or even hyper-mineralize in an appropriate environment [7]. Many prior studies profiling carious lesions have shown increased X-ray density, increased mineralization, micro- and nano-hardness of zone 1 surface enamel [9,10,12–14,16,41–43]. Physicochemical phenomena and protection by saliva seem the most likely reasons for the fortification of the outermost enamel [7,44]. Although surface protection does not occur in all cases, it has been reported in both naturally occurring and artificial lesions [9,10,12–14,16,41–44]. However, re- or hyper-mineralization of the outermost enamel is a double-edged sword: it prevents substrates, calcium and phosphate ions, reaching the deeper parts of the lesion, thus preventing re-mineralization of deeper parts of the lesion. The moderate lesion demonstrated the additional complexity of the bulk and deepest parts of the enamel lesion being separated by an intermediate denser and thus less porous zone and containing several alternating layers or laminations, displayed as layers of alternating X-ray density (Fig. 1) [45]. The laminations may have been produced by successive periods of cyclic de- and re-mineralization over differing time periods when the environment may have favored one or other process [45].

360

H. Deyhle et al./Acta Biomaterialia 10 (2014) 355–364

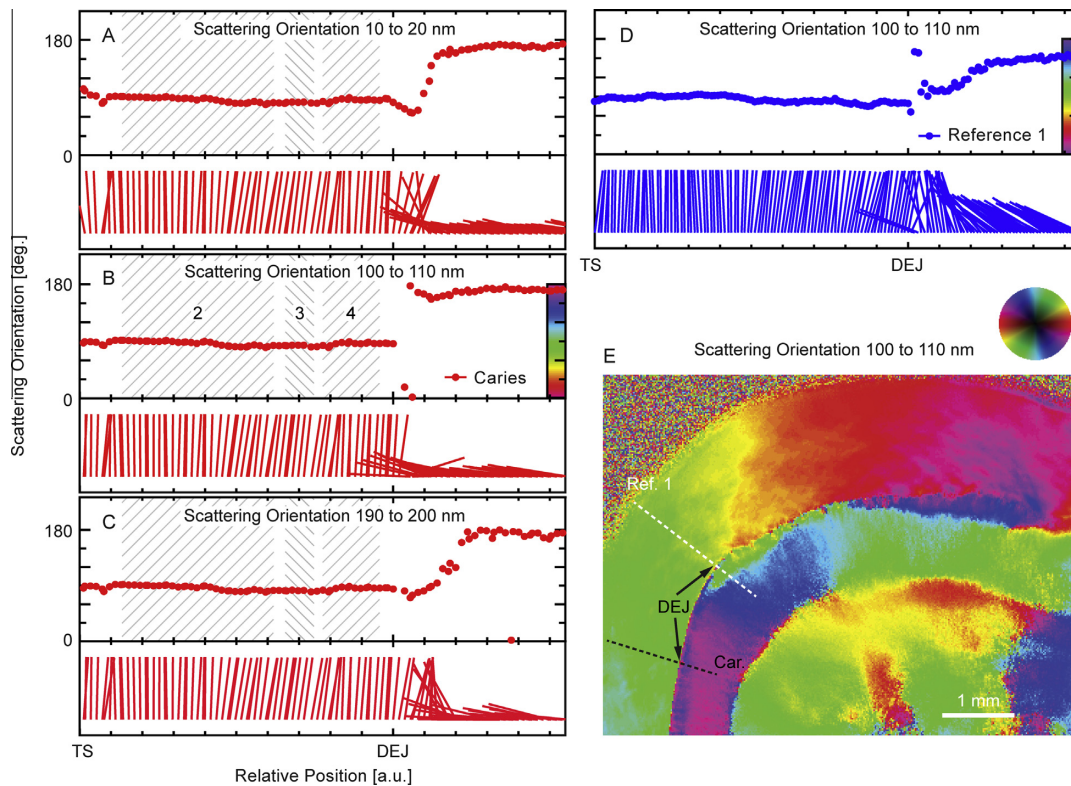


Fig. 4. (A–C) Orientation of the scattering signal along the black dashed line indicated in the image (E). The values given correspond to the angle between the main orientation of the scattering signal and the black dashed radial line, with 0° indicating a parallel alignment. Plots (A–C) show the orientation of the scattering signal in the ranges 10–20 nm, 100–110 nm and 190–200 nm, respectively. The vector plots demonstrate the perpendicular alignment of the scattering signal to the radial line in enamel. The shaded regions correspond to the zones as identified in Fig. 2. (D) Orientation of the scattering signal along a line through unaffected healthy enamel, in the range 100–110 nm, cf., white dashed line in (E). (E) 2-D map of the orientation of the scattering signal at scattering angles corresponding to the range 100–110 nm, according to the color wheel.

Differences in birefringence due to the production of submicroscopic pores during de-mineralization have been used to segment the smooth surface carious enamel lesion into four zones: the outer surface (zone 1), the body of the lesion (zone 2), the dark zone (zone 3), and the translucent zone (zone 4) [15,20,21]. Most of the outermost enamel surface of the moderate lesion, zone 1, had been lost and thus was not studied. However, the remaining lesion was divisible by absorption and scattering intensity into zones broadly coincident with those defined by differences in optical birefringence [15,20,21]. In the small early lesion, zones 1 and 2 were evident and broadly coincident with those defined by differences in optical birefringence.

Since both methods are sensitive to the presence of pores within the calcium phosphate phases of the enamel, the assumption that the zones coincide is reasonable. As optical birefringence, related to the wavelength of visible light, it is relatively sensitive to long-range orders in comparison with SAXS, the methods are complementary.

4.2. Pore size distribution

The increase in the abundance of pores in carious tooth structures must be considered to be a primary defining feature of the carious process. Accordingly, an increased scattered intensity in carious dentin [31] and enamel [35] has been reported. Since the

SAXS signal intensity is not homogeneous across the thickness of the enamel, the ratio $I_{\text{car}}/I_{\text{sound}}$ of the SAXS signal from the carious lesion and from an anatomically equivalent region was chosen to illustrate changes in scattering behavior.

In zone 4 of the moderate lesion, generally consistent with the translucent zone, $I_{\text{car}}/I_{\text{sound}}$ decreased markedly <100 nm, indicative of larger pores. The fact that the $I_{\text{car}}/I_{\text{sound}}$ was constant for all investigated nanometer ranges except the smallest ones <50 nm in both zones 2 and 3 suggests the presence of a more homogeneous distribution of pore sizes in the investigated range 200–50 nm.

It has been hypothesized that, in the outer regions of surface caries and, notably, in the dark zone (zone 3), some degree of remineralization occurs [46], or that the redistribution of endogenous organic material inside the lesion leads to increased mineral content [47]. This similar behavior of the ratio $I_{\text{car}}/I_{\text{sound}}$ as a function of scattering angle in zones 2 and 3 is indicative of a similar caries-induced destruction pattern, consisting of larger and smaller pores, where the smaller ones are the result of partially remineralized larger voids [45,48]. The higher scattered intensity in zone 1 arises from a more advanced status of enamel deterioration, i.e., a higher density of pores, in agreement with its reduced X-ray density. The decreased number of pores in zone 2 is partly due to natural re-mineralization.

The findings represented in Figs. 1–6 are consistent with the traditional models of the carious lesion derived from light microscopy,

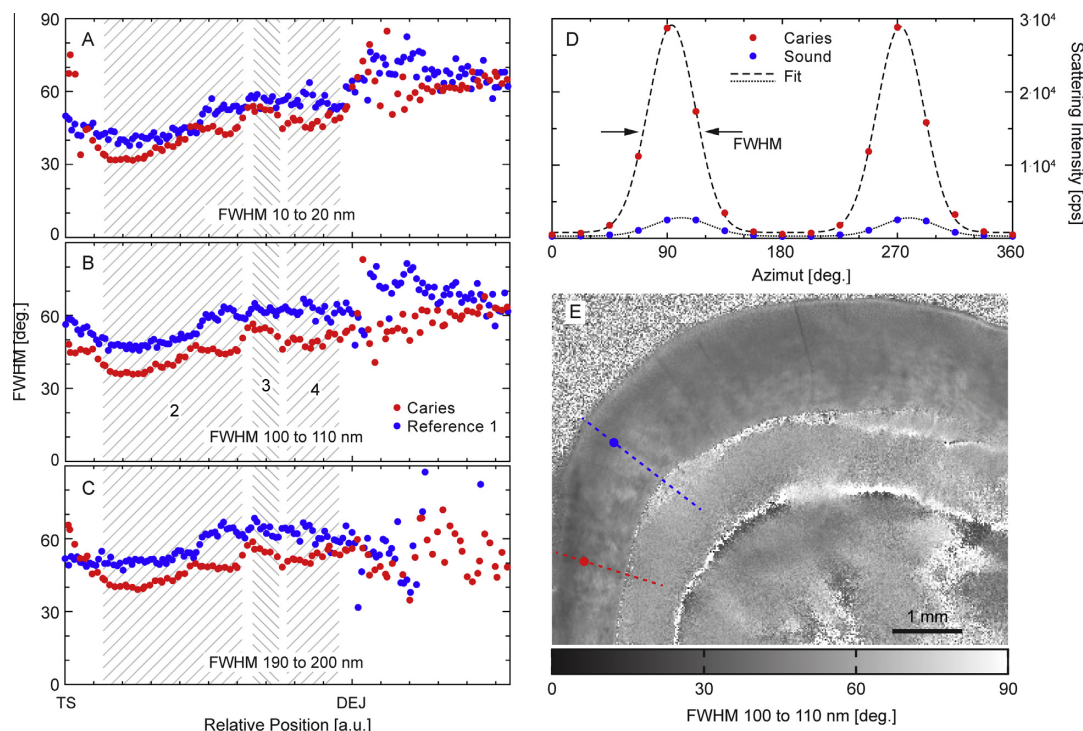


Fig. 5. (A–C) FWHM value of the azimuthal SAXS intensity distribution in the ranges 10–20 nm, 100–110 nm and 190–200 nm, respectively, along a line through the lesion (red dots) and one through unaffected enamel (blue dots, cf., (E)). The FWHM value determination is illustrated in (D). (D) SAXS intensity as function of the azimuthal angle around the central beam, for a point in the lesion (red-colored dots) and one in healthy enamel (blue-colored dots) of specimen H, according to (E). The intensity distribution was fitted with two Gaussians and a background. (E) The FWHM of the Gaussians was extracted for each raster scan point. Zone 1 of the lesion appears slightly darker than unaffected enamel, indicating increased anisotropy of the scattering signal.

microradiography and microhardness profiles [12], but have advanced knowledge in defining the underlying nanostructures.

Despite increased porosity and decreased density in the enamel and dentin immediately adjacent to the DEJ, the scattering intensity and absorption plots for carious and unaffected control samples intersected at this internal interface. The DEJ, a most remarkable structure, durably unites extremely dissimilar biomaterials, enamel and dentin, preventing crack propagation from brittle enamel into dentin, and preventing interfacial delamination [49–52]. This finding has extremely important implications for the restorative strategies used to address carious teeth, suggesting that ultraconservative approaches, beyond current minimally invasive approaches [53], could preserve an intact DEJ, even if bounded on both sides by partly de-mineralized tissues.

In the small early lesion, only a slight decrease in X-ray density in the outermost enamel was observed; whereas, the body of the lesion had a marked decrease. The scattering signal intensity presented a similar but inverse behavior, being comparable with that from healthy enamel at the surface of the tooth and increasing with decreasing X-ray density of the specimen. The $I_{\text{car}}/I_{\text{sound}}$ behavior is similar to that found in the fourth, deepest zone in the moderate lesion. The ratio $I_{\text{car}}/I_{\text{sound}}$ is higher for small scattering angles, i.e., periodicities >100 nm. This similarity indicates that both the subsurface body lesion and the deepest zone in the moderate lesion are cases of early caries attack, and a similar pore size distribution can be expected.

4.3. Nanostructure orientation and anisotropy

The mean orientation of the scattering signal remained unchanged among carious and sound tooth structure in both early

and moderate carious lesions. The mean orientation of the scattering signal in healthy enamel was clearly related to the arrangement of the crystallites in the rods running from the DEJ towards TS, with their *c*-axis parallel to the crystallite long axis [54], the scattering signal being aligned perpendicularly to this direction. Apparently, the contribution of the interrod crystallites (rod sheaths and tails) is less than the scattering from the highly ordered and closely packed crystallites within the rod body [55–60].

As illustrated in Fig. 5, caries-induced changes only slightly modify the SAXS signal anisotropy, towards higher anisotropy. The distinction was more marked in zone 2, where the highest degree of de-mineralization was found. Similarly, in the subsurface lesion in specimen V, where the de-mineralization reached 25%, a slight increase in anisotropy was observed. Here, the selective hollowing [61] and complete dissolution of individual crystallites within the rods leads to the increased equatorial scattering, parallel to the DEJ, while increase in scattering signal from the more resistant interrod crystallites is less prominent. In zone 3, where a certain degree of re-mineralization has taken place, the FWHM of the SAXS approximates that of unaffected enamel, i.e., anisotropy is decreased compared with zone 2, indicating that re-deposition processes give rise to at least partially isotropic structures. While the convergence between the FWHM values in carious and healthy tissues might indicate the restoration of tooth morphology through the naturally occurring re-mineralization, this does not necessarily mean that this is actually the case, since it is impossible to determine from the SAXS signal whether the re-deposition of material is happening preferentially at certain locations, such as within the rod or the interrod. The SAXS signal appears highly anisotropic, however, indicating that despite de- and re-minerali-

362

H. Deyhle et al./Acta Biomaterialia 10 (2014) 355–364

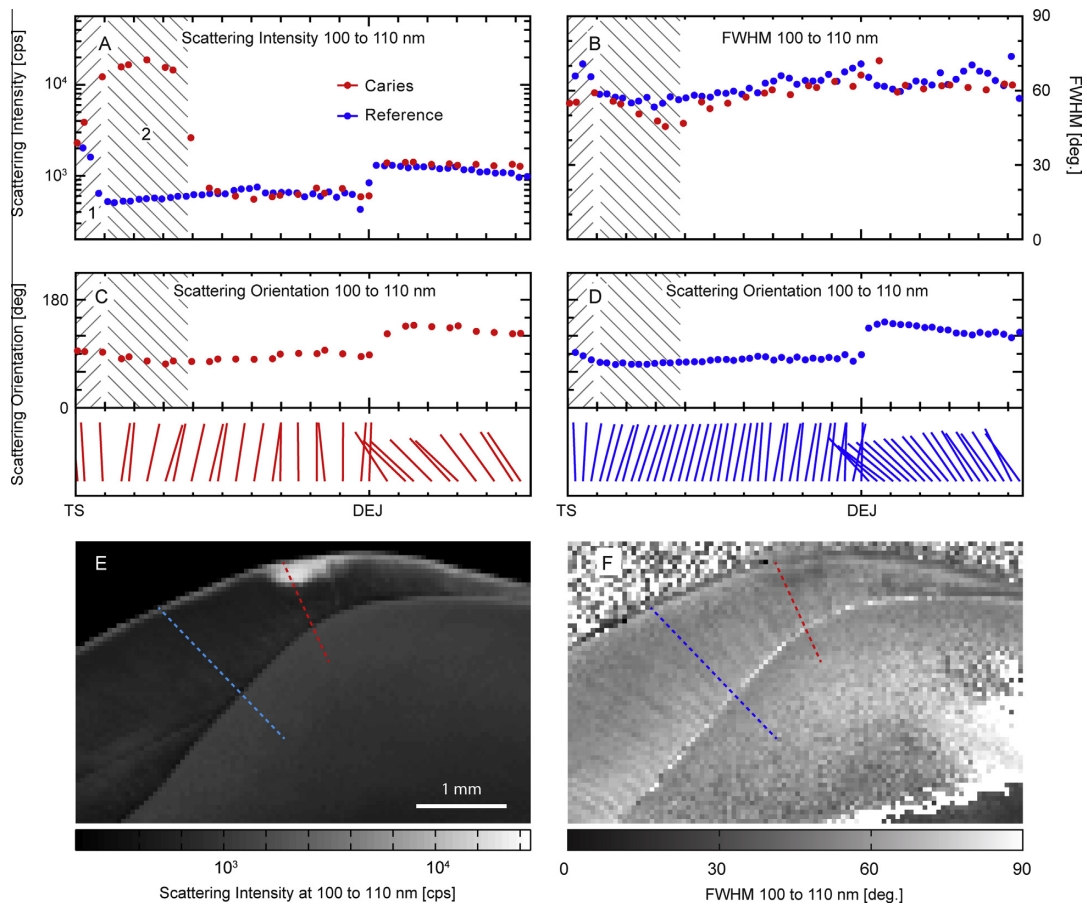


Fig. 6. Combined plots for specimen V. (A) Intensity of the scattering signal on a line through the lesion (red dots) and one through unaffected enamel (blue dots), in the range 100–110 nm, according to (E). The scattering signal in the outermost carious enamel, indicated by the shaded region labeled 1, approximates that of healthy enamel. The body of the carious lesion, located in the outer half of the enamel and indicated by the shaded region labeled 2, yields an increased scattering signal. (B) FWHM of the azimuthal intensity distribution of the scattering signal on a line through the lesion (red dots) and one through healthy enamel (blue dots), in the range 100–110 nm according to (F). The inner 50% of the lesion exhibits increased anisotropy, i.e., a reduced FWHM value. (C, D) Orientation of the scattering signal along a line through the lesion (C) and one through healthy enamel (D), in the range 100–110 nm according to (E), with respect to the dotted lines in (E). The carious lesion cannot be readily distinguished. (E) 2-D map of the total scattered intensity in the range 100–110 nm for specimen V. The carious lesion appears as a bright spot at the enamel surface. (F) 2-D map of the azimuthal intensity distribution in the range 100–110 nm. The lesion exhibits slightly increased anisotropy compared with unaffected enamel.

zation processes in zone 3 much of the enamel nanostructure is retained. Zone 4 presents FWHM values close to those from unaffected enamel. Since only little re-mineralization can be expected in zone 4, it appears that, despite caries-induced destruction, the structural anisotropy of the affected enamel is preserved. The retention of organization, despite de-mineralization, has important implications for the potential for interventions to not only re-mineralize de-mineralized enamel, but to do so in the original organizational form at the nanostructural level.

4.4. Confluence with classical caries models

Although the sample size was small, the lesions studied were carefully chosen to bracket the classically studied early carious lesion. The examination was performed in different perpendicular planes. The caries lesions were natural, probably occurring over years with innumerable cycles of de-mineralization and re-mineralization, rather than being artificially produced. They complemented prior SAXS data on fissure caries and an advanced

grossly cavitated lesion. Instead of a small amount of data on a large sample, this work produced an enormous amount of data (over 110,000 frames) on a small, but well-anchored, sample. It is important to note that the findings with respect to unaltered enamel were completely consistent with prior SAXS data on a variety of other teeth [33]; the data describing the studied lesions, early and moderate, in different planes, were entirely consistent with one-another and with classical models [9,10,12,14–16,20,21,31,35,41–43,45]. The findings were consistent with SAXS data previously reported for an advanced cavitated lesion and for fissure caries [33,36].

5. Conclusions

The fact that both orientation and anisotropy of the SAXS signal from carious enamel closely resembled those from unaffected regions reinforces the notion that naturally occurring de- and re-mineralization produce an anisotropic structure that retains the original nanoscale organization. This current SAXS data,

demonstrating the preservation of orientation in carious lesions, independent of degree of de-mineralization or pore morphology over 20–200 nm, advances understanding of the effects of de- and re-mineralization cycles at the crystallite level.

Acknowledgments

The support of F. Schmidli (Basel) during specimen preparation and acquisition of the light microscopy images is gratefully acknowledged. Beamtime at HASYLAB was granted under proposal number I-20080224 EC. The SAXS experiments were performed on the cSAXS beamline at the Swiss Light Source, Paul Scherrer, Institut, Villigen, Switzerland. Extracted teeth were kindly provided by dentists G. Krastl and N. Zitzmann (Basel).

Appendix A. Figures with essential color discrimination

Certain figures in this article, particularly Fig. 2, are difficult to interpret in black and white. The full color images can be found in the on-line version, at <http://dx.doi.org/10.1016/j.actbio.2013.08.024>

References

- [1] Bagramian RA, Garcia Godoy F, Volpe AR. The global increase in dental caries. A pending public health crisis. *Am J Dent* 2009;22:3–8.
- [2] Dye BA, Li X, Thornton-Evans G. Oral health disparities as determined by selected healthy people 2010 Oral Health Objectives for the United States, 2009–2010. *NCHS Data Brief* 2012;104:1–7.
- [3] Petersen PE. Challenges to improvement of oral health in the 21st century - the approach of the WHO Global Oral Health Programme. *Int Dent J* 2004;53:329–43.
- [4] Head JA. A study of saliva and its action on tooth enamel in reference to its hardening and softening. *J Amer Med Assoc* 1912;59:2118–22.
- [5] Lynch RJM, Smith SR. Remineralization agents - new and effective or just marketing hype? *Adv Dent Res* 2012;24:63–7.
- [6] Ten Cate JM, Arends J. Remineralization of artificial enamel lesions in vitro. *Caries Res* 1977;11:277–86.
- [7] Kidd EA, Fejerskov O. What constitutes dental caries? Histopathology of carious enamel and dentin related to the action of cariogenic biofilms. *J Dent Res* 2004;83(Spec No C):C35–8.
- [8] Applebaum E. Incipient dental caries. *J Dent Res* 1932;12:619–27.
- [9] Bergman G, Lind PO. A quantitative microradiographic study of incipient enamel caries. *J Dent Res* 1966;45:1477–84.
- [10] Buchalla W, Imfeld T, Attin T, Swain MV, Schmidlin PR. Relationship between nano-hardness and mineral content of artificial carious enamel lesions. *Caries Res* 2008;42:157–63.
- [11] Darling AL. The structure of the enamel revealed in dental disease. *Arch Oral Biol* 1961;4:80–5.
- [12] Featherstone JD, Behrman JM, Bell JE. Effect of whole saliva components on enamel demineralization in vitro. *Crit Rev Oral Biol Med* 1993;4:357–62.
- [13] Featherstone JD, ten Cate JM, Shariati M, Arends J. Comparison of artificial caries-like lesions by quantitative microradiography and microhardness profiles. *Caries Res* 1983;17:385–91.
- [14] Magalhães AC, Moron BM, Comar LP, Wiegand A, Buchalla W, Buzalaf MA. Comparison of cross-sectional hardness and transverse microradiography of artificial carious enamel lesions induced by different demineralising solutions and gels. *Caries Res* 2009;43:474–83.
- [15] Orams HJ, Phakey PP, Rachinger WA, Zybert JJ. Ultrastructural changes in the translucent and dark zones of early enamel caries. *J Oral Pathol* 1980;9:54–61.
- [16] Soni NN, Silberkweit M, Parrish BA. A microradiographic-microphotometric and polarized light study of the demineralization pattern in carious lesions. *Oral Surg Oral Med Oral* 1965;20:321–9.
- [17] Delbem ACB, Sasaki KT, Vieira AEM, Rodrigues E, Bergamaschi M, Stock SR, et al. Comparison of methods for evaluating mineral loss: hardness versus synchrotron microcomputed tomography. *Caries Res* 2009;43:359–65.
- [18] Dowker SEP, Elliott JC, Davis GR, Wilson RM, Cloetens P. Three-dimensional study of human dental fissure enamel by synchrotron X-ray microtomography. *Eur J Oral Sci* 2006;114:353–9.
- [19] Huang TTY, He L-H, Darendeliler MA, Swain MV. Correlation of mineral density and elastic modulus of natural enamel white spot lesions using X-ray microtomography and nanoindentation. *Acta Biomater* 2010;6:4553–9.
- [20] Gustafson G. The histopathology of caries of human dental enamel with special reference to the division of the carious lesion into zones. *Acta Odontol Scand* 1957;15:13–55.
- [21] Shellis RP, Hallsworth AS, Kirkham J, Robinson C. Organic material and the optical properties of the dark zone in caries lesions of enamel. *Eur J Oral Sci* 2002;110:392–5.
- [22] Theuns HM, Shellis RP, Groeneveld A, van Dijk JW, Poole DF. Relationships between birefringence and mineral content in artificial caries lesions of enamel. *Caries Res* 1993;27:9–14.
- [23] Kinney JH, Pople JA, Marshall GW, Marshall SJ. Collagen orientation and crystallite size in human dentin: a small angle X-ray scattering study. *Calcif Tissue Int* 2001;69:27–31.
- [24] Kinney JH, Nalla RK, Pople JA, Breunig TM, Ritchie RO. Age-related transparent root dentin: mineral concentration, crystallite size, and mechanical properties. *Biomaterials* 2005;26:3363–76.
- [25] Fratzl P, Paris O, Klaushofer K, Landis WJ. Bone mineralization in an osteogenesis imperfecta mouse model studied by small-angle X-ray scattering. *J Clin Invest* 1996;97:396–402.
- [26] Zizak I, Roschger P, Paris O, Misof BM, Berzlanovich A, Brenstorff S, et al. Characteristics of mineral particles in the human bone/cartilage interface. *J Struct Biol* 2003;141:208–17.
- [27] Kaabar W, Daar E, Bunk O, Farquharson MJ, Laklout A, Bailey M, et al. Elemental and structural studies at the bone-cartilage interface. *Nucl Instrum Methods Phys Res A* 2011;652:786–90.
- [28] Tanaka T, Yagi N, Ohta T, Matsuo Y, Terada H, Kamasaka K, et al. Evaluation of the distribution and orientation of remineralized enamel crystallites in subsurface lesions by X-ray diffraction. *Caries Res* 2010;44:253–9.
- [29] Tesch W, Eidelman P, Roschger P, Goldenberg F, Klaushofer K, Fratzl P. Graded microstructure and mechanical properties of human crown dentin. *Calcif Tissue Int* 2001;69:147–57.
- [30] Gutierrez P, Piña C, Lara VH, Bosch P. Characterization of enamel with variable caries risk. *Arch Oral Biol* 2005;50:843.
- [31] Märten A, Fratzl P, Paris O, Zaslansky P. On the mineral in collagen of human crown dentine. *Biomaterials* 2010;31:5479–90.
- [32] Jiang H, Liu X-Y, Lim CT, Hsu CY. Ordering of self-assembled nanobiominerals in correlation to mechanical properties of hard tissues. *Appl Phys Lett* 2005;86:163901.
- [33] Gaiser S, Deyhle H, Bunk O, White SN, Müller B. Understanding nano-anatomy of healthy and carious human teeth: a prerequisite for nanodentistry. *Biointerphases* 2012;7:4.
- [34] Fratzl P, Jakob HF, Rinnerthaler S, Roschger P, Klaushofer K. Position-resolved small-angle X-ray scattering of complex biological materials. *J Appl Crystallogr* 1997;30:765–9.
- [35] Yagi N, Ohta T, Matsuo T, Tanaka T, Terada Y, Kamasaka H, et al. Evaluation of enamel crystallites in subsurface lesion by microbeam X-ray diffraction. *J Synchrotron Radiat* 2009;16:398–404.
- [36] Deyhle H, Bunk O, Müller B. Nanostructure of healthy and caries-affected human teeth. *Nanomed Nanotechnol* 2011;7:694–701.
- [37] Beckmann F, Herzen J, Haibel A, Müller B, Schreyer A. High density resolution in synchrotron-radiation-based attenuation-contrast microtomography. *Proc SPIE* 2008;7078:70781D.
- [38] Müller B, Bernhardt R, Weitkamp T, Beckmann F, Bräuer R, Schurig U, et al. Morphology of bony tissues and implants uncovered by high-resolution tomographic imaging. *Int J Mater Res* 2007;98:613–21.
- [39] Bunk O, Bech M, Jensen TH, Feidenhansl R, Binderup T, Menzel A, et al. Multimodal x-ray scatter imaging. *New J Phys* 2009;11:123016.
- [40] Kraft P, Bergamaschi A, Broennimann C, Dinapoli R, Eikenberry EF, Henrich B, et al. Performance of single-photon-counting PILATUS detector modules. *J Synchrotron Radiat* 2009;16:368–75.
- [41] Darling AI. The selective attack of caries on the dental enamel. *Ann Roy Coll Surg* 1961;29:354–69.
- [42] Kielbassa AM, Wrbsas KT, Schulte M, Mönning J, Hellwig E. Correlation of transversal microradiography and microhardness on in situ-induced demineralization in irradiated and nonirradiated human dental enamel. *Arch Oral Biol* 1999;44:243–51.
- [43] Soni NN, Brudevold F. Microradiographic and polarized light studies of initial carious lesions. *J Dent Res* 1959;38:1187–94.
- [44] Arends J, Christoffersen J. The nature of early caries lesions in enamel. *J Dent Res* 1986;65:2–11.
- [45] Palamara J, Phakey PP, Rachinger WA, Orams HJ. Laminated zones in carious human dental enamel. *J Oral Pathol* 1986;15:109–14.
- [46] Wefel JS, Harless JD. The use of saturated DCPD in remineralization of artificial caries lesions in vitro. *J Dent Res* 1987;66:1640–3.
- [47] Robinson C, Shore RC, Bonass WA, Brookes SJ, Boteva E, Kirkham J. Identification of human serum albumin in human caries lesions of enamel: the role of putative inhibitors of remineralisation. *Caries Res* 1998;32:193–9.
- [48] Featherstone JD. The continuum of dental caries - evidence for a dynamic disease process. *J Dent Res* 2004;83(Spec Iss C):C39–42.
- [49] Imbeni V, Kruzic JJ, Marshall GW, Marshall SJ, Ritchie RO. The dentin-enamel junction and the fracture of human teeth. *Nat Mater* 2005;4:229–32.
- [50] White SN, Miklus VG, Chang PP, Caputo AA, Fong H, Sarikaya M, et al. Controlled failure mechanisms toughen the dentino-enamel junction zone. *J Prosthet Dent* 2005;94:330–5.
- [51] White SN, Paine ML, Luo W, Sarikaya M, Fong H, Yu Z, et al. The dentino-enamel junction is a broad transitional zone uniting dissimilar bioceramic composites. *J Am Ceram Soc* 2000;83:238–40.
- [52] Almer JD, Stock SR. High energy X-ray scattering quantification of in situ-loading-related strain gradients spanning the dentinoenamel junction (DEJ) in bovine tooth specimens. *J Biomech* 2010;43:2294–300.
- [53] Kidd EA. Clinical threshold for carious tissue removal. *Dent Clin N Am* 2010;54:541–9.

- [54] Al-Jawad M, Streuwer A, Kilconey SH, Shore RC, Cywinski R, Wood DJ. 2D mapping of texture and lattice parameters of dental enamel. *Biomaterials* 2007;28:2908–14.
- [55] Boyde A. A 3-D model of enamel development at the scale of one inch to the micron. *Adv Dent Res* 1987;1:135–40.
- [56] Helmcke J-G. Ultrastructure of enamel. In: Miles AEW, editor. *Structural and chemical organization of teeth vol II*. New York: Academic Press; 1967. p. 135–6.
- [57] Risnes S. Multiplane sectioning and scanning electron microscopy as a method for studying the three-dimensional structure of mature dental enamel. *Scanning Microsc* 1987;1:1893–902.
- [58] White SN, Luo W, Paine ML, Fong H, Sarikaya M, Snead ML. Biological organization of hydroxyapatite crystallites into a fibrous continuum toughens and controls anisotropy in human enamel. *J Dent Res* 2001;80:321–6.
- [59] Zahradnik RT, Moreno EC. Progressive stages of subsurface demineralization of human enamel. *Arch Oral Biol* 1977;22:585–91.
- [60] Eimar H, Chadimi E, Marelli B, Vali H, Nazhat SN, Amin WM, et al. Regulation of enamel hardness by its crystallographic dimensions. *Acta Biomater* 2012;8:3400–10.
- [61] Frazier PD. Adult human enamel: an electron microscopic study of crystallite size and morphology. *J Ultrastruct Res* 1968;22:1–11.

3 Conclusions

SR μ CT is a suitable tool for the high-resolution 3D imaging of human teeth, allowing for the rendering of the dentin tubules, which dominate the tooth microstructure. Both phase and absorption contrast imaging methods are viable alternatives. Intensity-based segmentation can be performed through thresholding. However, a second derivative filtering approach yields a more reliable tool when the voxel size of the dataset is below the mean tubule diameter. In this case, the filtering has the advantage of being less sensitive to noise. Variations in filter size might lead to an ulterior improvement of the segmentation.

Single-distance phase retrieval is preferred over multiple-distance phase retrieval or absorption data when imaging dentin tubular structure. Phase retrieval methods offer increased density resolution compared to absorption contrast measurements, while still retaining sufficient spatial resolution necessary for the visualization of individual tubules. Thus, these methods prove advantageous for imaging tooth tubular structure. Due to the pixel size necessary, below 1 μm , only specimens with diameters below 1 mm can be visualized simultaneously today. For an exhaustive characterization of the 3D organization of the tubuli, scans of multiple specimens obtained from the same tooth must be performed. Since beamtime at synchrotron radiation sources is limited, lengthy phase retrieval approaches, such as holotomography, which retrieves the phase from multiple scans at different specimen-detector distances, are disadvantageous compared to single-distance phase retrieval, where only one scan per specimen is necessary.

SAXS reveals strong anisotropies on the nanometer scale in both dentin and enamel. The scattering signal, which mainly originates from the inorganic nanometer-sized crystallites, shows preferential orientation depending on the location within the tooth. The architecture of the tooth follows the directions of maximal mechanical load. The orientations of the nanostructures within the dentin and the enamel are altered. Within certain regions, the nanostructures are almost perpendicular to each other at the dentin-enamel junction.

This knowledge should aid the development of bio-inspired dental fillings, which mimic the anisotropic structure of the tooth from the macroscopic scale, e.g. consisting of two distinct materials, in analogy to dentin and enamel, down to the nanometer-range, for example through the incorporation of functionalized carbon nanotubes. Such dental fillings should have superior resistance to thermal and mechanical loads.

Carious lesions, both in dentin and enamel, exhibit increased scattering potential compared to healthy tooth tissues. Since SAXS arises from electron density differences, the increased scattering signal is to be attributed to an increase in nanoscopic porosity, induced by the dissolution of the inorganic species. SAXS is extremely sensitive to caries, and allows to clearly identify mild lesion that are, for example only barely detected by X-ray absorption.

In moderate smooth enamel caries, which barely reaches dentin, SAXS allows for the identification of distinct zones presenting different scattering behavior. These zones are consistent with the classification of smooth surface lesions as defined by polarized light microscopy. Scattering intensity identifies three distinct zones in the moderate lesion's enamel: the body of the lesion characterized by strong scattering over the investigated ranges from 200 to 10 nm, indicative of high porosity and a wide pore size distribution; a second region presenting markedly less overall scattering, slightly lesser degree of orientation and slightly increased absorption; and a third deepest region, likely containing larger pores than the other regions with intermediate overall scattering, degree of orientation and absorption. A fourth zone, on the surface of the tooth exist and is speculated to possess scattering properties similar to those of unaffected healthy enamel. These zones are linked to the cyclic de- and re-mineralization occurring in the oral cavity.

Despite the caries induced deterioration, SAXS signal reveals the unaltered spatial organization of the nanometer-sized hydroxy-apatite crystallites within the carious lesion in enamel. This reinforces the notion that de-mineralization produces an anisotropic structure that retains the original nanoscale organization.

Despite increased porosity and decreased density in the enamel and dentin immediately adjacent to the DEJ in carious lesions extending from the enamel through the dentin, the DEJ within the lesion presents similar scattering behavior to the DEJ in healthy parts of the tooth. This indicates that the DEJ could preserve its original structure, and therefore also its remarkable mechanical properties, even if bounded on both sides by partly de-mineralized tissues.

At least during the initial stages of dentinal caries, when only mild de-mineralization is present, a significant part of the collagen network is conserved in abundance and orientation. It is noteworthy that differences in the degree of preservation of the collagen occur between specimens obtained from the same tooth. Thus, not only the total degree of de-calcification, but also the location within the carious lesion, seems to play a role concerning the damage to the collagen network. These findings were highlighted by the Editor of "Nanomedicine: Nanotechnology, Biology, and Medicine" as "groundbreaking study" and declared to be "clinically relevant" [40].

Bibliography

- [1] Helkimo, E., Carlson, G. E., and Helkimo, M., “Bite force and state of dentition,” *Acta Odontol. Scand.* **35**, 207–303 (1977).
- [2] Stack, M., “The chemical nature of the organic matrix of bone, dentin, and enamel,” *Annals of the New York Academy of Sciences* **60**, 585–595 (1955).
- [3] Meckel, A. H., Griebstein, W. J., and Neal, R. J., “Structure of mature human dental enamel as observed by electron microscopy,” *Archives of Oral Biology* **10**, 775–783 (1965).
- [4] Frazier, P. D., “Adult human enamel: An electron microscopic study of crystallite size and morphology,” *Journal of Ultrastructure Research* **22**, 1–11 (1968).
- [5] Simmelink, J. W., Nygaard, V. K., and Scott, D. B., “Theory for the sequence of human and rat enamel dissolution by acid and by edta: A correlated scanning and transmission electron microscope study,” *Archives of Oral Biology* **19**, 183–197 (1974).
- [6] Habelitz, S., Marshall, S. J., Marshall, Jr., G. W., and Balooch, M., “Mechanical properties of human dental enamel on the nanometre scale,” *Archives of Oral Biology* **46**, 173–183 (2001).
- [7] White, S. N., Luo, W., Paine, M. L., Fong, H., Sarikaya, M., and Snead, M. L., “Biological organization of hydroxyapatite crystallites into a fibrous continuum toughens and controls anisotropy in human enamel,” *Journal of Dental Research* **80**, 321–326 (2001).
- [8] Marshall, G. W., Marshall, S. J., Kinney, J., and Balooch, M., “The dentin substrate: Structure and properties related to bonding,” *Journal of Dentistry* **25**, 441–458 (1997).
- [9] Fratzl, P., Jakob, H., Rinnerthaler, S., Roschger, P., and Klaushofer, K., “Position-resolved small-angle x-ray scattering of complex biological materials,” *Journal of Applied Crystallography* **30**, 765–769 (1997).
- [10] Bunk, O., Bech, M., Jensen, T., Feidenhans'l, R., Binderup, T., Menzel, A., and Pfeiffer, F., “Multimodal x-ray scatter imaging,” *New Journal of Physics* **11**, 123016 (2009).
- [11] Kratky, O., [*Small angle X-ray scattering*], Academic Press (1982).
- [12] Guinier, A. and Fournet, G., [*Small angle scattering of X-rays*], John Wiley & Sons, Inc., New York (1955).
- [13] Urwyler, P., Deyhle, H., Bunk, O., Kristiansen, P. M., and Müller, B., “Nanometer-size anisotropy of injection-molded polymer micro-cantilever arrays,” *Journal of Applied Physics* **111**, 103530 (2012).

- [14] Althaus, J., Deyhle, H., Bunk, O., Kristiansen, P. M., and Müller, B., “Anisotropy in polyetheretherketone films,” *Journal of Nanophotonics* **6**, 063510 (2012).
- [15] Müller, B., Deyhle, H., Bradley, D., Farquharson, M., Schulz, G., Müller-Gerbl, M., and Bunk, O., “Scanning x-ray scattering: Evaluating the nanostructure of human tissues,” *European Journal for Clinical Nanomedicine* **3**, 30–33 (2010).
- [16] Nalla, R. K., Kinney, J., and Ritchie, R., “Effect of orientation on the in vitro fracture toughness of dentin: The role of toughening mechanisms,” *Biomaterials* **24**, 3955–3968 (2003).
- [17] Inoue, S., Pereira, P. N. R., Kawamoto, C., Nakajima, M., Koshiro, K., Tagami, J., Carvalho, R. M., Pashley, D. H., and Sano, H., “Effect of depth and tubule direction on ultimate tensile strength of human coronal dentin,” *Dent. Mater. J.* **22**, 39–47 (2003).
- [18] Kinney, J., Marshall, S., and Marshall, G., “The mechanical properties of human dentin: a critical review and re-evaluation of the dental literature,” *Critical Reviews in Oral Biology & Medicine* **14**, 13–29 (January 1, 2003 2003).
- [19] Köhl, S., Deyhle, H., Zimmerli, M., Spagnoli, G., Beckmann, F., Müller, B., and Filippi, A., “Cracks in dentin and enamel after cryo-preservation,” *Oral Surgery, Oral Medicine, Oral Pathology, Oral Radiology and Endodontology* **113**, e5–e10 (2011).
- [20] Kofmehl, L., Schulz, G., Deyhle, H., Filippi, A., Hotz, G., Berndt-Dagassan, D., Kramis, S., Beckmann, F., and Müller, B., “Computed tomography to quantify the loss of enamel and dentin resulting from clay pipe smoking,” *Proceedings of SPIE* **7804**, 78041F (2010).
- [21] Deyhle, H., Bunk, O., Buser, S., Krastl, G., Zitzmann, N., Ilgenstein, B., Beckmann, F., Pfeiffer, F., Weiger, R., and Müller, B., “Bio-inspired dental fillings,” *Proceedings of SPIE* **7401**, 74010E (2009).
- [22] Deyhle, H., Weitkamp, T., Lang, S., Schulz, G., Rack, A., Zanette, I., and Müller, B., “Comparison of propagation-based phase-contrast tomography approaches for the evaluation of dentin microstructure,” *Proceedings of SPIE* **8506**, 85060N (2012).
- [23] Stock, S. R., Vieira, A. E. M., Delbem, A. C. B., Cannon, M. L., Xiao, X., and De Carlo, F., “Synchrotron microcomputed tomography of the mature bovine dentinoenamel junction,” *J. Struct. Biol.* **161**, 162–171 (2008).
- [24] Parkinson, C. R. and Sasov, A., “High-resolution non-destructive 3D interrogation of dentin using X-ray nanotomography,” *Dent. Mater.* **24**, 773–777 (2008).
- [25] Zabler, S., Cloetens, P., and Zaslansky, P., “Fresnel-propagated submicrometer X-ray imaging of water-immersed tooth dentin,” *Opt. Lett.* **32**, 2987–2989 (2007).
- [26] Zaslansky, P., Zabler, S., and Fratzl, P., “3d variations in human crown dentin tubule orientation: A phase-contrast microtomography study,” *Dental Materials* **26**, e1–e10 (2010).

- [27] Sunnegardh-Grönberg, K., VanDijken, J. W. V., and Funegard, U., “Selection of dental materials and longevity of replaced restorations in public dental health clinics in northern sweden,” *Journal of Dentistry* **37**, 673–678 (2009).
- [28] VanNieuwenhuysen, J.-P., D’Hoore, W., Carvalho, J., and Qvist, V., “Long-term evaluation of extensive restorations in permanent teeth,” *Journal of Dentistry* **31**, 395–405 (2003).
- [29] Kernen, F., Waltimo, T., Deyhle, H., Beckmann, F., Stark, W., and Müller, B., “Synchrotron radiation-based micro computed tomography in the assessment of dentin de- and re-mineralization,” *Proceedings of SPIE* **7078**, 7078M (2008).
- [30] Bertassoni, L. E., Habelitz, S., Pugach, M., Soares, P., Marshall, S., and Marshall, G., “Evaluation of surface structural and mechanical changes following remineralization of dentin,” *Scanning* **32**, 312–319 (2010).
- [31] Zahradnik, R. T. and Moreno, E. C., “Progressive stages of subsurface demineralization of human tooth enamel,” *Archives of Oral Biology* **22**, 585–591 (1977).
- [32] Moreno, E. C. and Zahradnik, R. T., “The pore structure of human dental enamel,” *Archives of Oral Biology* **18**, 1063–1068 (1973).
- [33] Gaiser, S., Deyhle, H., Bunk, O., White, S. N., and Müller, B., “Understanding nano-anatomy of healthy and carious human teeth: a prerequisite for nanodentistry,” *Biointerphases* **7**, 4 (2012).
- [34] Ohgushi, K. and Fusayama, T., “Electron microscopic structure of the two layers of carious dentin,” *Journal of Dental Research* **54**, 1019–1026 (1975).
- [35] Pugach, M., Strother, J., Darling, C., Fried, D., Gansky, S., Marshall, S., and Marshall, G., “Dentin caries zones: mineral, structure, and properties,” *Journal of Dental Research* **88**, 71–76 (2009).
- [36] Deyhle, H., Hieber, S., and Müller, B., [*Encyclopedia of Nanotechnology*], ch. Nanodentistry, 1514–1518, Springer (2012).
- [37] Weitkamp, T., Haas, D., Wegrzynek, D., and Rack, A., “ANKAphase: software for single-distance phase retrieval from inline X-ray phase-contrast radiographs,” *J. Synchrotron Rad.* **18**, 617–629 (2011).
- [38] Paganin, D., Mayo, S. C., Gureyev, T. E., Miller, P. R., and Wilkins, S. W., “Simultaneous phase and amplitude extraction from a single defocused image of a homogeneous object,” *J. Microsc.* **206**, 33–40 (2002).
- [39] Herzen, J., Donath, T., Pfeiffer, F., Bunk, O., Padeste, C., Beckmann, F., Schreyer, A., and David, C., “Quantitative phase-contrast tomography of a liquid phantom using a conventional X-ray tube source,” *Opt. Express* **17**, 10010–10018 (2009).
- [40] Deyhle, H., Bunk, O., and Müller, B., “Nanostructure of healthy and caries-affected human teeth,” *Nanomedicine: Nanotechnology, Biology, and Medicine* **7**, 694–701 (2011).

Acknowledgments

My thanks go to Prof. Dr. Bert Müller for giving me the opportunity to perform this PhD thesis. Under his supervision I was introduced to a vast variety of fields and had the opportunity to work in a truly interdisciplinary environment. Without his support and advice this work would not have been possible. My thanks also go to Prof. Dr. Thomas Jung, who acted as co-referee for this work.

Dr. Oliver Bunk has introduced me to the world of small-angle X-ray scattering. Thank you for the (often lengthy) discussions, for all the support with the measurements and the analysis routines, for the night-shifts at the beamline, and for the coffee and tea.

I thank Dr. Andreas Menzel, Dr. Ana Diaz and Xavier Donath for all the support during SAXS measurements, for the hints, the tips and the tricks they shared with me.

Special thanks go to Prof. Dr. Shane White for welcoming me at UCLA. His enthusiasm in discussing and analyzing data gave me an additional motivation boost.

I want to thank Dr. Felix Beckmann for all the help during the measurements at HASYLAB. Also, the trips to the Mühle were always appreciated.

Dr. Timm Weitkamp supported me during the beamtimes at the ID19 beamline at ESRF. I want to thank him for his help and for his patience in answering all my questions.

Specimen preparation for my experiments wouldn't have been possible without Fredy Schmidli. Thank you for your help and sorry for all the broken diamond bands.

Dr. Marlen Luckow, Prof. Dr. Nicola Zitzmann and Dr. Gabriel Krastl have my gratitude for providing the tooth specimen.

I want to thank the whole Biomaterials Science Center for the great collaboration and all the interesting tasks associated with it. Special thanks go to Dr. Georg Schulz for all the fruitful discussions, and for generally being a source of distraction.

OpenSuse, KDE and ksirk.

My thanks go to “MaMa-eat” for providing food to the hungry and to “Drinks of the world” for providing drinks to the thirsty.

Rockeyes, Thunderdeath, Disgraceful and Sluthorn for the many hours of distraction and the occasional tinnitus.

Ruth for the countless dinners. Thank you for feeding me abundantly.

Nic, Goran and Liv for just being there.

Last but not least, my thanks go to my parents. They have always had an open ear for my complaints, always good advice, and they have always supported me in everything I have done, far beyond this thesis. Thank you!

Curriculum Vitae

Family Name: Deyhle
First Name: Hans
Citizenship: Swiss
Date of Birth: 24.11.1982
Place of Birth: Zürich, Switzerland

Education

2009-2012 PhD student in experimental physics,
Biomaterials Science Center
University of Basel, Switzerland
2008 Diploma in experimental physics at the
Swiss Federal Institute of Technology
Zürich, Switzerland
2001 Federal university-entrance diploma type C
Locarno, Switzerland

Professional Experience

2012-2013 Post-Doc
Biomaterials Science Center
University of Basel, Switzerland
2009-2012 PhD student in experimental physics,
Biomaterials Science Center
University of Basel, Switzerland
2008-2009 Scientific collaborator at School for Dental Medicine
Institute of Material Science
University of Basel, Switzerland
2007-2008 Research assistant at the Biomaterials Science Center
University of Basel, Switzerland
2007 Junior Research Assistant at the
Department of Mathematics
Swiss Federal Institute of Technology
Zürich, Switzerland

Erklärung

Hiermit versichere ich, dass ich die vorliegende Arbeit selbständig verfasst und keine anderen als die angegebenen Quellen und Hilfsmittel benutzt habe.

Basel, den 30.10.2012

Hans Deyhle